Title
Identifying the Magnetospheric Source of Pi2 Pulsations Using Global MHD Simulations

Author
Ream, Jodie Barker

Publication Date
2015

Peer reviewed|Thesis/dissertation

University of California
Los Angeles

Identifying the Magnetospheric Source of Pi2 Pulsations Using Global MHD Simulations

A dissertation submitted in partial satisfaction
of the requirements for the degree
Doctor of Philosophy in Geophysics and Space Physics

by

Jodie Barker Ream

2015

Abstract of the Dissertation

Identifying the Magnetospheric Source of Pi2 Pulsations Using Global MHD Simulations

by

Jodie Barker Ream

Doctor of Philosophy in Geophysics and Space Physics

University of California, Los Angeles, 2015

Professor Raymond J. Walker, Co-chair

Professor Maha Ashour-Abdalla, Co-chair

Pi2 pulsations are magnetic field fluctuations with periods between 40 an 150 seconds observed on the ground in conjunction with the onset of magnetospheric substorms. Pi2 period perturbations are also observed in magnetic field and plasma observations in space in conjunction with fast earthward flows leading to several theories concerning how and where the pulsations are generated. We investigate the source and propagation of Pi2 period pulsations through the magnetosphere, tracing the disturbances from their origin in the magnetotail through the inner edge of the plasma sheet and into the inner magnetosphere. Several models for the generation of Pi2 pulsations have been constructed by using satellite and ground-based observations. Our approach is to use global magnetohydrodynamic (MHD) computer codes to simulate the Earth's magnetosphere during substorms to determine where the Pi2 period perturbations are being generated. We use two different MHD models, the UCLA and Lyon-Fedder-Mobarry (LFM) models, in order to test the robustness of our conclusions about Pi2. The simulation results are compared with ground-based and satellite data for validation.

We find that Pi2 period perturbations are generated in both models by earthward propagating fast flows inside of x$\sim$-12 R_E. As the flows propagate through the braking region, the region where flows slow down as they approach the inner edge of the plasma sheet, the

pulsations begin to run ahead of the fast flow and its accompanying dipolarization front into the inner magnetosphere. This indicates that a compressional wave is being generated by the flow as it slows in the braking region. The speed of the flows, and the penetration of the flows and perturbations into the inner magnetosphere, depends strongly on the ionospheric models used at the inner boundary of the MHD models. When modeled Pedersen conductances are high with respect to typically observed values, strong line-tying slows the flows more quickly in the braking region. Therefore, perturbations are not able to propagate as freely into the inner magnetosphere.

When looking at the power spectral density (PSD) we find that the fluctuations in B_z propagate with the flow channel until they reach $\sim$-8 R_E, but as the disturbance approaches the inner edge of the plasma sheet the flow speeds decrease and the perturbations propagate earthward and spread azimuthally. As a result the perturbations generated by an azimuthally thin flow channel would be observed over a large area on the ground. Field line tracing shows that ionospheric perturbations do not always map to a flow channel, but they do map to a disturbance in the thermal pressure associated with the flow. Since the flows are responsible for the thermal pressure perturbations, they are also indirectly responsible for the perturbations observed in the simulated ionosphere.

The dissertation of Jodie Barker Ream is approved.

Margaret G. Kivelson

Maha Ashour-Abdalla, Committee Co-chair

Raymond J. Walker, Committee Co-chair

University of California, Los Angeles

2015

To my husband Robert, and my wonderful daughters Kalila and Autumn.

Table of Contents

List of Figures

Acknowledgments

First, I would like to give a sincere thank you to my advisors, Raymond Walker and Maha Ashour-Abdalla, for all of their guidence and support. I would also like to thank Margaret G. Kivelson, Krishan Khurana, James Weygand, and Robert J. Strangeway for many helpful group meeting discussions and debates during the course of this research.

This work was supported by NASA grant NNX09AV91G. This research was also supported in part by the NASA Graduate Student Research Program through Goddard Space Flight Center, grant number NNX10AM08H. I would like to acknowledge high-performance computing support from Yellowstone (ark:/85065/d7wd3xhc) provided by NCAR's Computational and Information Systems Laboratory, sponsored by the National Science Foundation. Computational resources for the UCLA model were provided by the Extreme Science and Engineering Discovery Environment (XSEDE), which is supported by National Science Foundation grant number OCI-1053575. All satellite and OMNI data were obtained through the Virtual Magnetospheric Observatory (VMO, http://vmo.igpp.ucla.edu/). We acknowledge the experiment teams that acquired, processed and provided the OMNI-included data, and J.H. King and N.E. Papitashvili of NASA/GSFC for creating the OMNI data set. Geotail magnetic field data were provided by T. Nagai, JAXA in Japan. We acknowledge Prof. C. Carr and the Double Star TC1 FGM instrument team, as well as ESA, Double Star, Center for Space Science and Applied Research, and the Chinese Academy of Sciences for Double Star data. I acknowledge NASA, Andre Balogh, and Elizabeth E. Lucek for use of data from the CLUSTER mission. I acknowledge NASA contract NAS5-02099 and V. Angelopoulos for use of data from the THEMIS Mission, K. H. Glassmeier, U. Auster and W. Baumjohann for the use of FGM data provided under the lead of the Technical University of Braunschweig and with financial support through the German Ministry for Economy and Technology and the German Center for Aviation and Space (DLR) under contract 50 OC 0302, as well as S. Mende and E. Donovan for use of the ASI data, and the CSA for logistical support in fielding and data retrieval from the GBO stations. I also acknowledge the World Data Center for Geomagnetism, Kyoto (http://wdc.kugi.kyoto-u.ac.jp/index.html), and the

Geomagnetic Network of China, for Pi2 data. Copyright permissions have been obtained for the reproduction of figures from Nature Publishing Group (Figure 1.2), and Wiley Publishing (Figures 1.4, 1.5, and 1.6).

Chapter 2 is a version of *Ream et al.* (2013).

Chapter 3 is a version of *Ream et al.* (2015)

Vita

2005	A.S. in English Salt Lake Community College.
2005-2009	Data Analyst Center for Atmospheric and Space Science, Utah State University.
2005-2007	President of the Society of Physics Students Chapter Utah State University.
2007-2008	Eccles Undergraduate Research Fellowship Department of Physics, Utah State University.
2008-2009	Undergraduate Research Award and Leadership Scholarship Society of Physics Students.
2008-2009	Barry Goldwater Scholarship Utah State University.
2009	B.A. in Physics with Minors in Mathematics and Classics Department of Physics, Utah State University.
2009-2015	Graduate Student Researcher Dept. of Earth, Planetary and Space Sciences, UCLA.
2010-2013	Graduate Student Research Program (GSRP) Fellowship Goddard Space Flight Center, NASA
2012	Outstanding Student Paper Award Space Physics and Aeronomy Section, American Geophysical Union.
2012	M.S. Geophysics and Space Physics Dept. of Earth, Planetary and Space Sciences, UCLA.
2014	Harold and Mayla Sullwold Scholarship Dept. of Earth, Planetary and Space Sciences, UCLA.

Publications

Nielsen, K, G. E. Nedoluha, A. C., L. C. Chang, **J. Barker-Tvedtnes**, M. J. Taylor, N. J. Mitchell, A. Lambert, M. J. Schwartz, J. M. Russell III (2011), On the origin of mid-latitude mesospheric clouds: The July 2009 cloud outbreak, *J. of Atmos. Solar-Terr. Phys.*, *73*, Issues 14-15, 2118-2124, doi:10.1016/j.jastp.2010.10.015.

Ream, J. B., R. J. Walker, M. Ashour-Abdalla, M. El-Alaoui, M. G. Kivelson, and M. L. Goldstein (2013), Generation of Pi2 pulsations by intermittent earthward propagating dipolarization fronts: An MHD case study, *J. Geophys. Res.*, *118*, 6364–6377, doi: 10.1002/2013JA018734.

Ream, J. B., R. J. Walker, M. Ashour-Abdalla, M. El-Alaoui, M. Wiltberger, M. G. Kivelson, and M. L. Goldstein (2013), Propagation of Pi2 Pulsations Through the Braking Region in Global MHD Simulations (*Submitted*), *J. Geophys. Res.*, doi:10.1002/2015JA021572.

Taylor, M. J., Y. Zhao, P. D. Pautet, M. J. Nicolls, R. L. Collins, **J. Barker-Tvedtnes**, C. D. Burton, B. Thurairajah, J. Reimuller, R. H. Varney, C. J. Heinselman, K. Mizutani (2009), Coordinated optical and radar image measurements of noctilucent clouds and polar mesospheric summer echoes, *J. Atmos. Solar-Terr. Phys.*, *71*, Issues 6-7, 675-687, doi: 10.1016/j.jastp.2008.12.005.

Weygand, J. M., M. G. Kivelson, H. U. Frey, J. V. Rodriguez, V. Angelopoulos, R. Redmon, **J. Barker-Ream**, A. Grocott, and O. Amm (2015),An interpretation of spacecraft and ground based observations of multiple omega band events, *J. Atmos. Solar-Terr. Phys.*, *133*, 185-204, doi:10.1016/j.jastp.2015.08.014.

CHAPTER 1

Introduction

Ultra-low frequency (ULF) pulsations in the Earth's magnetic field have been observed from the ground since the mid 1700s. However, very little was known about the origin of the pulsations until some very important discoveries were made concerning the near-Earth region of space. 1) There is a constant stream of particles being released from the Sun, known as the solar wind, that interacts with the Earth's magnetosphere. 2) The development of a low frequency description of a magnetized plasma, referred to as magnetohydrodynamics (MHD), by *Alfvén* (1942), including the discovery of a wave mode that is able to travel along magnetic field lines. 3) The initial description of magnetic reconnection by Sweet and Parker in 1956 (*Parker*, 1957), and the proposal by *Dungey* (1961) that reconnection drives convection in the magnetosphere.

After several different types of fluctuations had been identified in ground-based magnetometer records, *Jacobs et al.* (1964) put forward a way to categorize the different signatures based on their waveform and their period (T). The categories for the observed pulsations are Pc (continuous pulsations) and Pi (irregular pulsations). Table 1.1 outlines the period and frequency ranges for each of the ULF pulsation categories. Each group of pulsations is thought to be generated by a different set of phenomena that take place in the Earth's magnetosphere.

Category	Pc1	Pc2	Pc3	Pc4	Pc5	Pi1	Pi2
Period (sec)	0.2-5	5-10	10-45	45-150	150-600	1-40	40-150
Frequency (mHz)	5000-200	200-100	100-22	22-6.7	6.7-1.67	1000-25	25-6.7

Table 1.1: Categories of ULF pulsations adopted from *Jacobs et al.* (1964)

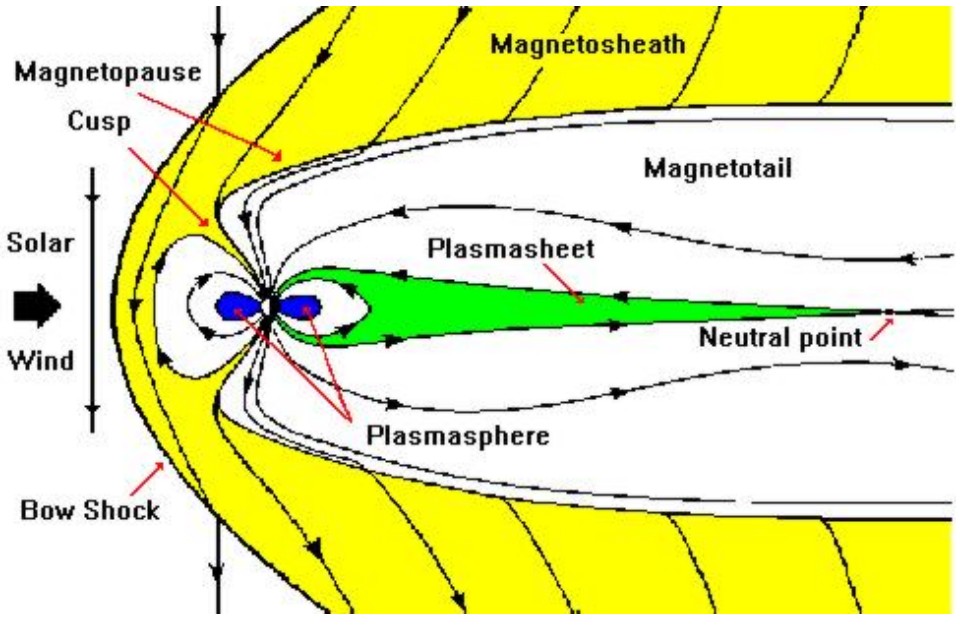

Figure 1.1: Meridional cut of the Earth's magnetosphere. (Image courtesy NASA)

1.1 The Magnetosphere

The Earth's magnetosphere can be divided into different regions shown in Figure 1.1. On the dayside the magnetosphere is compressed by the solar wind. The solar wind dynamic pressure is balanced by the magnetic pressure in the Earth's magnetic field at the magnetopause (*Schield*, 1969). The bow shock acts to slow the supersonic solar wind to sub-sonic speeds as it moves around the obstacle created by Earth's magnetic field. The night side of the magnetosphere is dragged out into a long tail with north and south lobes composed of cold dense plasma. The two lobes are separated by the plasma sheet, a region of hot tenuous plasma with a strong east-west current across the tail. The inner magnetosphere, earthward of the inner edge of the plasma sheet, is dominated by the dipole field. Different populations in the inner magnetosphere include the cold dense plasmasphere population, and the energetic radiation belt population.

However, during intervals when Earth's magnetic field is interacting directly with the solar wind the picture is not as well defined as that shown in Figure 1.1. Any process that disturbs the quiescent magnetic field configuration can generate fluctuations that may be observed as ULF pulsations on the ground. Interactions between the solar wind and

the magnetosphere generate pulsations directly by imposing a periodicity in the solar wind directly on the magnetosphere as the solar wind moves around the planet, or through the coupling of the solar wind and terrestrial magnetic fields. This occurs most readily during intervals when the solar wind is oriented in the southward direction with respect to the Earth's magnetic pole, the solar wind magnetic field and the Earth's magnetic field can interact through a process known as magnetic reconnection. When two oppositely oriented magnetic fields are pushed close enough together the field lines break and change partners as depicted in Figure 1.2. The inflow regions bring plasma from the lobes into the reconnection region. The field lines are brought into the ion diffusion region the ions become demagnetized so they are no longer frozen to the magnetic field. Because the ions and electrons are no longer moving together a Hall current is generated. The particles are pushed by the current into the outflow region where they are once again frozen to the magnetic field.

At times when magnetic reconnection is taking place at the magnetopause the magnetic flux is stripped away from the dayside and transported with the solar wind to the night side where it builds up until the magnetic pressure becomes so strong in the magnetotail that the plasma sheet becomes pinched and reconnection commences on the nightside. The magnetic field on the sunward side of the reconnection point in the plasma sheet is then transported earthward and eventually returned to the dayside as depicted in Figure 1.3. This process of transferring magnetic flux from the dayside, across the polar cap to the nightside, and back to the dayside via reconnection in the magnetopause and plasma sheet is known as the Dungey cycle.

During intervals when the interplanetary magnetic field (IMF) is southward, and reconnection is occurring on the dayside, the magnetotail can become very active as reconnection commences on the nightside to balance the system and return magnetic flux to the dayside. During these intervals, energy is transported from reconnection in the tail earthward and much of the energy is deposited in the ionosphere. *Palmroth et al.* (2006) calculated the precipitation and total power consumption during two substorms in March 1998 using both an MHD simulation and observations and found that different methods for precipitation power give very different results. The precipitation in northern hemisphere found using Polar UVI

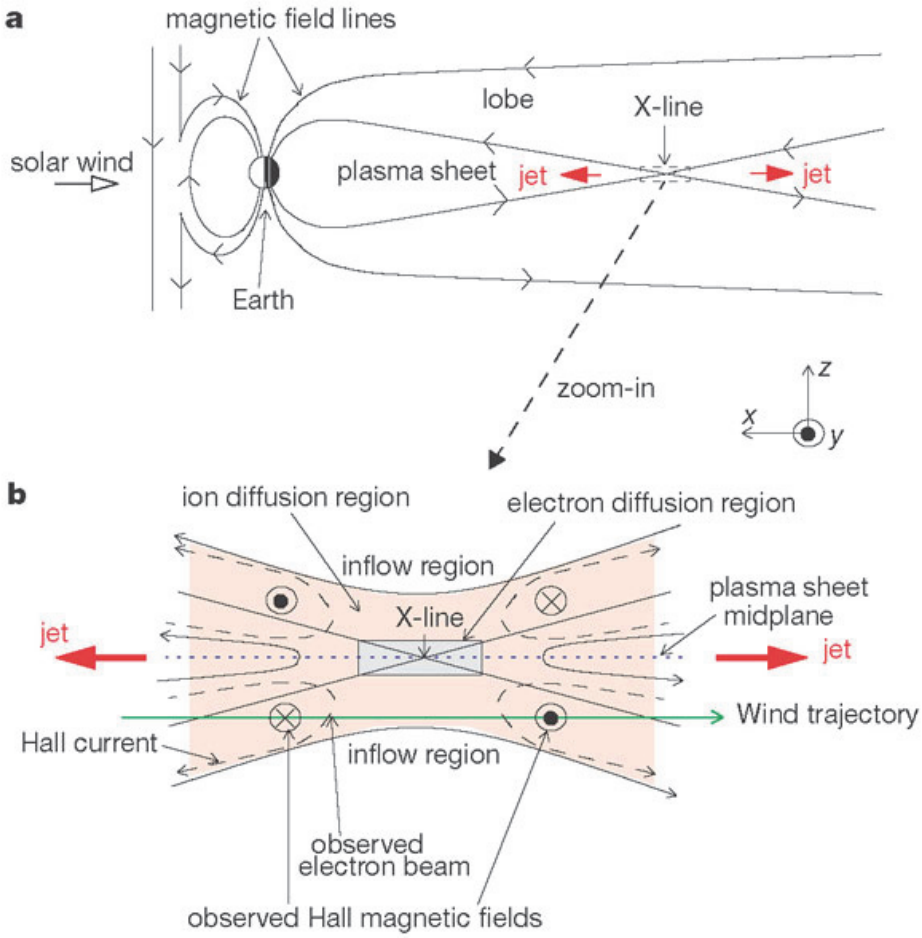

Figure 1.2: a) A meridional cut of the magnetosphere at midnight showing the location of the reconnection region. b) Schematic for magnetic reconnection in the plasma sheet. Solid lines with arrows indicate magnetic field configuration, and red arrows show flow direction in the outflow region. The electron diffusion region is shown by the gray rectangle at the center of the diagram. The ion diffusion region is indicated by the light pink color. The dashed black lines indicate the location and direction of the Hall current and the circles indicate the direction of the Hall magnetic field. (*Øieroset et al.*, 2001).

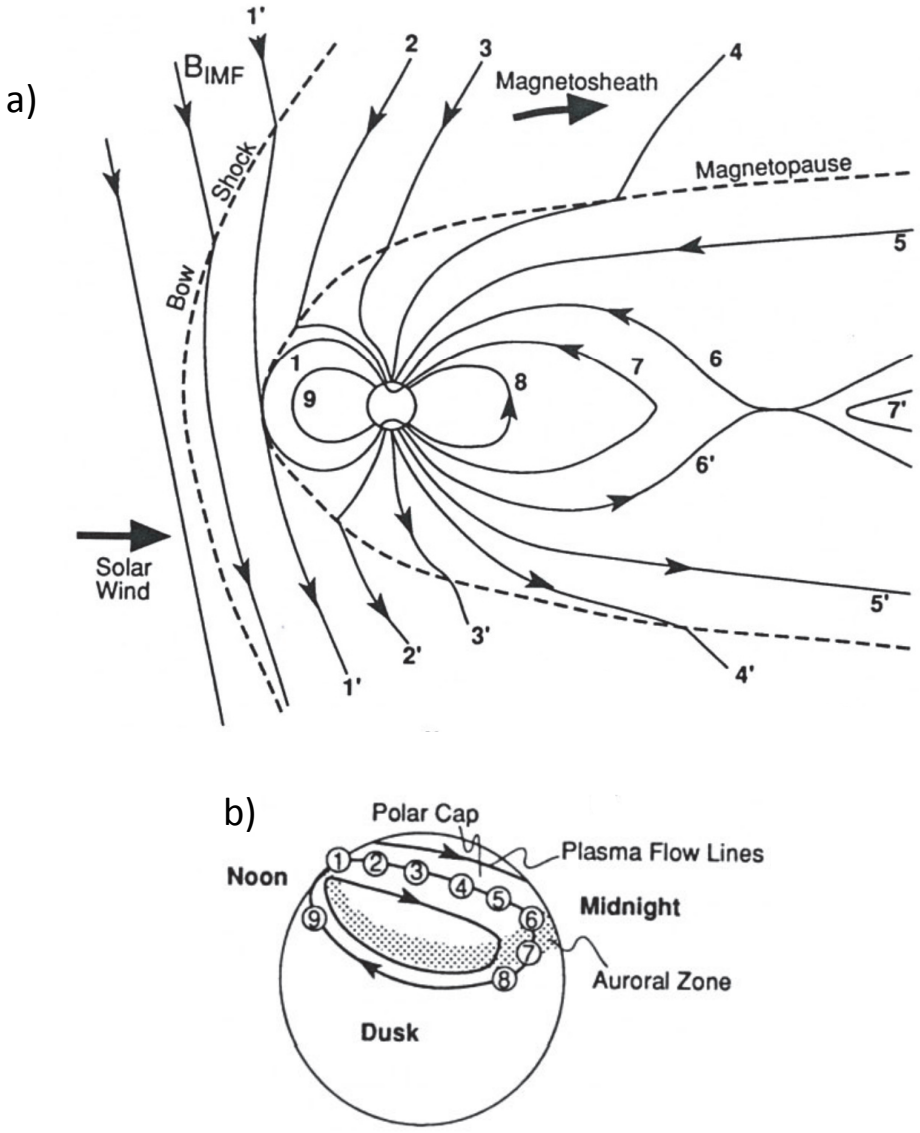

Figure 1.3: a) Magnetospheric convection driven by reconnection. Numbered lines represent the motion of a field line from reconnection at the dayside magnetopause at 1(1') to reconnection in the plasmasheet at 6(6') and back to the dayside a 9. b) positions of the footprint of the numbered field lines in panel a) shown with plasma flow lines in the ionosphere as a result of the reconnection-driven convection in the magnetosphere (Figure 9.11 *Kivelson and Russell* (1995)).

varied between ∼40 GW and ∼90 GW.

Because any process in the magnetosphere that perturbs the magnetic field from its equilibrium state can be a source for waves observed on the ground, these active intervals are prime candidates for ULF wave generation. There has been a great deal of work done on identifying the source of ULF waves in the magnetosphere, but magnetospheric measurements are very sparse so identifying how and where waves are generated during transient events, such as those related to impulsive reconnection, is difficult. One class of transient events, referred to as substorms, is of particular interest because they are a major mechanism for energy transport from the solar wind to the ionosphere.

1.2 Substorms

There are several different names used to describe different levels of activity such as steady magnetospheric convection (SMC), substorms, and pseudo-breakups. The activity level in the magnetotail is measured by the Auroral indices. The Auroral Lower (AL) index is built by plotting magnetic field (B_H) measurements from several ground-based magnetometer stations located at auroral latitudes together and taking the lower envelope (*Davis and Sugiura*, 1966). A sharp decrease of 100 nT over a few minutes in the AL index indicates the onset of a substorm. This is typically preceded by a slow decrease over tens of minutes, the substorm growth phase (*McPherron*, 1970, 1972). Once a minimum in the AL index is reached the recovery phase begins. This phase of the substorm can last for nearly an hour. SMC intervals occur when the AL index stays below -50 nT for more than 2 hours with few fluctuations (*Kissinger et al.*, 2012). These intervals typically begin with a substorm. Pseudo break-ups are substorms that never fully develop.

Substorms were originally studied by observing the aurora. As a result they are often referred to as auroral substorms. The sequence of events that occurs in auroral forms during a substorm was carefully noted by *Akasofu* (1964). One of the author's original sketches is shown in Figure 1.4. Auroral substorms begin with a quiet pre-existing arch in panel A. Panel B depicts an equatorward brightening of the arc. Panel C shows the beginning of

the auroral break-up and poleward expansion of the arc. The development of the westward traveling surge and the Harange reversal can also be seen in Panels C-E. Panel F shows the aurora retreating equatorward and eventually returning to the original state shown in Panel A after ∼2-3 hours.

The Pi2 category of ULF pulsations, discussed in detail in Section 1.3, has been shown to be directly related to substorms. The relationship is based on the fact that Pi2 pulsations begin in ground-based magnetometer records concurrently with other indicators of substorm onset including the decrease in the AL index and auroral break-up (*Saito et al.*, 1976; *Sakurai and Saito*, 1976; *Olson*, 1999; *Miyashita et al.*, 2000; *Kepko et al.*, 2004; *Hsu and McPherron*, 2007; *Kim et al.*, 2007; *Keiling et al.*, 2008). It has even been argued that Pi2 can bee seen as the first indicator of substorm onset (*Nagai et al.*, 1998; *Kepko et al.*, 2004; *Hsu et al.*, 2012). Understanding the sequence of events leading up to substorms, and Pi2 onset, is important because substorms are one of major avenues by which energy is transferred from the Sun through the solar wind, and into the Earth's ionosphere. For the remainder of this dissertation we focus on understanding Pi2 pulsations and their relationship to substorm phenomena.

Based on the Near Earth Neutral Line (NENL) paradigm for substorms (*McPherron et al.*, 1973; *Baker et al.*, 1996), onset is preceded by the initiation of reconnection at a neutral line that forms around -20 R_E in the tail. Fast flows are released earthward from the reconnecting region. As the fast flows reach the near-Earth region there is an injection of particles into the radiation belts and ionosphere and the substorm current wedge (SCW) forms (*McPherron*, 1972). The SCW is a current system that forms as a result of a partial collapse of the cross tail current. As a result of the current disruption some of the current is diverted along field lines to close in the ionosphere. The traditional image of the SCW is shown in Figure 1.5 which shows that with the collapse of the cross tail current, current is diverted into the ionosphere on the dawn side of the SCW , travels through the ionosphere in a westward direction, and leaves the ionosphere on the dusk side of the SCW along upward FACs. Although the general configuration of the SCW is well accepted the details of how and where the current closure takes place are still under debate.

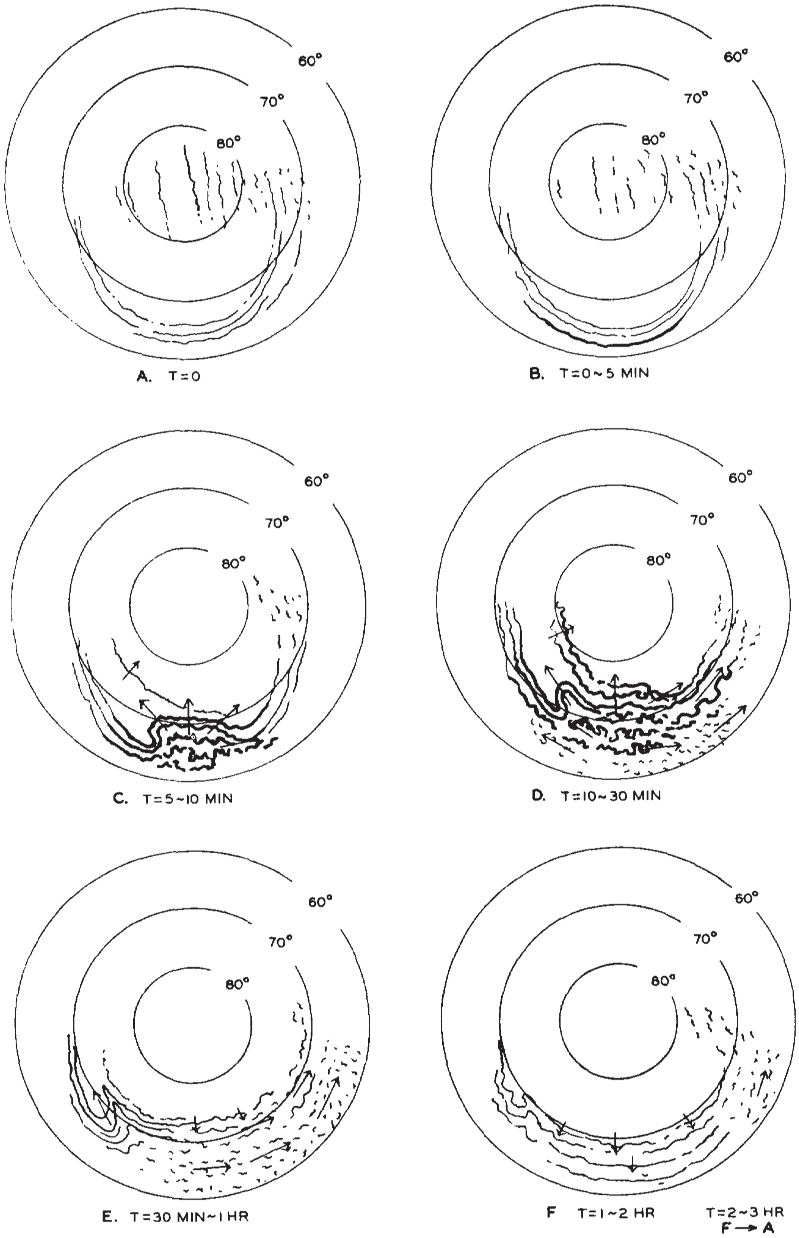

Figure 1.4: Illustration of the sequence of events during an auroral substorm over ∼3 hours (*Akasofu*, 1964).

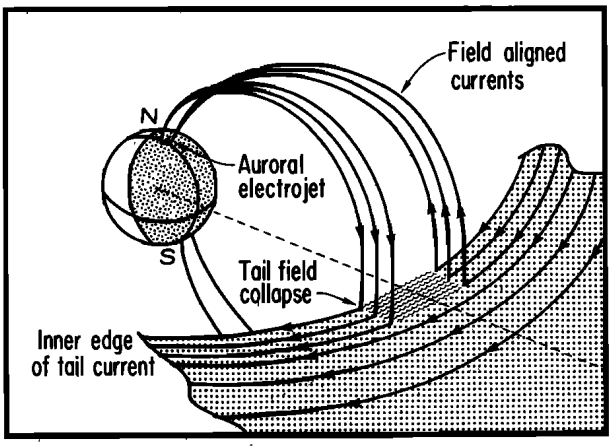

Figure 1.5: Illustration of the substorm current wedge (*McPherron et al.*, 1973).

Intermittent fast earthward flows ($|\vec{v}| > 100$ km/s), often referred to as bursty bulk flows (BBFs), are observed frequently in the tail (*Scholer et al.*, 1984; *Baumjohann et al.*, 1989; *Angelopoulos et al.*, 1992, 1994), and have been linked to reconnection events at neutral lines that form in the near-earth region between -15 and -25 R_E (*Pytte et al.*, 1976; *Hones et al.*, 1984; *Angelopoulos et al.*, 2008; *Nagai et al.*, 1998; *Miyashita et al.*, 2009; *Gabrielse et al.*, 2009). BBFs cause an increase in thermal pressure, and a magnetic pile-up and dipolarization in the plasma sheet as they travel earthward.

The leading edge of the plasma sheet dipolarization is referred to as a dipolarization front (DF), and develops at the boundary between the flowing plasma and the background plasma (*Runov et al.*, 2009, 2011). DFs are observed as enhancements in B_z that occur over the course of a few seconds. They are typically accompanied by a drop in B_x, and occur throughout the magnetotail from $x = -5$ to -31 R_E during disturbed periods as observed by satellites and in simulations (e.g., *Slavin et al.*, 1997; *Nakamura et al.*, 2009; *Sitnov et al.*, 2009; *Ashour-Abdalla et al.*, 2011). The dipolarization region behind a DF is sometimes referred to as an entropy bubble since it is associated with flux tubes that have decreased entropy content (*Pontius and Wolf*, 1990; *Chen and Wolf*, 1993; *Sergeev et al.*, 1996; *Chen and Wolf*, 1999; *Wolf et al.*, 2009). As the DFs encounter the region where the magnetic field lines transition from a stretched to a dipolar configuration there is a pile-up effect in the magnetic field that causes an expansion of the region in both tailward and azimuthal

directions (*Hesse and Birn*, 1991). This expansion is often referred to as dipolarization associated expansion. Pulsations in the Pi2 frequency band have been observed in magnetic field and velocity measurements both in the tail and at geosynchronous orbit in conjunction with dipolarization fronts (DFs) (*Kepko and Kivelson*, 1999). This has lead to the idea that the Pi2 pulsations observed at substorm onset are either generated by or concurrently with the DFs observed in association with substorms.

1.3 Properties of Pi2 Pulsations

Pi2 pulsations are ultra-low frequency (ULF) waves ($T = 40 - 150s$) that come in packets at irregular intervals. A thorough overview of the properties of ground-based Pi2 pulsations is given by *Olson* (1999) and *Keiling and Takahashi* (2011). *Saito and Matsushita* (1968) has shown that Pi2 periods also vary with the level of geomagnetic activity. Higher levels of geomagnetic activity such as those found during strong magnetic storms are associated with higher frequency Pi2 pulsations. The amplitude of the pulsations varies from tens of nano-tesla (nT) at high latitudes to a few nT at mid-latitudes. The spectral properties of Pi2 also vary significantly with latitude. At high latitudes, the Pi2 signature is disordered and contains several spectral peaks (*Stuart et al.*, 1979; *Samson*, 1982). The signatures at low and mid-latitudes are more sinusoidal, with only a single dominant spectral peak. The change in Pi2 spectra from high to mid-latitudes indicates that there is a mechanism acting to filter the pulsations in the inner magnetosphere. There has been speculation that the boundary between high latitude disordered Pi2 and the more ordered mid-latitude Pi2 is associated with the plasmapause and the way in which the pulsations propagate through the plasmasphere. The boundary may also be associated with the inner edge of the plasma sheet and the propagation of the pulsations as the plasma flows slow in the braking region. These possibilities are discussed further in Section 1.4.

The longitudinal extent of Pi2 on the ground also varies with latitude. At high latitudes Pi2 appear to be more confined to the location of the substorm current wedge (SCW) (*McPherron*, 1972; *Singer et al.*, 1983), whereas the mid- and low latitude pulsations are

more spread out, occurring over most of the nightside (*Yeoman et al.*, 1994). The pulsations are circularly polarized and it has been shown by *Lester et al.* (1983) that the center of the polarization pattern observed for Pi2 on the ground (discussed in Section1.3) and the center of the substorm current wedge (SCW) are co-located. When looking at high to mid-latitudes, fluctuations in the H and D components of the magnetic field are in phase at the location of substorm onset while at locations removed from the substorm onset the components are out of phase with the phase shift becoming greater at greater distances. In addition, *Sakurai and McPherron* (1983) found that the deflection of the D-component, B_D, that would be caused by the SCW is the same as the deflection of the D-component observed in Pi2 on the ground and at geosynchronous orbit. This suggests that the pulsations may be excited as a result of the formation of the SCW. With the current extensive arrays of ground-based magnetometers throughout North America it is possible to use Pi2 observations to identify both the timing and location of substorm onset (*Rae et al.*, 2009; *Murphy et al.*, 2011a).

Pi2 packets are typically very short lived, lasting ∼10-15 min, with only a few wave periods per packet (∼5). However, each substorm can have several Pi2 packets associated with it. In a statistical study by *Hsu and McPherron* (2007) the authors showed that, on average, there are two Pi2 packets generated during a substorm and that the packets are separated by ∼20 minutes.

As was indicated in Section 1.2, there have also been observations of pulsations with Pi2 properties observed in magnetic field and velocity measurements in space from geosynchronous orbit (*Kepko and Kivelson*, 1999) out as far as ∼-12 R_E (*Murphy et al.*, 2011b; *Cao et al.*, 2012; *Ream et al.*, 2013). These observations have lead to the models for Pi2 generation that will be described in the following section.

1.4 Existing Models for Pi2 Generation

Pi2 pulsations have been studied extensively for several decades, however, the source of the Pi2 observed on the ground is still a subject of debate (*Olson*, 1999; *Keiling and Takahashi*, 2011)[and refs therein]. Because mid-latitude Pi2 can be used to identify the onset time

of a substorm, understanding how they are generated is vital to understanding the series of events leading up to onset. There have been several models presented over the past decade to explain how Pi2 are generated in the magnetotail and propagate through the inner magnetosphere.

Well-correlated measurements of the phenomena have led to several theories concerning the relationship between Pi2 pulsations and DFs such as the Bursty Flow Model(*Kepko and Kivelson*, 1999; *Kepko et al.*, 2001) and the Pulsed Reconnection Model (*Keiling et al.*, 2008; *Murphy et al.*, 2011b). Recently, *Hsu et al.* (2012) used a statistical study to show that 90% of plasma flows in the tail are associated with Pi2's, indicating that either the plasma flows generate the Pi2 pulsations, or that the flows and Pi2s are generated by the same process. Another model that describes Pi2 generation in the near-earth plasma sheet is the Balloon Instability Model. There is also a set of models that describes the Pi2 period in the pulsations observed at substorm onset being filtered out from a broadband disturbance by mechanisms in the inner magnetosphere. This set of models includes the Plasmapause Surface Mode model (*Sutcliffe*, 1975; *Southwood and Stuart*, 1980), as well as the Plasmasphere Cavity Resonance model (*Saito and Matsushita*, 1968; *Yeoman and Orr*, 1989; *Sutcliffe and Yumoto*, 1991; *Takahashi et al.*, 1992), and its more generalized form, the Plasmasphere Virtual Resonance model.

Based on a recent review of Pi2 by *Keiling and Takahashi* (2011), there are at least seven different models for Pi2 generation with source regions ranging from the reconnection region in the tail to the plasmasphere. These models are listed in Table 1.2 with brief descriptions of the Pi2 generation location and mechanisms addressed in each model. We will briefly go through each of these models.

1.4.1 Plasmasphere Models

There are several models describing how the fluctuations propagate once they are in the inner magnetosphere. These models look at plasmasphere cavity modes, plasmapause surface waves, and field line resonances as sources for the pulsations observed on the ground. One

Table 1.2: List of Pi2 models with location and mechanism for Pi2 generation.

Model	**Location**	**Generation Mechanism**
Pulsed Reconnection	Near-earth reconnection site	changes in the reconnection rate generate fast mode pulses that travel earthward (*Keiling et al.*, 2006; *Murphy et al.*, 2011b)
Transient Response (high-latitude Pi2)	near-Earth plasma sheet	impedance mismatch causes Alfvén waves to be partially reflected and bounce between the northern and southern ionospheres (*Hughes*, 1974; *Southwood and Stuart*, 1980; *Webster et al.*, 1989)
Bursty Flow	plasma sheet and inner edge of the plasma sheet	Transient Response, flow modulations, and fast mode waves generated by flow bursts at the inner edge of the plasma sheet (*Kepko and Kivelson*, 1999; *Kepko et al.*, 2001, 2004)
Plasma Instability-Driven (high-latitude Pi2)	near-Earth plasma sheet	propagating and non-propagating periodic oscillations of ballooning modes (*Solovyev et al.*, 2000; *Keiling et al.*, 2008)
Plasmapause Surface Mode	plasmapause	earthward propagating compressional waves excite a surface wave on the plasmapause (*Sutcliffe*, 1975; *Southwood and Stuart*, 1980)
Plasmaspheric Cavity Resonance	plasmasphere	Earthward propagating compressional waves generate a trapped eigenmode in the plasmasphere (*Saito and Matsushita*, 1968; *Yeoman and Orr*, 1989; *Sutcliffe and Yumoto*, 1991; *Takahashi et al.*, 1992)
Plasmaspheric Virtual Resonance	plasmasphere	Earthward propagating compressional waves generate a trapped eigenmode in the plasmasphere with a boundary that is not a perfect reflector (*Lee and Lysak*, 1999; *Fujita et al.*, 2002)

model typical of the inner magnetosphere is the Plasmaspheric Virtual Resonance (PVR) model which states that a broadband compressional wave travels earthward from the inner edge of the plasma sheet and excites a fast mode wave that is trapped in the plasmasphere with the ionosphere and plasmapause acting as nearly perfect reflectors at the inner and outer boundaries (*Lee and Lysak*, 1999).

Each of the inner magnetosphere models for Pi2 generation require that a disturbance, presumably from the tail, must generate a broadband compressional pulse that travels earthward through the inner magnetosphere. Therefore, the model for Pi2 generation in the tail

by BBFs and those describing Pi2 generation in the inner magnetosphere are not mutually exclusive.

1.4.2 The Bursty Flow Model

The key feature of the bursty flow model is a causal relationship between DFs and Pi2 generation in the tail. *Kepko and Kivelson* (1999), *Kepko et al.* (2001) and *Kepko et al.* (2004) used satellite and ground-based observations to study Pi2 period fluctuations in the magnetic field at geosynchronous orbit and on the ground, and velocity perturbations further out in the magnetotail. The authors identified similar waveforms in each of the data sets and determined that variations associated with the DFs were generating the Pi2 observed at geosynchronous orbit and on the ground. Specifically, the authors argued that both the compression regions and time-variations in velocity associated with the braking of dipolarization fronts drive Pi2 pulsations. Based on the different drivers, the authors divided Pi2 pulsations into three distinct categories: Transient Response (TR), Inertial Current (IC) and Directly Driven (DD).

The model is summarized in Figure 1.6. TR and IC Pi2 pulsations are associated with the substorm current wedge (SCW) and are thought to arise because of an impedance mismatch between the ionosphere and magnetosphere as the DFs propagate earthward (*Southwood and Stuart*, 1980), and time variations in the flow velocity in the braking region (*Shiokawa et al.*, 1997; *Yumoto et al.*, 1989; *Nagai et al.*, 1998; *Kepko et al.*, 2001), respectively. Although both the TR and IC Pi2 are observed at mid- to high latitudes, they have slightly different signatures on the ground. Specifically, TR Pi2 have a damped sinusoidal form which continues after the driving flow has stopped, and IC Pi2 have a relatively constant amplitude and are only present while the flows are present. In addition, the waveforms of the IC Pi2 match the flow variations in the magnetotail while the TR Pi2 waveforms do not (*Kepko and Kivelson*, 1999; *Kepko et al.*, 2001).

Directly Driven (DD) Pi2 are caused by flow channels entering the high pressure region near the inner edge of the plasma sheet where field lines change from a stretched to a dipolar

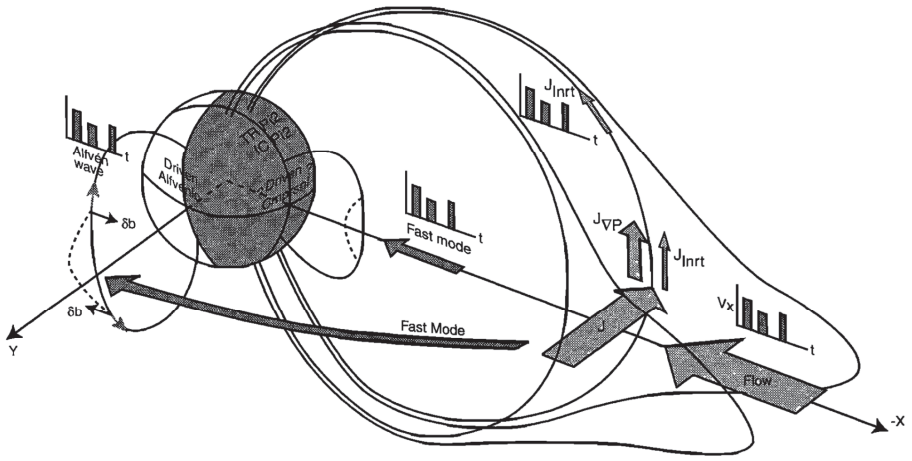

Figure 1.6: A summary of the bursty flow model for Pi2 generation from *Kepko et al.* (2001).

geometry. Each successive flow channel generates a compressional pulse, and several flow channels arriving at the inner edge of the plasma sheet generate a Pi2 packet that travels earthward across the background magnetic field (*Russell and McPherron*, 1973; *Chang and Lanzerotti*, 1975) to generate mid- to low-latitude Pi2 observed on the ground. Observations of Pi2 by *Uozumi et al.* (2009) verify the existence of shear waves that are generated by a compressional wave in agreement with the directly driven model for generation of mid- to low latitude Pi2.

Panov et al. (2010) extended the *Kepko et al.* (2001) interpretation suggesting that Pi2 pulsations are generated by the overshoot and rebound of bursty bulk flows (BBFs) at the braking region causing the compressional wave to travel earthward.

1.4.3 The Pulsed Reconnection Model

A slightly different model, referred to as the pulsed reconnection model, was proposed by *Keiling et al.* (2006) and *Keiling et al.* (2008). For this model the authors use observations from the Cluster spacecraft along with ground based magnetometer data to show that flow variations at the BBF cause Alfvén-mode waves to propagate along field lines, and fast-mode waves propagate earthward in the plasma sheet ahead of the BBF. An early reference to this mechanism for Pi2 generation was made by *Dungey* (1994) when he states "Another

enjoyable hand waving speculation suggests that Pi2 are the pizzicato form of pulsations, probably twanged by impulsive reconnection."

More recently, *Murphy et al.* (2011b) used Geotail and ground-based magnetometer observations to construct a set of scenarios which are possible in the pulsed reconnection model but not in the bursty flow model. In these scenarios reconnection generates both a bursty flow and a fast mode wave. The first scenario shows the fast mode traveling much faster than the bursty flow so that Pi2 are observed on the ground before the BBF is observed by Geotail. The second scenario shows the fast mode only slightly ahead of the BBF so that Geotail observed the BBF before the Pi2 were observed on the ground. Finally, the third scenario shows simultaneous observations of Pi2 on the ground and the BBF at Geotail.

This model is closely related to the Bursty Flow model in that they both suggest that variations in the pressure and in velocity associated with the earthward propagation of dipolarization fronts are related to the Pi2 pulsations measured by ground-based magnetometers. However, in the bursty flow model, the pulsations are generated by the flow channels, whereas, in the pulsed reconnection model, the Pi2 pulsations and the flow channel are generated concurrently at the reconnection site with the period of the pulsations determined by the reconnection rate.

1.4.4 The Instability Driven Model

A more recently proposed model for high latitude Pi2 generation is the instability driven model (*Keiling*, 2012). *Solovyev et al.* (2000) suggested that instabilities in the magnetotail could lead to phenomena such as Pi2 pulsations and spatial distortion of auroral arcs observed from the ground. *Keiling* (2012) takes this scenario further by identifying the drift ballooning mode in the near-Earth plasma sheet ($\sim 9 - 12\ R_E$) as the specific source for the Pi2 period pulsations observed from the ground. In this model Pi2 are a direct response to the period of the ballooning wave perturbations combined with a westward diamagnetic drift. Field-aligned currents then carry the disturbance from the ballooning unstable region into the ionosphere. *Keiling* (2012) also argues that different ballooning active regions

produce slightly different Pi2 signatures so the model can account for the multiple spectral peaks observed in Pi2 at high latitudes. The author notes that there are Pi2 observed by ground magnetometers in their case study that are not instability driven, but instead match the transient response description at high latitudes, and the plasmasphere cavity resonance description at mid- to low latitudes.

Based on the existing models for Pi2 generation there are at least 7 different generation mechanisms that may be responsible for generating Pi2 period pulsations. Most likely, several of the mechanisms described in the existing models are acting together to produce the Pi2 signatures observed by ground-based magnetometers for any given substorm event.

1.5 Methods

Each of the Pi2 models discussed in 1.4 tries to describe how the Pi2 signatures observed at different latitudes are generated. However, since all of the models were constructed by using satellite and ground-based data they only account for discrete point observations with large spatial separation. In order to properly identify the Pi2 driver we need a more global picture of the magnetotail. In order to obtain that large scale view of the magnetotail, we have decided to use global magnetohydrodynamic (MHD) simulations to approach the question of what is driving Pi2 in the tail.

In order to investigate the generation of Pi2 pulsations in the context of the global environment we will select several substorm events to model using a global MHD simulation of Earth's magnetosphere. The benefit of using a global simulation, rather than satellite measurements, is that we are able to track the flow channels and their related DFs as they propagate through the system rather than simply getting a glimpse of them as they pass by the spacecraft. This will allow us to get a more complete picture of how the flow channels are related to the generation of Pi2 pulsations since we will be able to observe how the signatures change as the disturbance propagates earthward.

1.5.1 Global Magnetohydrodynamic (MHD) Simulations

MHD simulations have been carried out with both the UCLA global MHD code and the Lyon-Fedder-Mobarry (LFM) Global MHD code to establish the magnetosphere's response to the solar wind conditions observed before and during the substorm event. The reason for using two different MHD models is twofold. First, we need to determine whether the results are code dependent. Given that these are small transient features in a very large system the computational grid and the numerical methods used in the models may impact the perturbations that develop in the simulation results. Using two different models allows us to investigate the robustness of the Pi2 results. Second, although it was not used in the current study, LFM has the capability to couple to an inner magnetosphere model which will allow studies involving wave propagation from the inner edge of the plasma sheet earthward. The developers of LFM have also done some simulations where they have incorporated a plasmasphere model and they are currently analyzing the preliminary results from those simulations [Michael Wiltberger, Personal communication, June 2013]. The inclusion of the plasmasphere will be of great use in Pi2 investigations because it will allow us to investigate how the Pi2 propagate to lower latitudes.

With some differences both models follow the set of ideal MHD equations which are a combination of Maxwell's equations and the fluid equations given below in SI units.

$$\frac{\partial \mathbf{B}}{\partial t} = -\nabla \times \mathbf{E} \qquad \text{(Faraday's Law)} \tag{1.1}$$

$$\mu_0 \mathbf{J} = \nabla \times \mathbf{B} \qquad \text{(Ampere's Law)} \tag{1.2}$$

$$\nabla \cdot \mathbf{B} = 0 \tag{1.3}$$

$$\frac{\partial \rho}{\partial t} + \nabla \cdot (\rho \mathbf{v}) = 0 \qquad \text{(Continuity)} \tag{1.4}$$

$$\rho\left(\frac{\partial}{\partial t}+\mathbf{v}\cdot\nabla\right)\mathbf{v}=\mathbf{J}\times\mathbf{B}-\nabla p \qquad \text{(Momentum)} \tag{1.5}$$

$$\frac{\partial}{\partial t}\frac{p}{\rho^{\gamma}}=0 \qquad \text{(Energy)} \tag{1.6}$$

$$\mathbf{E}+\mathbf{v}\times\mathbf{B}=0 \qquad \text{(Ideal Ohm's Law).} \tag{1.7}$$

In this set of equations $\mathbf{B}$ $[T]$ is the magnetic field, $\mathbf{E}$ $[V/m]$ is the electric field, $\mathbf{v}$ $[m/s]$ is the bulk velocity, ρ $[kg/m^3]$ is the mass density, p $[Pa]$ is the pressure, γ is the adiabatic index, $\mathbf{J}$ $[A/m^2]$ is the current density, and μ_0 is the permeability of free space.

Each of the two models uses different methods for solving the set of MHD equations. In some cases the equations themselves are rewritten and additional terms are included. For example the UCLA model solves the resistive MHD equations which includes an anomalous resistivity term in Ohm's law. In addition, both of the models use normalized parameters when solving the MHD equations on the computational grid. The normalized parameters are then converted to the appropriate units for input into the ionospheric models. Descriptions of the two simulation are given in the following sections.

1.5.1.1 The UCLA 3D Global MHD Model

The UCLA global MHD code is a coupled magnetosphere-ionosphere three-dimensional global MHD code based on a one-fluid description of the interaction between the solar wind and the magnetosphere. This code is discussed in detail by *Raeder et al.* (1996), *Raeder et al.* (1998) and *El-Alaoui* (2001). The simulation box is 20 to -300 R_E in x, and 55 to -55 R_E in y and z, GSM, and uses a non-uniform Cartesian grid with the minimum grid spacing set at 0.15 R_E.

As mentioned above, the equations used in the model differ slightly from the ideal MHD equations. First, the electric field in the code includes both convective and resistive terms $\mathbf{E}=-\mathbf{v}\times\mathbf{B}+\eta\mathbf{j}$ where $\mathbf{j}$ is the current, $\mathbf{B}$ is the magnetic field, $\mathbf{E}$ is the electric field, and

η is the anomalous resistivity. This anomalous resistivity is defined by

$$\eta = \alpha j'^2 \quad if \quad j' \geq \delta, \quad 0 \ otherwise \tag{1.8}$$

$$j' = \frac{\mid j \mid \Delta}{\mid B \mid + \epsilon} \tag{1.9}$$

where j' is the normalized current density, Δ is the grid spacing, j is the local current, B is the local magnetic field, and ϵ is used to avoid dividing by zero. The quantities α and δ are set such that the resistivity is only non-zero in strong current sheets.

Another difference is in the energy and momentum equations. In the UCLA model Equation 1.5 is written in the form

$$\frac{\partial \rho \mathbf{v}}{\partial t} = -\nabla \cdot (\rho \mathbf{v}\mathbf{v} + p\underline{\mathbf{I}}) + \mathbf{J} \times \mathbf{B} \qquad \text{(UCLA Momentum)} \tag{1.10}$$

where $\underline{\mathbf{I}}$ is the identity matrix. The energy equation is written as

$$\frac{\partial \epsilon}{\partial t} = -\nabla \cdot (\{\epsilon + p\}\mathbf{v}) + \mathbf{J} \cdot \mathbf{E} \qquad \text{(UCLA Energy)} \tag{1.11}$$

$$\epsilon = \frac{1}{2}\rho v^2 + \frac{p}{\gamma - 1} \tag{1.12}$$

where ϵ $[J]$ includes both thermal and kinetic contributions as shown in Equation 1.12. The $\mathbf{J} \times \mathbf{B}$ and $\mathbf{J} \cdot \mathbf{E}$ terms are included as source terms since the large magnetic field gradients and low plasma β in the near-Earth region do not allow for the full conservative form of the MHD equations (*Raeder et al.*, 1996).

Open (i.e., zero normal derivative) boundary conditions are applied to all outer boundaries except the sunward boundary. The sunward outer boundary conditions are set to the time dependent solar wind conditions (magnetic field, velocity, density and temperature) measured by an available solar wind monitor (ACE, Geotail, THEMIS, etc.). To prepare the solar wind data for input into the simulation, magnetic field measurements are rotated

into a minimum variance frame. The normal component of the magnetic field is then set to a constant. The method outlined here is used to propagate the solar wind parameters from the solar wind monitor to the inflow boundary and keeps divergence of $\mathbf{B}$ equal to zero at the outer boundary (*El-Alaoui*, 2001). The benefit of treating the solar wind input in this way is that it allows the inclusion of time variation in each of the components of the solar wind magnetic field while maintaining $\nabla \cdot \mathbf{B} = 0$ at the sunward boundary. The conditions imposed on the inner boundary will be discussed in detail in Section 1.5.2

The code uses a finite difference method to solve the normalized resistive MHD equations on the grid. The equations are solved using a fourth order spatial differencing with a predictor-corrector scheme that is second order accurate in time. Since only the gas dynamic equations are strictly conserved with the finite difference method the constrained transport method (*Evans and Hawley*, 1988) is used when solving the magnetic induction equation. The constrained transport method used in conjunction with a grid where the magnetic field quantities are offset from the plasma parameters by half a grid spacing ensures that $\nabla \cdot \mathbf{B} = 0$ is maintained throughout the grid.

1.5.1.2 Lyon-Fedder-Mobarry Global MHD Model

The LFM simulation is described in great detail in *Lyon et al.* (2004), and the specific numerical methods are discussed in *Lyon* (2007). The basic idea of the two codes is similar but there are several key differences between the UCLA model and the LFM model. Perhaps the most obvious difference is that LFM uses a non-orthogonal distorted spherical grid, as opposed to the stretched Cartesian grid used by the UCLA model. The grid boundary is a cylindrical shell. Boundaries in the ϕ and θ directions are periodic and the boundaries in the radial direction are divided into internal and external boundaries. The external boundary is where the solar wind measurements are input. The solar wind is assumed to be made up of planar fronts much like the UCLA model, but rather than using a minimum variance frame to keep variations in all three Cartesian components of the solar wind, the LFM model assumes $B_x = 0$. Because the solar wind B_x is not amplified across the bow shock this assumption

does not dramatically affect the simulation results. The internal boundary will be discussed in the Section 1.5.2.

Lyon et al. (2004) states that there were several considerations that went into developing the LFM code. These considerations were the grid described above, $\nabla \cdot B = 0$, regions with high Alfvén speed, low β, or high magnetic field, and coupling to the ionospheric model. LFM maintains $\nabla \cdot B = 0$ using a *total variation diminishing* (TVD) scheme in conjunction with a grid that has the magnetic field offset from the plasma parameters by half a grid spacing. The TVD scheme is a method used to mediate problems that arise when using numerical schemes that use linear operators to solve hyperbolic systems (like the ideal MHD equations). The basic idea is to determine where diffusion is necessary in order to control unnatural oscillations that arise in the system. As a result the amount of diffusion is increased in regions with steep gradients, and minimized in regions where the flow is smooth. As you move closer to the planet the magnetic field and Alfvén speed get very large. LFM handles this by setting the inner edge of the MHD calculations to $\sim 3\ R_E$ and using a Boris correction on the flows.

The final form for the LFM momentum equation is

$$\frac{\partial \rho \mathbf{v}}{\partial t} = -\nabla \cdot (\rho \mathbf{v}\mathbf{v} + p\underline{\mathbf{I}}) - \nabla \cdot \left(\underline{\mathbf{I}} \frac{B^2}{8\pi} - \frac{\mathbf{B}\mathbf{B}}{4\pi} \right) \qquad \text{(LFM Momentum)}. \tag{1.13}$$

The difference between Equations 1.10 and 1.13 is the LFM equation set is written in Gaussian units whereas the UCLA equations are written in SI units where $\mathbf{B}$ $[Gs]$ is the magnetic field, $\mathbf{v}$ $[cm/s]$, ρ $[gm/cm^3]$ is the mass density, and p $[dyne/cm^2]$ is the pressure. In addition the $\mathbf{J} \times \mathbf{B}$ term has been rewritten using some vector algebra.

In order to addresses the low plasma β consideration LFM uses an energy equation that includes only the thermal and kinetic contributions. The final form of the LFM energy equation is

$$\frac{\partial \epsilon}{\partial t} = -\nabla \cdot \left(\mathbf{v} \left(\frac{\rho v^2}{2} + \frac{\gamma}{\gamma - 1} p \right) \right) - \mathbf{v} \cdot \nabla \cdot \left(\underline{\mathbf{I}} \frac{B^2}{8\pi} - \frac{\mathbf{B}\mathbf{B}}{4\pi} \right) \qquad \text{(LFM Energy)}. \tag{1.14}$$

where ϵ $[ergs]$ is referred to as the fluid (plasma) energy (*Lyon et al.*, 2004). This set of equations is very similar to those used in the UCLA model except the $\mathbf{J} \cdot \mathbf{E}$ term in Equation 1.14 has been written as velocity dotted with the magnetic force.

Also, Faraday's Law has been rewritten using the ideal Ohm's law so it takes the form

$$\frac{\partial \mathbf{B}}{\partial t} = \nabla \times (\mathbf{v} \times \mathbf{B}). \tag{1.15}$$

Although the LFM model uses Gaussian units in its formulation all of the results have been converted to SI units for comparison to the UCLA model results.

Like the UCLA model, the LFM model uses a grid where the magnetic field quantities are offset from the plasma parameters by half a grid spacing. As a result the quantities on the cell faces are not directly computed. Instead, the mean magnetic field threading the face is used. The magnetic field is updated using Faraday's Law with Stokes Theorem with the integral computed along the edges of the cell that enclose the given face. $\nabla \cdot B = 0$ is conserved since the flux entering the cell is the same as the flux leaving the cell. Since the action of an electric field along the edge of a cell leaves $\nabla \cdot B$ unchanged the TVD scheme can modify the electric field locally while conserving the solenoidal behavior of $\vec{B}$ (*Lyon et al.*, 2004).

1.5.2 Ionospheric Boundary

The treatment of the boundary conditions differs between the two models. This is where the MHD variables are coupled to the ionosphere via the parallel currents by using the ionospheric potential equation

$$\nabla \cdot \overline{\overline{\Sigma}} \cdot \nabla \Phi = -j_{\parallel} \sin I \tag{1.16}$$

where $\Phi[V/m]$ is the ionospheric potential as a function of magnetic latitude and local time, $\Sigma[S]$ is the tensor of the ionospheric conductance including Hall and Pedersen conductances, $j_{||}[A/m^2]$ is the mapped FAC with the downward current considered positive and corrected

for flux tube convergence, and I is the inclination of the dipole field at the ionosphere (*Raeder et al.*, 1998). For the inner boundary, both simulations include ionospheric conductance models based Solar EUV and particle precipitation. In addition, both models use the formula presented by *Robinson et al.* (1987), which accounts for ionization arising particle precipitation to solve for the Hall and Pedersen conductances in the ionosphere.

$$\Sigma_P = \frac{40\epsilon}{16+\epsilon^2} F_\epsilon^{\frac{1}{2}} \tag{1.17}$$

$$\Sigma_H = 0.45(\epsilon)^{0.85}\Sigma_P \tag{1.18}$$

Here Σ_H is the Hall conductance, Σ_P is the Petersen conductance in $mhos$, ϵ is the mean energy in keV, and F_ϵ is the energy flux in $ergs/cm^2s$. Although both models use the Robinson formula they use very different methods to calculate the solar EUV contribution and to solve for the mean energy and energy flux to use in Equations 1.17 and 1.18. The ionospheric models for the simulations are described in detail in Sections 1.5.2.1 (UCLA) and 1.5.2.2 (LFM).

1.5.2.1 UCLA Ionosphere

The inner boundary for the UCLA simulation is a spherical shell placed at a radius of 2.7 R_E. As indicated above, the conductance distribution in the model is determined by using solar EUV, as well as discrete and diffuse precipitation, self-consistently with the MHD model (*Raeder et al.*, 1998, 2001; *El-Alaoui et al.*, 2009). Because the UCLA model is calculated in SI units, all parameters are converted to Gaussian units for input into the ionospheric model.

The solar EUV contribution to the conductivity is based on the empirical model described by *Moen and Brekke* (1993). It is temporally fixed but varies spatially based on solar zenith angle (χ) and the solar flux index as observed at 10.7 cm ($F_{10.7}$ $10^{-22}W/m^2Hz$). The resulting

conductances are given in [mhos].

$$\begin{aligned} \Sigma_H &= (F_{10.7})^{0.53}(0.81k + 0.54k^{1/2}) \\ \Sigma_P &= (F_{10.7})^{0.49}(0.34k + 0.93k^{1/2}) \\ k &= cos\chi \end{aligned} \tag{1.19}$$

To account for the discrete auroral contribution to the conductance, the UCLA model uses the precipitation model proposed by *Knight* (1973) and *Lyons et al.* (1979) to calculate the mean energy (ϵ_0 $[keV]$) and energy flux (F_ϵ $[ergs/cm^2s]$) of precipitating electrons that have been accelerated by a parallel potential drop ($\Delta\Phi_{||}$) (see also *Fridman and Lemaire*, 1980):

$$\begin{aligned} F_\epsilon &= \Delta\Phi_{||}|j_{||}| \\ \epsilon_0 &= e\Delta\Phi_{||} \\ \Delta\Phi_{||} &= \left(\frac{\sqrt{2\pi m_e kT_e}}{e^2 n_e}\right) max(0, -j_{||}) \end{aligned} \tag{1.20}$$

where e, m_e, n_e $[cm^{-3}]$, and T_e $[K]$ are the electron charge, mass, density and temperature respectively, taken at a radial distance of 3.7 R_E. The current density is taken in $[A/m^2]$. The model assumes steady state and incorporates precipitation only in regions of upward field-aligned currents.

To account for the diffuse auroral contribution, following *Kennel and Petschek* (1966), the ionospheric model used in the UCLA simulation assumes that the electron distributions become isotropic at a radial distance of 3.7 R_E. So the equations for the diffuse precipitation are given as:

$$\begin{aligned} F_\epsilon &= n_e kT_e \left(\frac{kT_e}{2\pi m_e}\right)^{1/2} \\ \epsilon_0 &= kT_e \end{aligned} \tag{1.21}$$

where the electron charge, mass, density and temperature are, again, taken at a radial distance of 3.7 R_E. Equations 1.20 and 1.21 are added together for use in the Robinson formula (Equations 1.17 and 1.18.

Equation 1.16 is solved on the surface of a sphere with radius 1.015 R_E, an altitude of 110

km, using the mapped FAC and the computed conductances. The potential is then mapped along field lines up to the inner edge of the MHD model where it is used as a boundary condition for the flows, $\mathbf{v} = -\nabla\Phi \times \mathbf{B}/B^2$.

1.5.2.2 LFM Ionosphere

The ionospheric model used in LFM is the Magnetosphere Ionosphere Coupler/Solver or MIX code which has been described in detail in *Fedder et al.* (1995) and *Wiltberger et al.* (2009). The code's primary function is to use existing empirical models for ionospheric conductance to find the electrostatic potential solution for a given event.

The solar EUV contribution to the conductances is calculated based on fits to incoherent scatter radar data using solar flux index as observed at 10.7 cm. The equations are broken up into bins of solar zenith angle for the Pedersen and Hall conductances in *mhos*:

$$\begin{aligned}
\Sigma_P &= 0.5F_{10.7}^{2/3}cos(\chi)^{2/3} \qquad \chi \leq 65^\circ \\
\Sigma_P &= \Sigma_P^{65^\circ} - 0.12F_{10.7}^{2/3}cos(\chi - 65^\circ) \qquad 65^\circ < \chi \leq 100^\circ \\
\Sigma_P &= \Sigma_P^{100^\circ} - 0.065F_{10.7}^{2/3}cos(\chi - 100^\circ) \qquad \chi > 100^\circ
\end{aligned} \tag{1.22}$$

$$\begin{aligned}
\Sigma_H &= 1.8F_{10.7}^{1/2}cos(\chi) \qquad \chi \leq 65^\circ \\
\Sigma_H &= \Sigma_H^{65^\circ} - 0.49F_{10.7}^{1/2}cos(\chi - 65^\circ) \qquad \chi > 65^\circ
\end{aligned} \tag{1.23}$$

The same method for calculating ionospheric conductances has been used in AMIE studies (*Richmond and Kamide*, 1988). This is similar to the solar EUV model used in the UCLA simulation in that it creates a temporally fixed profile that varies with solar zenith angle. It also allows for the inclusion of seasonal and diurnal variations in the model.

For the contribution from precipitating electrons the MIX calculates the thermal flux (F_0 $[cm^{-2}s^{-1}]$) and mean energy (E $[keV]$) of the precipitating electrons by first calculating the initial energy (E_0) and thermal flux using the sound speed and the plasma density at the

inner boundary of the MHD region in the simulation.

$$\begin{aligned} \epsilon_0 &= \alpha c_s^2 \\ F_0 &= \beta \rho \epsilon_0^{1/2} \end{aligned} \tag{1.24}$$

Here c_s $[cm/s]$ is the sound speed and ρ $[gm/cm^3]$ is the density at inner edge of the simulation grid. Constants α and β are used in the equations for number flux and mean energy to scale the precipitation energy to reasonable values in order to obtain results for the conductances that are consistent with measurements (*Slinker et al.*, 1999).

Next, following work by *Chiu and Cornwall* (1980) and *Chiu et al.* (1981), the field aligned electric potential energy difference between the inner boundary of the simulation grid and the ionosphere is calculated via:

$$\epsilon_{||} = \frac{R J_{||} \epsilon_0^{1/2}}{\rho} \tag{1.25}$$

where $J_{||}$ $[A/m^2]$ is the current density and a scaling factor (R) that is proportional to the electron velocity is used in this step to include an effective resistivity to the field-aligned currents that is taken to be 5 times larger for upward current than for downward current. This accounts for the stronger electric field required to draw 'hot' electrons from the magnetosphere into the ionosphere than that required to draw 'cold' electrons out of the ionosphere.

Finally, the effects of the field-aligned potential on the electron flux in a geomagnetic mirror field are accounted for based on work by *Owens and Fedder* (1978). The final forms of the energy (ϵ $[keV]$) and electron number flux (F $[cm^{-2}s^{-1}]$) are:

$$\begin{aligned} F &= F_0 \left(8 - 7e^{\frac{-\epsilon_{||}}{7\epsilon_0}} \right) \qquad \epsilon_{||} > 0 \\ F &= F_0 e^{\frac{\epsilon_{||}}{\epsilon_0}} \qquad \epsilon_{||} < 0 \\ \epsilon &= \epsilon_0 + \epsilon_{||} \end{aligned} \tag{1.26}$$

The coupling between MIX and LFM is accomplished via field aligned currents and the potential solution is used as a boundary condition for the velocity in the MHD region of the

simulation, in the same manner as in the UCLA model.

1.5.3 Limitations of MHD Models

Magnetohydrodynamics (MHD) is a fluid approximation to a plasma that can be found by taking the macroscopic moments of the Vlasov equation (the equation for a collisionless plasma). The moments tell you about the density, bulk velocity, pressure and temperature of the of the plasma rather than how the individual particles are behaving. As a result MHD cannot give information about phenomena caused by particle-particle or wave-particle interactions. Each moment depends on the next higher moment so the system must be truncated in order to form a closed set of equations. This is typically done by taking an equation of state for the pressure to avoid the necessity of solving for the heat flux. The equation of state used in the LFM and UCLA models is $p\rho^{-\gamma} = constant$ where $\gamma = 5/3$ as indicated in Equation 1.6 in Section 1.5.1. So the density and temperature of the plasma evolve adiabatically. In addition, the models used in this study assume isotropic pressure so any effects of pressure anisotropy are neglected.

The set of equations is simplified further by neglecting the difference between particle species. The number density, mass, and velocity are taken to be a combination of the individual species variables. The models also assume quasi-neutrality. As a result any effects of interactions between different particle species are also neglected. The frozen-in condition, in which the particles are tied to the magnetic field lines, requires that some additional assumptions be made to reduce the generalized Ohm's law

$$\mathbf{E} + \mathbf{v} \times \mathbf{B} = \eta \mathbf{j} + \frac{1}{ne}\mathbf{j} \times \mathbf{B} - \frac{1}{ne}\nabla \cdot \mathbf{P_e} + \frac{m_e}{ne^2}\frac{\partial \mathbf{j}}{\partial t} \tag{1.27}$$

to the ideal Ohm's law $\mathbf{E} = -\mathbf{v} \times \mathbf{B}$. The electron pressure gradient is neglected to eliminate the third term on the right. Slow time variations in the current density are also neglected eliminating the fourth term on the right. Because transverse currents are small throughout most of the system, the Hall term (second term on the right) is also neglected. The first term on the right is included in regions of large current density in the UCLA model in order

to allow for reconnection. In the LFM model the numerical resistivity is large enough to allow for reconnection to take place so no additional resistivity is included.

In addition to the general limitations on MHD models, both the UCLA and LFM models used in this study are limited by the fact that they do not include an inner magnetosphere. The physical processes that occur in regions of the plasmasphere, ring current, and radiation belts are completely neglected. As a result we limit our analysis to the region outside of 6 R_E and do not evaluate the Pi2 models that describe generation of Pi2 by physical processes in the inner magnetosphere.

By approaching the question of how Pi2 pulsations are generated using global MHD simulations we will be able to determine if the DFs observed in the system are responsible for the generation of the Pi2 pulsations in the inner magnetosphere. We will also be able to track the Pi2 period perturbations from their point of origin in the tail into the inner magnetosphere. This method eliminates the need to make assumptions concerning what happens between discrete point observations in the magnetosphere afforded by satellite observations and instead lets us look at the entire system.

1.6 Major topics addressed in the dissertation

There are several outstanding questions concerning how Pi2 pulsations are generated and how they propagate earthward to produce the signatures observed on the ground. We investigated the following aspects of Pi2 generation in the magnetotail:

1. **Identify the relationship between flow channels, DFs, and Pi2 pulsations in MHD simulations.** We identify earthward flow channels and their associated DFs in the tail in a case study with the UCLA global MHD simulation. The simulation results are then used to investigate the perturbations associated with the flow channels observed in the near the time of onset.

2. **Identify how the Pi2 period perturbations change as they approach and pass through the braking region.** We identify the wave modes and phase shift

as perturbations related to flow channels/DFs as they approach and pass through the braking region. We also investigate the amplitude of the Pi2 perturbations to determine what changes the perturbations experience as they pass through the braking region into the inner magnetosphere.

3. **Compare the MHD results to the existing models for Pi2 generation.** We use the simulations to distinguish between the drivers for Pi2 that would be observed at different latitudes on the ground in order to compare the results to the bursty flow model. To compare the results to the pulsed reconnection model we determine whether there are Pi2 period perturbations present in the reconnection regions responsible for generating the fast flows.

4. **Propose a model for Pi2 generation based on MHD Results**. Results from both the UCLA MHD Model and the LFM Model are used to develop the Pi2 model. We use the field aligned current, magnetic field, pressure and velocity perturbations in the MHD results to distinguish between TR, IC, and DD Pi2 and their different driving mechanisms.

CHAPTER 2

Using MHD Simulations to Study Pi2 Pulsations

We use a global magnetohydrodynamic (MHD) simulation event study of a substorm on September 14, 2004 to investigate fluctuations in plasma properties of the magnetotail in the Pi2 range and their relationship to fast earthward flows and their associated dipolarization fronts (DFs). This is the first time a global MHD simulation has been used to study Pi2 pulsations.

The first step in this project to determine whether Pi2 pulsations can be observed in a global MHD simulation. Next we focus on the time surrounding substorm onset to determine how the Pi2 pulsations are related to the fast flows and DFs observed in the simulation. We also follow the perturbations associated with the fast flows from their point of origin into the geosynchronous orbit to determine how the perturbations propagate through the system. The major results are that Pi2 can be identified in a global MHD simulation and they are directly associated with the observed fast flows that originate from reconnection regions in the tail.

When we focus on the dipolarization front (DF) at the earthward edge of the fast flow channel at onset, we observe fluctuations at Pi2 frequencies in the magnetic field, velocity, and pressure. There are very distinct changes in the signatures as the perturbations pass through the braking region into the inner magnetosphere. These changes are discussed briefly here and will be discussed in greater detail in Chapter 3.

2.1 Observations

The event we have selected for this study is a substorm on September 14, 2004 whose properties have previously been reported on by *Cao et al.* (2008, 2012) based on Double Star and Cluster observations. This event was selected because it is an example of moderate to high levels of activity with Pi2 observations available on the ground and in the plasma sheet.

Pi2 onset measured by the Urumqi magnetometer (northwest China; 48 MLAT) occurs at ∼18:22 UT as shown in Figure 2.1. Data are from the World Data Center [http://wdc.kugi.kyoto-u.ac.jp]. The instrument observed a burst of Pi2 pulsations at ∼1822-1834 UT with a smaller burst around 1845 UT. The period of the observed Pi2s is ∼60-90 seconds. The Norlisk (NOK) magnetometer in Russia (mLat 59.50) *Gjerloev* (2009, 2012) observed a drop of ∼700 nT in the northward component beginning at 1821 UT and confirms the Pi2 timing (not shown). The AL index *Davis and Sugiura* (1966)(Figure 2.2), however, shows a period of moderate activity between 1715 UT and 1820 UT followed by an expansion phase beginning at ∼1828 UT; 6 minutes after Pi2 onset. At this time the AL index decreases sharply from -150, reaching a minimum of -857 at 1844 UT. In fact, each of the measurements that can be used to identify substorm onset show slightly different times. Measurements of the mid-latitude bay gives the onset time as 1827 UT (*Chu et al.*, 2015). The SuperMag ground-based magnetometer data set (*Newell and Gjerloev*, 2011) shows several onset times at 1704 UT, 1737 UT, 1827 UT, 1847 UT, and 1920 UT. This indicates that each of the intervals with large fluctuations in the AL index is a minor substorm or a pseudo breakup. Substorm onset based on observations by the IMAGE satellite (*Mende et al.*, 2001) give the onset time as 1825 UT (*Liou*, 2010). With so many different onset times given using different methods it is not surprising that the Pi2 onset and the AL substorm onset do not agree. The entire interval from 1700UT to 1930 UT is very disturbed. In general, all of the ground-based data sets show an onset at 1827-1828 UT. This is the largest substorm identified by any method during the interval and it is the one we focus on in our analysis.

The data available in the plasma sheet during this event are from Double Star (TC1) located at (-10.2, -1.6, 1.2) R_E GSM. The data used in this study come from the Fluxgate

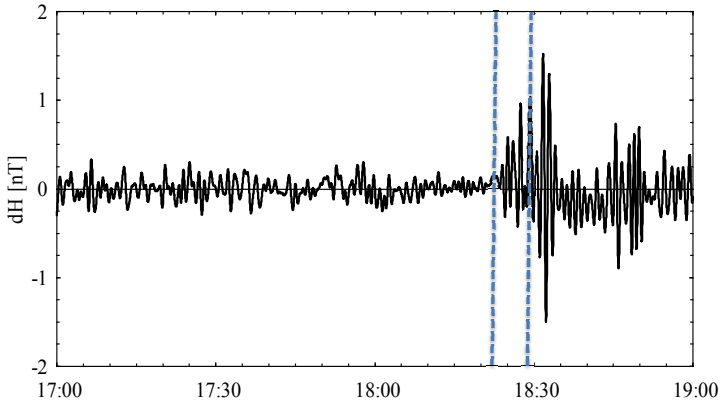

Figure 2.1: Detrended B_H from the ground magnetometer in Urumqi, China. The station is located at 43.80° latitude and 87.70° longitude, (33.4° magnetic latitude). At the time of substorm onset (1828 UT) the station is located at 0222 MLT.

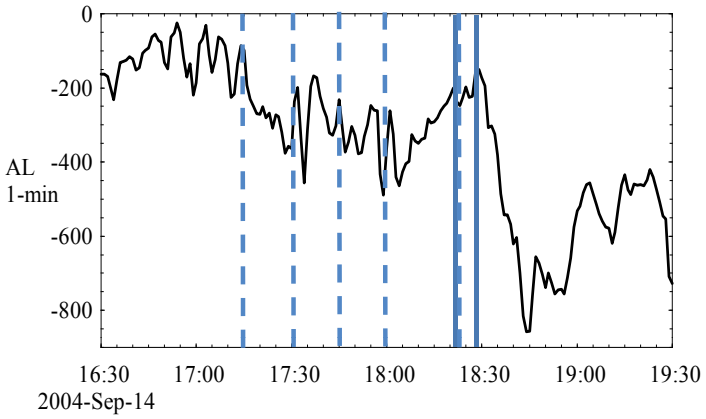

Figure 2.2: The 1 minute AL index during the substorm on 14-Sept-2004 (1630-1930 UT) from the OMNI database. The solid vertical lines indicate Pi2 onset (∼1822 UT) and substorm onset (∼1828 UT) as identified using ground-based magnetometer data, AL and IMAGE observations. The dashed vertical lines indicate the times when bursts of DFs are observed in the simulation.

Magnetometers (FGM) (*Carr et al.*, 2005) aboard the satellite. TC1 is located very close to the central plasma sheet (CPS) around the time of substorm onset, which is the ideal position to observe DFs propagating earthward/tailward in the magnetotail. Figure 2.3a shows the magnetic field measurements from TC1. There is an interval from ∼1755 to ∼1825 UT when TC1 is near the edge of the plasma sheet. During this interval B_x becomes very large and B_z becomes very small. It is possible that the plasma sheet became very thin during this interval. Figure 2.3b expands the plots of B_z (blue) and B_x (red) for the interval between the solid blue lines (1815 to 1850 UT). Three DFs were observed by TC1 at ∼1825, 1830, and 1844 UT, with the possibility of a fourth DF at 1837. The signatures are identified as sharp jumps in B_z with corresponding decreases in B_x, and are marked with gray arrows in Figure 2.3b. TC1 also observed Pi2 pulsations beginning at 1821 UT (Figure 2.4a), just before the first DF was observed as shown in Figure 2.3, and ∼1-2 minutes before Pi2 onset on the ground. This suggests a relationship between the two phenomena.

We use Geotail, which was located just outside the bow shock at ∼(25, 17, -2) R_E GSM, as the solar wind probe for this event (*Frank et al.*, 1994; *Kokubun et al.*, 1994). A small time shift (<2 minutes) was applied to propagate the measurements to the bow shock. Geotail measurements are shown in Figure 2.5. The panels show a) magnetic field B_x (black), B_y (blue), and B_z (red), b) v_x, c) v_y (black) and v_z (red), d) density, and e) temperature. The observations show a period where the IMF is dominated by B_y between 1640 and 1730 UT. The IMF turns slightly southward at ∼1707 UT and becomes more negative at 1730 UT. A strong northward turning occurs at ∼1830 UT, coincident with the beginning of the expansion phase in AL.

Satellite and ground-based observations for this event are discussed in detail by *Cao et al.* (2008). The authors used the timing between observations of magnetic dipolarization at TC1 and Cluster 4 (located outside of the plasma sheet until ∼1850 UT) along with multi-point analysis techniques (*Nakamura et al.*, 2005) to suggest that the tailward boundary of the dipolarization region propagates tailward at a speed of ∼86 km/s. They also relate the tailward expansion of the magnetic dipolarization to poleward expansion of auroral bulges observed by the IMAGE spacecraft (*Mende et al.*, 2001). Pre-onset auroral signatures for

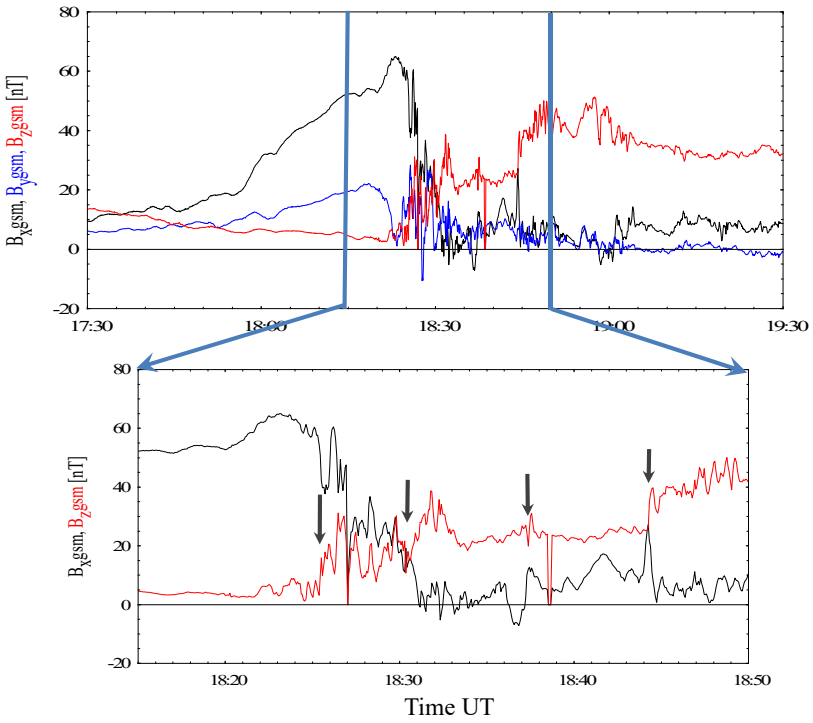

Figure 2.3: a) Magnetic field measurements B_x (black), B_y (blue), and B_z (red) for Double Star (TC1) for the time period 14-Sep-2004 1730–1930 UT. Pi2 onset (1822 UT) from ground magnetometer observations, and substorm onset (1828 UT) based on the AL index are indicated by the gray dashed lines. b) B_z (red) and B_x (black) during the interval 1815-1850 UT (indicated by the blue solid lines in panel a). The arrows indicate times of DFs.

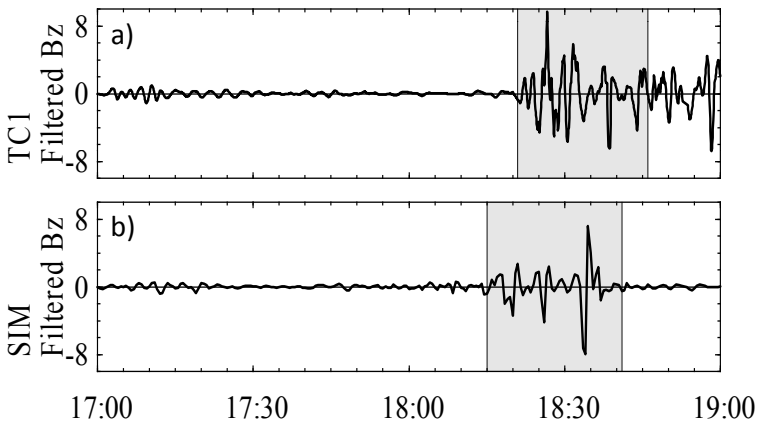

Figure 2.4: Filtered B_Z for a) TC1 and b) Simulation results near the TC1 location. The times for Pi2 onset in the two panels are offset by 5 minutes. The gray areas indicate times when the Pi2 in the simulation correspond to the TC1 measurements.

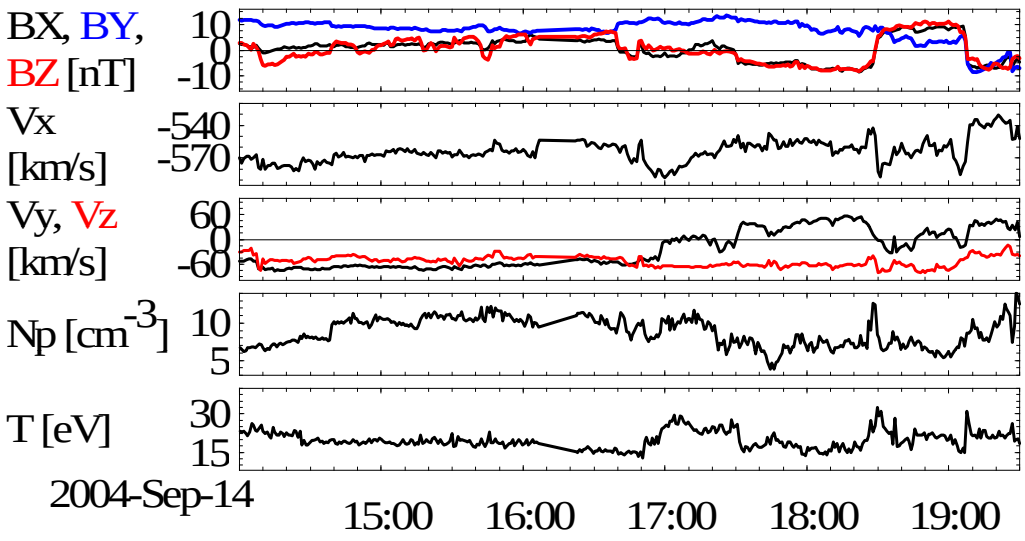

Figure 2.5: Geotail solar wind measurements for September 14, 2004 1400–1930 UT used for input in the MHD simulation. a) Magnetic field B_x (black), B_y (blue), and B_z (red) [nT], b) Solar wind velocity v_x, c) Solar wind velocity v_y (black), v_z (red) [km/s], d) density [cc^{-3}], and e) temperature [°K]. Blue dashed line indicates Pi2 onset and blue solid line indicates substorm onset.

this event were investigated in depth by *Cao et al.* (2012). In this paper the authors discuss a double oval in the image data at 1720 UT with poleward boundary intensifications (PBIs) beginning at ∼1752 UT. They also point out auroral streamers in the IMAGE data between ∼1801 and ∼1820 UT, and argue that these signatures are indicative of earthward flows during the growth phase of the substorm. However, onset for this event in the IMAGE auroral observations is not clearly defined. There is a full auroral oval that formed during an earlier substorm at ∼1520 UT. The PBIs are most likely a result of the x-line retreat during the recovery phase of the substorms identified at 1704 UT in the SuperMag data set. Although there was auroral brightening seen at the time of the Pi2 onset at Urumqi (1820-1822 UT), poleward expansion did not begin until ∼1824-1825 UT as indicated above.

2.2 Simulation Results

In order to observe structures propagating along the plasma sheet, it is useful to remove the spatial affects caused by a curved or distorted plasma sheet in the simulation. For this study

we defined the center of the plasma sheet by using the position where B_x passes through zero. We compared this surface with that of maximum thermal pressure, which gives a good approximation for the central plasma sheet (CPS) on the night side (*Ashour-Abdalla et al.*, 2002), and found good agreement everywhere except $x > -7.5$ where the B_x surface organized the simulation results better. Figure 2.6 shows results from the simulation on the central plasma sheet before (panel a) and during (panel b) the substorm. The background colors are B_z, the purple arrows are the velocity vectors, and the black contours are the thermal pressure between 0 and 4000 pPa, dP=500 pPa. The reconnection regions, where B_z is zero, are colored in green. The TC1 location is indicated by the purple dot in the images. Two snapshots prior to the onset time of the substorm are shown in Panel a for times 1755 and 1805 UT. Both of these snapshots show that the neutral line is located between -20 and -25 R_E. They also show that there was a great deal of activity leading up to the substorm. This is especially evident at 1805 UT when fast plasma flows are present across the dusk sector in the region $15 < r < 20$ R_E, and the remnants of at least three fast flow channels, which appear as a dimple in the pressure contours, are present inside of ~ 15 R_E. Panel b shows four time steps at 10 minute intervals beginning at 1820 UT. The snapshot at 1820 UT shows a fast flow channel near midnight highlighted by the yellow box. This is the flow channel that agrees most closely, both spatially and temporally, with the TC1 observations. The reconnection at this time is very patchy in the region $-20 \geq x \geq -35$ R_E. The snapshot at 1830 UT shows that the reconnection and fast flows begin to move tailward. At ∼1840 UT there is one final flow channel that forms at the reconnection region located near -35 R_E and by 1850 UT the entire region inside of -30 R_E has quieted down.

2.3 Identifying Pi2 in the Simulation results

The first step to determine the relationship between the Pi2 pulsations and the DFs in the simulation is to identify the signatures of the two phenomena. By looking at the central plasma sheet in the simulation we are able to identify DFs which appear as propagating enhancements in B_z with $\delta B_z \geq 6nT$. Several DFs can be seen propagating earthward from

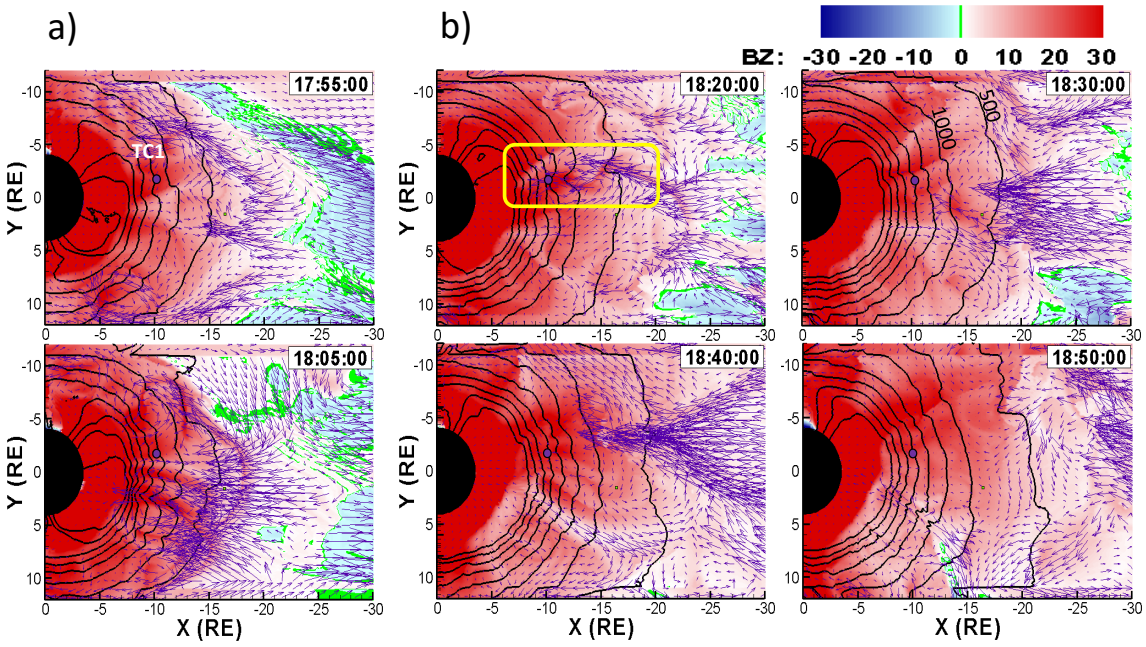

Figure 2.6: Simulation results in the central plasma sheet before (panel a) and during (panel b) the substorm. The background color shows B_z (-30 – 30 nT), the gray line contours show thermal pressure (0-4000 pPa, δP between contours is 500 pPa), the two outer pressure contours are labeled in the upper right panel for reference. The purple arrows show the velocity in the xy-plane. The purple dots indicate the location of TC1. The yellow box indicates an earthward propagating DF.

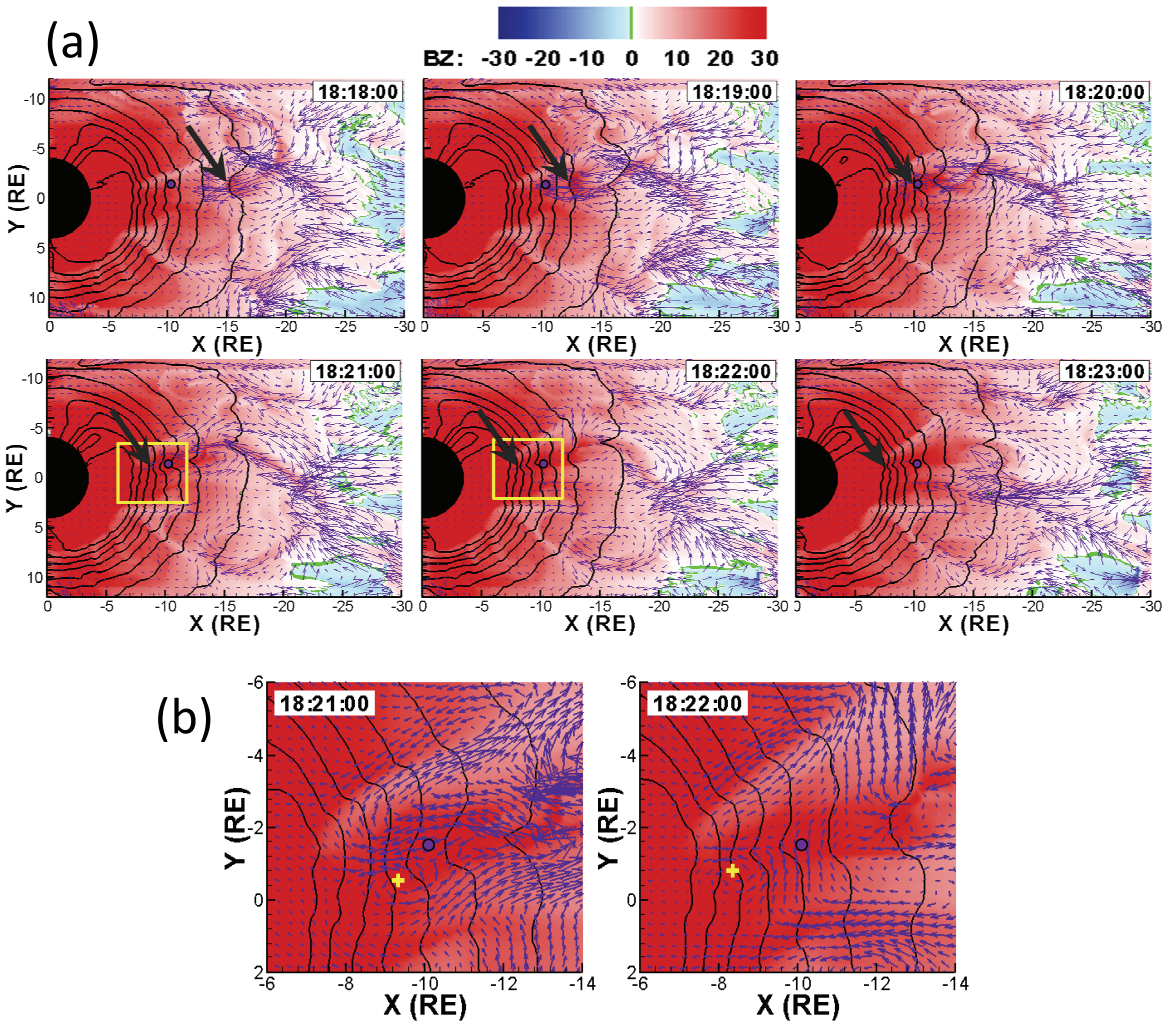

Figure 2.7: a) Simulation results on the maximum pressure surface at two minute intervals during the passage of a DF. The background color shows B_z (-30 – 30 nT), the gray line contours show thermal pressure (0-4000 pPa, δP between contours is 500 pPa), and the purple arrows show the velocity in the xy-plane. The DF is indicated by the large blue arrow in each panel. The purple dot indicates the location of TC1. b) The regions in the yellow boxes in the panels for 1821 and 1822 UT are expanded to show the flow vortex at the leading edge of the DF. Yellow crosses indicate the center of the vortex.

the reconnecting regions in the simulation after 1700 UT with the majority being confined within a few hours of local midnight. The DFs with the largest δB_z occur between 2330 and 0115 MLT. Figure 2.7a shows simulation results on the maximum pressure surface between 1818 and 1823 UT. The format is the same as Figure 2.6. The DF shown in these images is coincident with the TC1 observations and is confined to the region 0015-0115 MLT. The large black arrows indicate the leading edge of the DF as it propagates earthward. Figure 2.7b shows the regions outlined by the yellow boxes at 1821 and 1822 UT. From these two images one can see the obvious flow reversal on either side of the DF as well as a flow vortex that forms at the earthward edge of the structure (*El-Alaoui*, 2001; *Ashour-Abdalla et al.*, 2002; *Walker et al.*, 2006; *El-Alaoui et al.*, 2009; *Ashour-Abdalla et al.*, 2009; *El-Alaoui et al.*, 2010; *Ge et al.*, 2011; *Birn et al.*, 2011). The center of the vortex, indicated by the yellow crosses, travels earthward $\sim$1 R_E in the minute between the two time steps. Throughout the simulation interval, there are several BBFs that propagate with their associated DFs from reconnection regions between -12 and -35 R_E. Each individual flow channel extends over many earth radii in x but extends across only 1-3 R_E in y in GSM coordinates.

The signatures associated with the DFs in the simulations are identified by averaging the simulated velocity, magnetic field, and pressure at fixed radial distances from 3 to 50 R_E across a region of magnetic local time (MLT) where the dipolarization fronts are present. This allows us to see the effects that the DFs in a given local time range have on the inner magnetosphere as they travel earthward while averaging out the smaller scale spatial fluctuations within the DFs themselves. Next we take 10 minute running averages and subtract them from the measured values to look only at the perturbations in the different components.

As was stated before, most of the strongest DFs in the simulation are observed in the region 2330-0115 MLT, however, the strong DF observed at onset is located in the region 0015-0115 MLT. Figure 2.8a and b show the central plasma sheet at 1820 UT in the same format as the panels in Figure 2.6. The gray lines in panel a indicate the MLT wedge between 2330 and 0115 MLT, and the black lines in panel b indicate the MLT wedge between 0015 and 0115 MLT. Figure 2.8c shows the perturbations on the central plasma sheet in the average

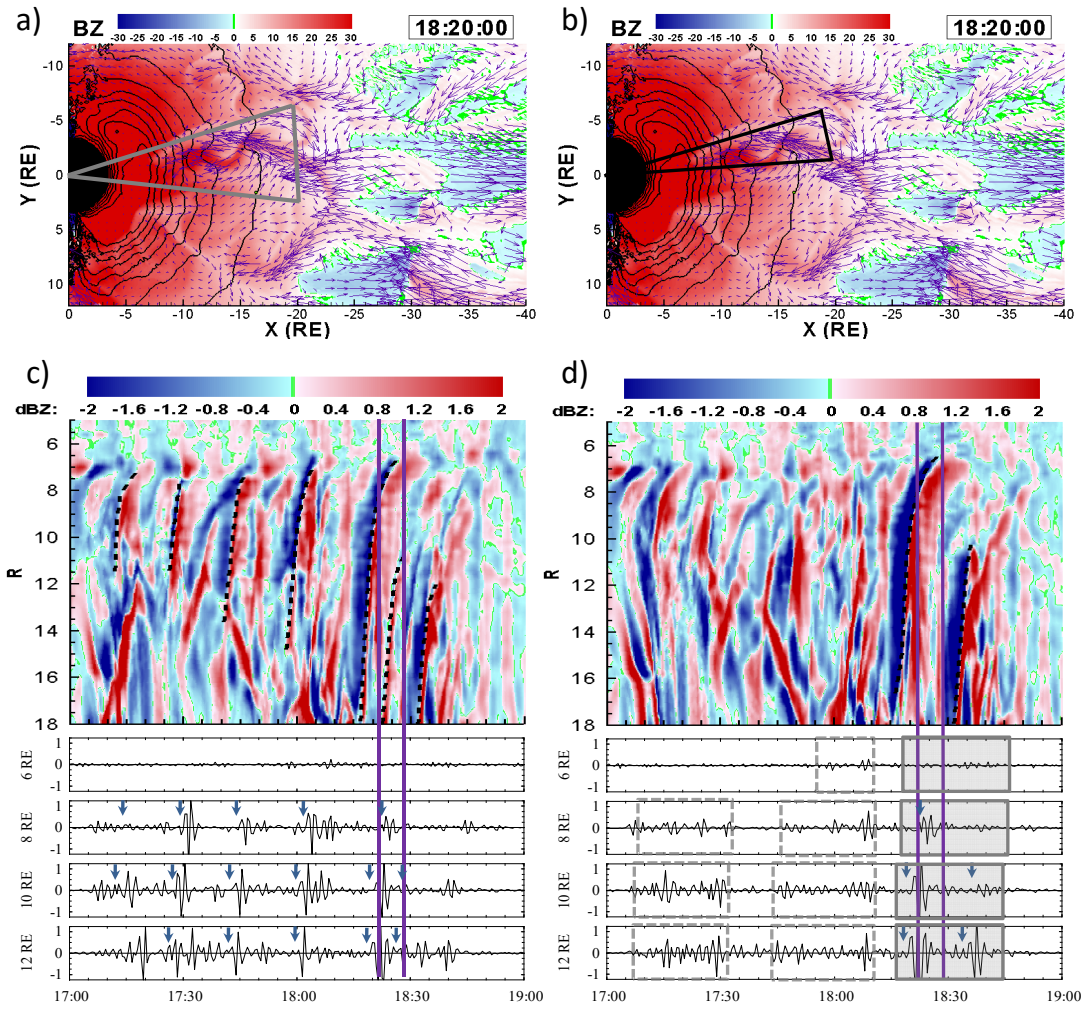

Figure 2.8: a) An image of the simulated CPS at 1820 UT in the same format as Figure 2.6 with the region 2330-0115 MLT indicated by the gray lines. b) Same as panel a but with the region 0015-0115 MLT indicated by the black lines. c) Perturbed variables in B_z on the CPS averaged over the region 2330-0115 MLT plotted versus time in x and radial distance from earth in y. The dashed lines identify the paths of strong DFs. The lower panels show line plots of the perturbed variables at r = 6, 8, 10, and 12 R_E. Vertical lines indicate Pi2 and substorm onset. Blue arrows identify the passage of strong DFs. d) Same as panel c for the region 0015-0115 MLT. Gray highlighted intervals are times when the frequencies of the oscillations related to the DF at onset are within the Pi2 range. Dashed boxes indicate Pi2 fluctuations related to DFs outside the selected local time region.

of B_z between 2330 and 0115 MLT, and Figure 2.8d shows the perturbations in B_z between 0015 and 0115 MLT, plotted versus time and radial distance from Earth in R_E. When you look at a given radial distance at a DF you first observe a decrease in B_z followed by a sharp increase. The earthward propagating DFs in Figure 2.8c can be seen in B_z (Figure 2.8c-d) as sharp boundaries between negative (blue) and positive (red) contours. The paths of the strongest, most coherent DFs identified in panels c and d have been traced (black dashed lines). The slope of the dashed lines indicates how fast the DFs are propagating. The line plots at the bottom of panels c and d show δB_z at r = -6, -8, -10, and -12 R_E filtered to Pi2 frequencies by using a band pass filter. The blue arrows on the line plots indicate the times when DFs were observed at the given radial distance in the tail. The solid purple lines indicate Pi2 onset at Urumqi (1822 UT) and substorm onset identified in AL (1828 UT). Gray highlighted intervals in panel d are times when Pi2 frequency oscillations are found at and immediately after the dipolarization front observed at onset. In Figure 2.8d, there are bursts of fluctuations within the Pi2 range following each of the DF observed at onset (highlighted in gray). Additional Pi2 period perturbations prior to onset and related to DFs outside of the MLT region selected are indicated by dashed boxes.

To show that the fluctuations in are, in fact, Pi2 period fluctuations rather than simply a portion of a broadband disturbance we calculate the power spectral density for the time series in Figure 2.8d. Figure 2.9 shows the power spectral density for the average B_z at a) 8 and, b) 10 R_E, in the 0015-0115 MLT bin. The analysis was carried out on a 15 minute interval centered on 1824 UT sampled every 30 seconds. The power spectral density is calculated by using the Welch method. The time series is divided into 10 minute intervals that overlap by 7.5 minutes. A periodogram is computed for each time series using a discrete Fourier transform and taking the squared magnitude of the result. The resulting power spectral density for the 15 minute interval is the average of the resulting periodograms. There is a peak in both panels within the Pi2 frequency range, shown by the shaded regions in the figure.

In order to focus on the perturbations related to the DF observed by TC1 at onset we focus on the region between 0015 and 0115 MLT. In addition, since TC1 was near the edge

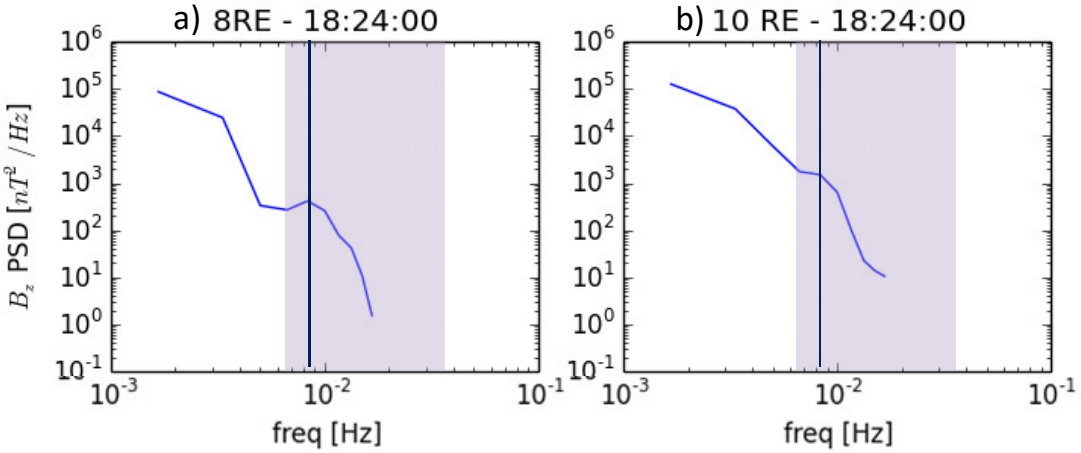

Figure 2.9: PSD $[nT^2/Hz]$ for the average B_z at a) 8 R_E and b) 10 R_E in the 0015-0115 MLT bin. The shaded region indicates the Pi2 frequency range and the black line indicates the frequency where there is a peak in the PSD.

of the plasma sheet during the time leading up to onset we focus on the surface 1.5 R_E above the minimum B_x plane. Figure 2.10a shows the perturbations in the radial component of the magnetic field on a plane 1.5 R_E above the minimum B_x plane. The patchy appearance near the top of the plot is a numerical effect of the resampling process after the plasma sheet is extracted from the simulation results. Ground-based observations, low pass filtered and resampled at 30 second time-steps to match the simulation results, are shown at the bottom of the figure for comparison. The black dashed lines have been copied from Figure 2.8d to show how the perturbations relate to the path of the DFs. Pi2 fluctuations are observed at -6 R_E, highlighted in gray in the line plots, as the DF at onset approaches and begins to disrupt the braking region. The onset of these perturbations is at 1819 UT, a few minutes before Pi2 onset on the ground, and the fluctuations continue for about 30 minutes which agrees well with the duration of Pi2 in the Urumqi observations. Fluctuations are also evident in the radial component of the magnetic field at -6 R_E, during the SMC-like interval, that are related to DFs just outside the selected MLT range (gray dashed boxes in Figure 2.10a). The B_R component is interesting because it shows the fluctuations that are propagating across the magnetic field lines. These are the fluctuations that would be observed at mid- to low latitudes.

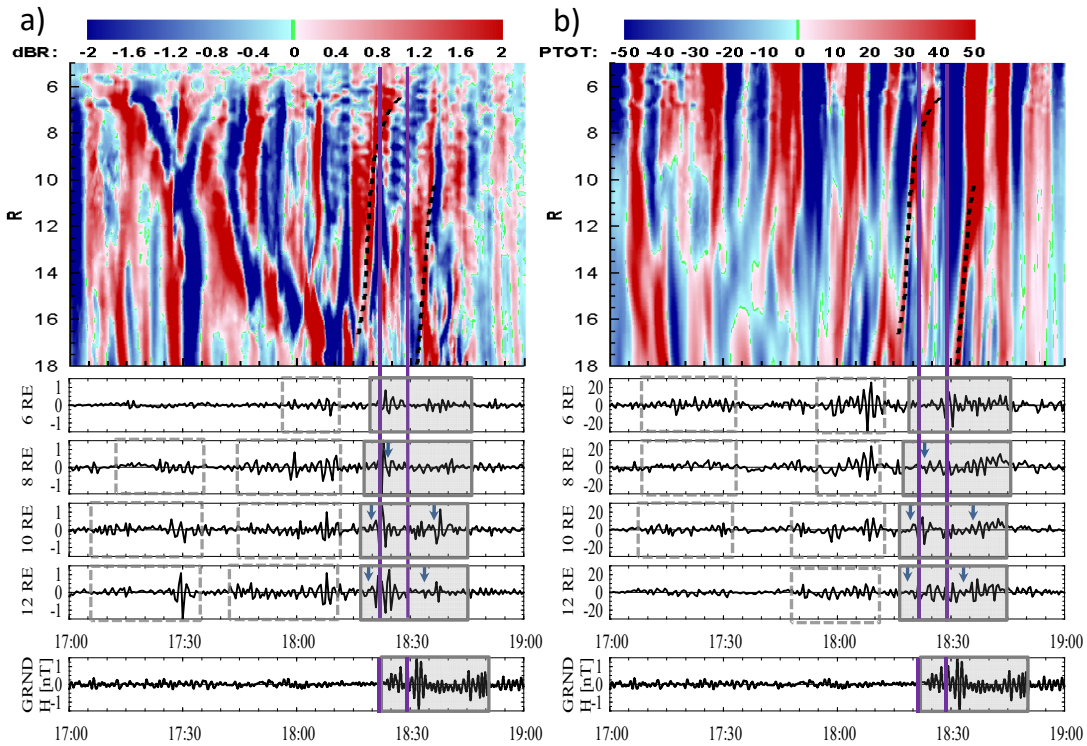

Figure 2.10: Perturbed variables a) δB_R, b) the perturbed total pressure δP_{total} plotted in the same format as Figure 2.8d. Ground magnetometer observations filtered to 30 second resolution have been included at the bottom of the figure for comparison.

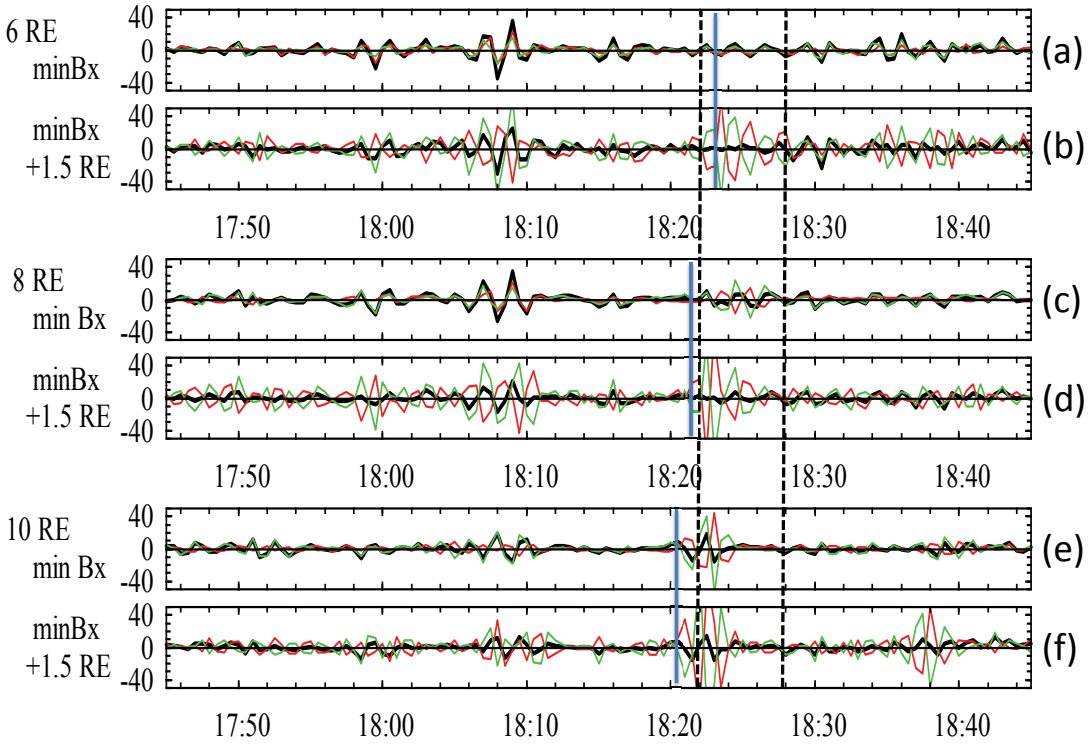

Figure 2.11: Perturbations in the thermal pressure (green), magnetic pressure (red), and total pressure (black)[pPa] at -6, -8 and -10 R_E between 0015 and 0115 MLT. For each radial distance, perturbations are shown on the minimum B_x surface, and 1.5 R_E above the minimum B_x surface. Blue vertical lines indicate the times the DFs were observed at the given radial distances and the black dashed lines indicate Pi2 and substorm onset.

Figure 2.10b shows that the fluctuations in δP_{total} (thermal pressure plus magnetic pressure) on a plane 1.5 R_E above the minimum B_x plane are also coincident with the passage of DFs through the region. Following the DF at onset there are fluctuations in the line plots from -12 to -6 R_E with a period of ∼120-150 s (highlighted in gray).

Figure 2.11 shows line plots of the perturbations in the magnetic pressure (red), thermal pressure (green), and total pressure (black) at the minimum B_x plane and 1.5 R_E above the plane at -6 (a-b), -8 (c-d) and -10 (e-f) R_E in the magnetotail from 1745 to 1845 UT. The blue vertical lines indicate the time the DF reached the given radial distance and the black dashed lines indicate Pi2 and substorm onset. In general, the fluctuations in the magnetic and total pressures 1.5 R_E above minimum B_x surface, near the edge of the plasma sheet, are out of phase. On the minimum B_x surface fluctuations are more often in phase suggesting a fast mode wave. The perturbations at the time of the DF crossing are typically in anti-phase suggesting a slow mode wave. The exception is at -6 R_E on the minimum B_x surface where the perturbations are in phase at the time of the DF. In the center of the plasma sheet at -10 R_E (panel e) the total and magnetic pressures are only in phase for a short time beginning at 1821 UT, just before Pi2 onset. Near the edge of the plasma sheet at -10 R_E (panel f) the fluctuations in the magnetic pressure in panel d very closely resemble the Pi2 observed by TC1 beginning at 1822 UT (see Figure 2.4a).

Figure 2.12 shows the perturbations in a) the velocity parallel to the magnetic field (δv_{pa}), and b) the velocity in the earthward direction (δv_x) 1.5 R_E above the plasma sheet plotted in the same format as Figure 2.8. The amplitude of the fluctuations observed in δv_{pa} (panel a) generally increase following the passage of a DF, and perturbations are observed in to -6 R_E following the DF at onset. Pi2 period fluctuations related to DFs outside the selected MLT region are observed at 1705-1730 UT and 1745-1810 UT (gray dashed boxes). The first of these intervals is associated with a strong minimum in B_z at the beginning of the disturbed period in the simulation. The second interval occurs just before the first minimum in the AL index discussed above. The interval related to the DF at onset (highlighted in gray) occurs just before and during the expansion phase of the substorm, and may represent the precursor to the Pi2 observed on the ground at Urumqi. The enhancement in δv_{pa} tailward

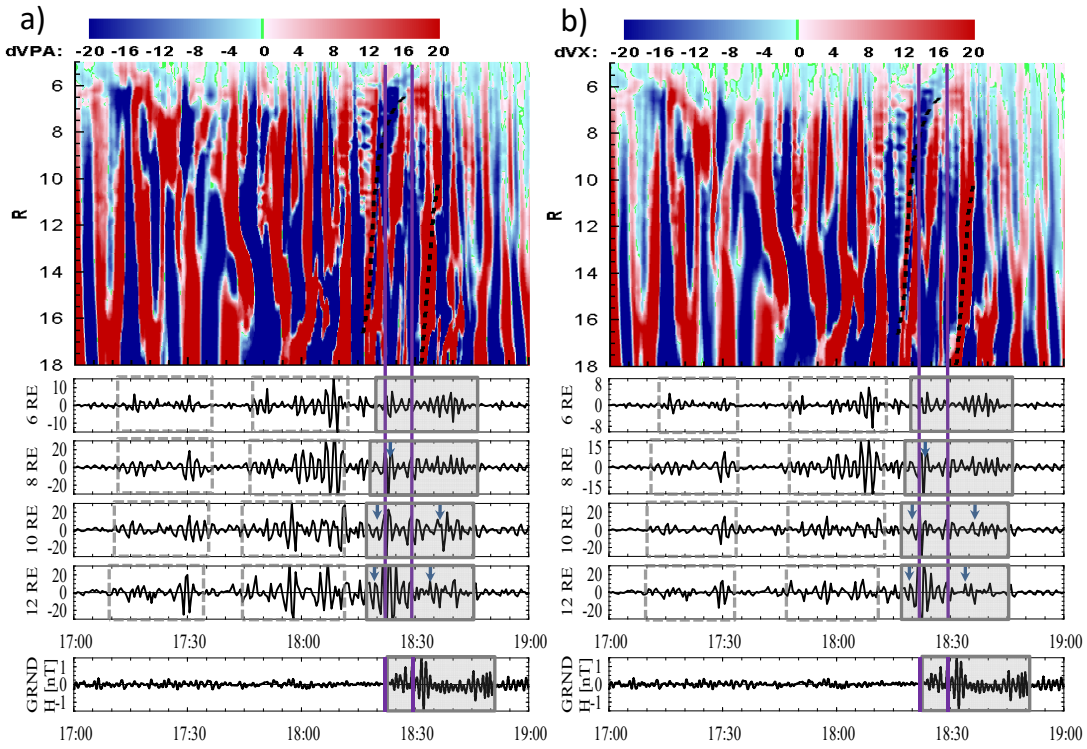

Figure 2.12: Perturbed variables a) $\delta v_{\parallel}$, b) δv_x plotted in the same format as Figure 2.10.

of the braking region, along the path of the DF within the Pi2 range may be associated with Transient Response (TR) Pi2 as described in Section 1.4.2.

The amplitude of the fluctuations in δv_x (Figure 2.12b) increase slightly before the DFs passage through the region. However, we must remember that the fluctuations are over a range in MLT from 0015 to 0115 UT. Because the flow channels are so narrow (1-2 R_E)(see Figure 2.7), Figure 2.12a shows the effects of the interaction between several earthward flow channels and rebound flows, the tailward flows that form in the vortices to either side of each fast flow channel, located outside of the MLT region. Fluctuations in δv_x are well correlated with fluctuations in δB_R. The line plots at the bottom of panel b show that the amplitude of the fluctuations in δv_x decreases by more than 50% as the disturbances move earthward from -12 to -8 R_E. The fluctuations in δv_x associated with the DF at onset agree very well with the duration of the Pi2 observed on the ground and the fluctuations earlier in the simulation agree well with the timing of the first drop and the first minimum in the AL index (Figure 2.2). However, the earlier flow channels do not penetrate as far earthward as

the flow channel observed at substorm onset. As a result the perturbations associated with the earlier flow channels would not have been observed at mid to low latitudes. Because fluctuations are observed in the AL index in agreement with the timing for the early flow channels, it is likely that they generated perturbations at higher latitudes.

2.4 The Relationship between Fast Flows, Dipolarization Fronts, and Pi2 Period Pulsations in the Magnetotail

Previous studies have used satellite measurements to investigate the origin of Pi2 pulsations and build models to describe how they are generated. The benefits of using a global MHD simulation to investigate the relationship between the DFs and the Pi2 pulsations is that we can examine the entire region where the bursty flows, DFs and Pi2 pulsations are present rather than using data from single points in space. This allows us to identify possible source regions and to track the evolution of the pulsations as they move through the simulation.

In order to investigate the azimuthal extent of the fluctuations near the inner edge of the plasmasheet, we have taken several MLT bins and examined the coherence between them by looking at how the period and phase of the pulsations change with location. Figure 2.13 shows the perturbations in the total magnetic field (B_T) in 15 minute MLT bins between 2330 and 0145 MLT on the surface 1.5 R_E above the center of the plasma sheet for the interval 1730-1900 UT. From top to bottom, the panels show the MLT bins a) 2330-2345, b) 2345-0000, c) 0000-0015, d) 0015-0030, e) 0030-0045, f) 0045-0100, g) 0100-0115, h) 0115-0130, and i) 0130-0145 MLT. The values for coherence between the bin 0030-0045 MLT and the other MLT bins for the shaded intervals (1805-1813 UT and 1819-1829 UT) range from 0.6 to 0.85 for the low end of the Pi2 spectrum (6-11 mHz). By investigating the azimuthal extent of the pulsations observed at -6 R_E we can determine whether they might be responsible for generating the pulsations observed on the ground. In general, the magnetic field perturbations during the shaded intervals on this surface show good coherence over ∼1.5 to 2 hours MLT. This is consistent with a recent study by *Kwon et al.* (2012) which shows high coherence if the signals (multiple satellites and ground-based observations) are within

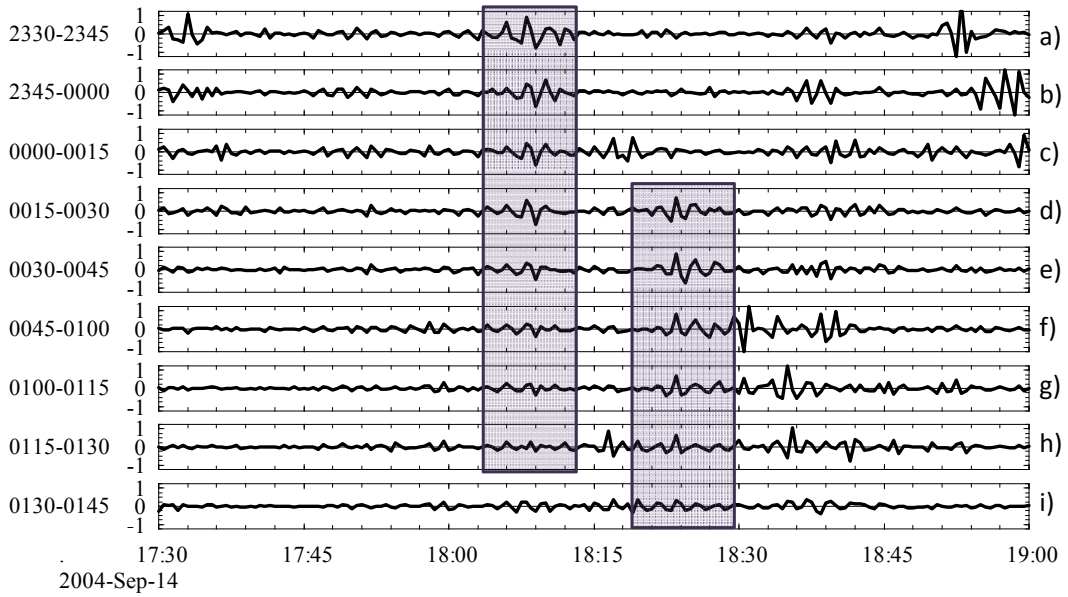

Figure 2.13: Perturbations in B_T at -6 R_E 1.5 R_E above the plasma sheet in the MLT bins a) 2330-2345, b) 2345-0000, c) 0000-0015, d) 0015-0030, e) 0030-0045, f) 0045-0100, g) 0100-0115, h) 0115-0130, and i) 0130-0145 MLT. The shading indicates MLT bins which have good coherence to the bin at 0030-0045 MLT in the perturbations related to the DFs observed during the first minimum in AL (1085-1813 UT) and at onset (1819-1929 UT).

3 hours MLT of each other. However, although we see coherence across several MLT bins above the center of the plasma sheet during the expansion phase of the substorm (1819-1829 UT), and the wave forms at -6 R_E in the simulated magnetic pressure look very much like the observations, we only see coherence across $\sim$1 hour of MLT near the center of the plasma sheet. Therefore, it is difficult to determine a direct causal relationship between the pulsations we observe in the simulation and the mid-latitude observations from the Urumqi magnetometer, since higher latitude Pi2 observations are unavailable for this event. We can, however, use the ground observations for a timing comparison with the simulation.

In order to investigate the frequency of the perturbations versus radial distance, we have run a power spectral density analysis on the average B_z at radial distances of 8, 10, 12, and 14 R_E in the 0015-0115 MLT bin. The analysis was carried out on 15 minute intervals centered on the time of the DF crossing at each radial distance. The power spectral density is calculated in the same manner as the PSD shown in Figure 2.9. The results are shown in Figure 2.14. The times mark the center of the 15 minute time series selected. The shaded

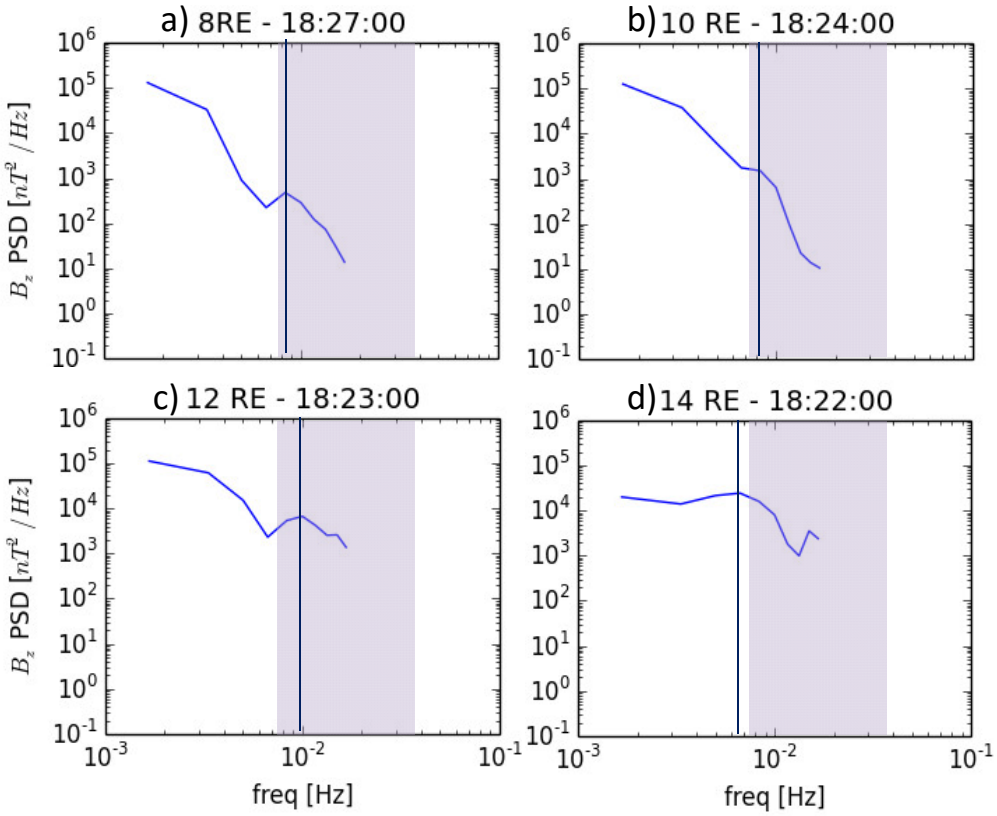

Figure 2.14: PSD in B_z at the time of the DF crossing at a) 8 R_E (1827 UT), b) 10 R_E (1824 UT), c) 12 R_E (1823 UT), and d) 14 R_E (1822 UT). The shading indicates the Pi2 frequency range. The black vertical line marks the frequency where there is a peak in PSD.

region shows the Pi2 frequency range and the black vertical line marks the frequency where there is a peak in PSD. At 8, 10, and 12 R_E the peak in PSD falls within the Pi2 range. However, at 14 R_E the peak is at a lower frequency and more spread out than it is at smaller radial distances. The fact that the perturbations are lower at 14 R_E than at the smaller radial distances agrees well with the transient response model for Pi2, however, the frequency of the fluctuations is highest at 12 R_E than at 8 and 10 R_E. This may be a result of the meandering motion of the flow channel in the area between ∼10 and 14 R_E.

Based on Figures 2.8, 2.10 and 2.12 the simulation observed Pi2 period pulsations at -6 R_E related to the DFs outside the selected region. This is in contrast to the observations which only show Pi2 pulsations after 1823 UT. There is a short (∼10 min) burst of weak Pi2 pulsations just after 1730 UT in the observations that may be related to the earlier DFs

observed in the simulation and the first drop in AL, but there is nothing in the observations that could correspond to the fluctuations between 1755 and 1805 UT in the simulation. One reason for the discrepancy may be that the DFs were in the wrong local time for the Pi2 to be observed by the Urumqi station. Although the Pi2 pulsations spread out at mid-latitudes, as noted above, satellite and ground observations are only found to be coherent when the pulsations are observed by a satellite that is less than 3 hours removed from the ground station in MLT. This may be especially true for the DF burst at 1755-1805 UT which was predominantly on the dusk side while Urumqi was on the dawn side at ∼0200 MLT. Another possibility is that the fluctuations observed at -6 R_E in the simulation prior to onset are not able to propagate earthward to be observed at lower latitudes. Due to the lack of an inner magnetosphere/plasmasphere model in the MHD simulation we are not able to investigate the propagation of Pi2 to lower latitudes and we leave this topic for future research.

Focusing on the perturbations at substorm onset, Figure 2.10b shows that perturbations with Pi2 periods are present in the δP_{total} from -6 to -12 R_E between ∼1815 and 1845 UT, when the burst of DFs was observed near the time of onset. During this interval the simulation shows at least 6 individual DFs of varied intensities which form and travel earthward within a time span of ∼30 minutes at locations between ∼2230 and 0130 MLT. The pressure fluctuations may be initiated by the passage of the strong DF and then amplified by the succeeding DFs. The fluctuations in pressure can also be identified in Figure 2.7 as the perturbations in the thermal pressure contours (gray contours) surrounding the flow channel as the DF travels earthward. There is also a tailward displacement of the pressure contours associated with the tailward flows on either side of the flow channel. Each time a new DF enters the region a new indentation in the pressure contours forms and migrates toward either flank. During active periods in the simulation several of these indentations can be observed on each of the pressure contours. The perturbations in the pressure near the center of the plasma sheet (see Figure 2.11 a,c,e) following the arrival of the DFs may be related to the fast mode wave which propagates into the inner magnetosphere to generate low to mid-latitude Pi2. We also observe earthward velocity perturbations all the way in to -6 R_E (Figure 2.12b) that are related to the fluctuations in the pressure which agrees well

with the directly driven category of Pi2 *Kepko et al.* (2001).

Each time a bursty flow and its associated DF travel earthward in the simulation, the flows at the earthward edge of the DF are diverted to either side of the flow channel. As the flows are diverted they interact with the background flows and neighboring flow channels which cause further diversion. In many cases the flows eventually turn tailward. The tailward flows then interact with subsequent earthward flows to create flow perturbations and vortices. The resulting vortices can be seen in the velocity vectors in Figure 2.7b. As the DFs reach the inner magnetosphere we begin to see tailward flows to either side of the initial earthward flow channel. The interactions become more pronounced during the intervals of intense activity due to the fact that there are several DFs which travel earthward in a short amount of time during this period. Velocity fluctuations intensify each time a new DF passes through the region (highlighted in gray) indicating that the DFs may act to enhance the existing perturbations bringing them above the ambient noise levels in the region (see Figure 2.12). There are also velocity perturbations associated with DFs outside the selected MLT region (gray dashed boxes in Figure 2.12) which result from the interactions between the various flow channels. As discussed in the previous section, each of the intervals corresponds to a period when there are large fluctuations in the AL index (see Figure 2.2). In addition there are field aligned currents generated by the flow channel as it travels earthward. A plot of the field aligned currents, in the same format as Figure 2.10, is shown in Figure 2.15. From this plot it is clear that the perturbations in the field aligned currents begin just before the arrival of the flow channel. The fluctuations are associated with the vortices that form on either side of the flow channel as it travels earthward and would transmit the perturbations generated by the flow channel into the high-latitude ionosphere.

In Figure 2.8c there is a steady boundary in the field at -7.5 R_E, where the DFs are stopped at the inner edge of the plasma sheet, until 1805 UT when a relatively strong DF enters the region and distorts the boundary, pushing it earthward $\sim$0.5 R_E. Before the magnetic field has time to recover, another strong DF penetrates to $\sim$-6.5 R_E at 1823 UT, and displacing the boundary further in the earthward direction. It is only after the DFs displace the boundary at the inner edge of the plasma sheet that we have Pi2 period

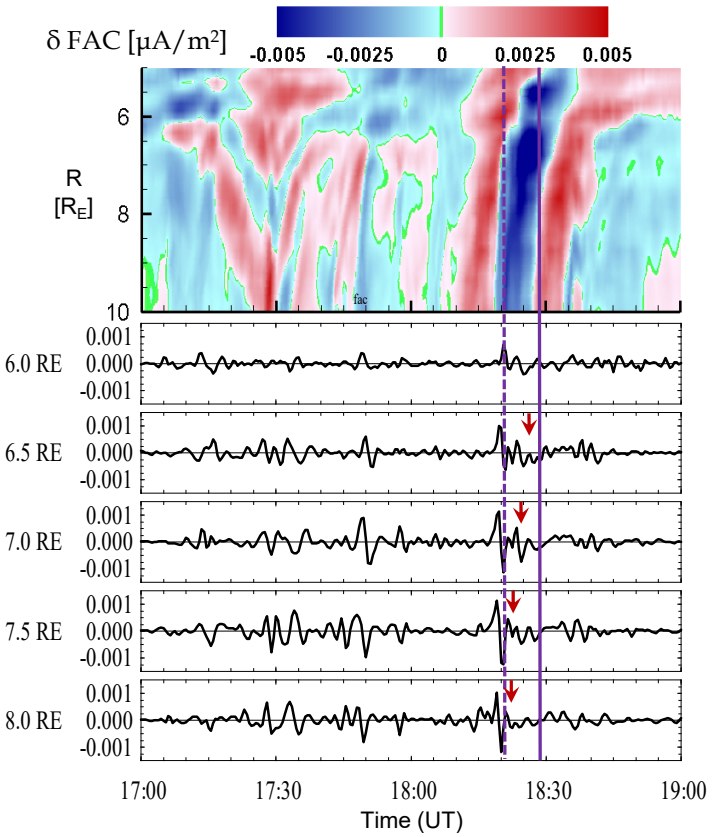

Figure 2.15: Perturbations in the field aligned currents (δFAC [$\mu A/m^2$]) plotted in the same format as Figure 2.10.

fluctuations in δB_z inside -7 R_E. The timing and duration of the interval when Pi2 period perturbations in δB_z are observed inside -7 R_E (1830-1845 UT), associated with the DF at 1815-1824 UT in the simulation, agrees well with expansion phase of the substorm and with the duration of the second packet of Pi2 (1840-1855 UT) in the ground-based observations. In addition, the perturbations in v_{pa} associated with the DFs at 1830 to 1855 UT are observed at -6 R_E and may be related to the inertial current Pi2s described by *Kepko et al.* (2001). IC Pi2 appear to be generated by the vortices formed through interactions between the flows and rebound flows associated with the successive DFs as they enter the near-Earth region. However, the velocity perturbations are quickly damped earthward of $\sim$-7 R_E except during the intervals when a strong DF has disrupted the steep pressure and magnetic field gradients in the braking region.

2.5 Conclusions and Summary

In order to better understand generation of Pi2 and how they are associated with substorm dynamics, we need a global view of the magnetosphere. We have investigated the generation of Pi2 waves in the tail by DFs propagating earthward from a near-Earth neutral line by analyzing a global MHD simulation of a substorm event on September 14, 2004. We note that this is the first time a global MHD simulation has been used to analyze Pi2 pulsations in the magnetotail. Because global MHD simulations provide estimates of the critical parameters throughout the inner magnetosphere, they are valuable tools for studying such processes as the generation of Pi2 and determining how they link to earthward propagating dipolarization fronts. The sequence of events in the simulations is similar to that inferred from observations by the Double Star, and IMAGE spacecraft, and the variations of the AL index, indicating that the simulation has done a reasonable job of reproducing the state of the magnetotail for this event. The substorm begins at $\sim$1828 UT and is preceded by an interval of enhanced but variable convection. Both the initial period and the substorm have multiple DFs which lead to vorticity. The DFs observed in the simulation are very localized with an azimuthal extent on the order of 1-2 R_E. Several dipolarization fronts have been identified in the

simulation and are linked to Pi2 frequency fluctuations in the magnetic field, velocity and pressure inside -13 R_E, but not all of the flows make it into the inner magnetosphere to generate the Pi2 observed inside the braking region.

Considering the Pi2 period fluctuations outside the braking region, there is good agreement between observations by TC1 and fluctuations in the simulation at a location similar to that of TC1. We cannot draw a direct relationship between the Urumqi observations and the pulsations inside the braking region in the simulation since the pulsations near the plasma sheet are only coherent over about 1 hour of MLT. However, we have shown good agreement in the relative timing of the Pi2 pulsations when comparing the observations and the simulation. The timing and location of dipolarization fronts and Pi2 pulsations in the simulation lead us to believe that the Pi2 waves are generated by the DFs in agreement with several models developed to explain observations *Kepko et al.* (2001, 2004).

Our main conclusions for this project can be summarized as follows: 1) Dipolarization fronts create perturbations in B_z which have periods in the Pi2 range, but the perturbations quickly damp unless there are subsequent DFs to keep the oscillations going. 2) There are Pi2 period perturbations in the total pressure, and B_R at $\sim$-6– -12 R_E following the DFs observed at onset. The Pi2 period pulsations in both total pressure and B_R at -6 R_E beginning shortly before Pi2 onset in the observations agree well with ground-based observations. 3) Pulsations with periods within the Pi2 range are observed in the velocity components inside $\sim$-13 R_E throughout the simulation, and are enhanced directly following the passage of each flow burst observed when we look at the region 0015-0115 MLT. It appears that the compression and rebound of the BBFs and their associated DFs as they approach the braking region produce the Pi2 signatures in agreement with *Kepko et al.* (2001). 4) The DFs in the simulation between 1715 and 1820 UT all stop tailward of -7.5 R_E without causing serious disruption to the braking region, and the magnetic field perturbations associated with them are quickly damped. The fluctuations inside the braking region appear to be driven by perturbations in total pressure, B_R, v_{pa} and v_x associated with the BBFs even though the B_z signatures dissipate tailward of the braking region.

This project has raised the question of the impact of the braking region on Pi2 generation.

Figure 2.11 shows a slow mode signature convecting with the DF but there appears to be a phase shift as the perturbations pass through the braking region. We also see a change in the amplitude of the perturbations as they move earthward from the tail into the braking region. The phase shift and change in amplitude of the perturbations will be addressed in the next section.

CHAPTER 3

Comparing Pi2 Results from the UCLA and LFM Models

Using the same event that was described in Chapter 2 we compare results from the UCLA 3D global MHD model described in Section 1.5.1.1, and the Lyon-Fedder-Mobarry (LFM) global MHD model described in Section 1.5.1.2. The purpose of using the second model is to test the robustness of the results for Pi2 generation and propagation.

3.1 Magnetospheric Results

Cross-field flows are fastest near the center of the plasma sheet. In order to identify the perturbations associated with the fast flows, we must first determine the location of the plasma sheet in the simulation results. We identify the plasma sheet by selecting the surface of minimum $|B_x|$ in GSM coordinates. Since the UCLA model is set up on a Cartesian grid we simply select the z location for each (x, y) pair that has the minimum $|B_x|$ value in the region $|z| < 8\ R_E$. Due to the nature of the grid in the LFM model we cannot use the same technique to identify the plasma sheet as was used for the UCLA model. Instead, we select the grid points that have $|B_x| < 2.5$ nT and $4 > z > -8\ R_E$. The selected points are then projected onto a plane and linear interpolation is used to plot them on a regular grid with a grid spacing of 0.2 R_E in both the x and y directions. The average z value is found for each point on the grid to determine the location of the plasma sheet. In the simulation results the plasma sheet is displaced from the geomagnetic equator by several R_E at distances greater than 15 R_E down tail. The large span in z included in the selection criterion accounts for that displacement and allows for identification of the plasma sheet as far tailward as -40 R_E.

We find that, in both simulations, the plasma sheet is located between $z = 2$ and $z = 0$ R_E in the region $-12 \leq x \leq 0$ R_E then begins to tilt in the -z direction so it is located at $z \approx -7$ R_E at $x = -30$ R_E.

Snapshots of the plasma properties at the location of the plasma sheet from the simulations are shown in Figure 3.1. The top panels show results from the UCLA model, and the bottom panels show results from the LFM model, every minute between 1821 and 1826 UT. The background color shows B_z between 50 and -50 nT. The green color marks $-0.15 \leq B_z \leq 0.15$ nT to show approximate locations for the reconnection regions in the plasma sheet. Black arrows show the velocity in the plane and gray contours show thermal pressure. In most cases there is a stagnation point in the flows at or near the green regions where $B_z = 0$ supporting the assumption that reconnection is occurring in those regions. Black arrows show the velocity in the plane with a reference vector given for 500 km/s, and gray contours show thermal pressure for 0-4000 pPa ($\delta P = 500pPa$). The dark green x marks the TC1 location and the panels show that the respective DFs observed in the simulations cross directly over the TC1 location.

There are several similarities in the global configurations in the two simulations. Through most of the substorm interval, the reconnecting regions (green in Figure 3.1) in both simulations are located between -20 and -25 R_E. Reconnection in the UCLA results is more patchy than in LFM, probably because the current-dependent anomalous resistivity in the UCLA model allows for reconnection in more localized regions. Most of the fast flows from the reconnection regions in both models are slowed and diverted before reaching -12 R_E. As a result of this diversion, the flow channels that penetrate further earthward are pinched into azimuthally thin structures, in agreement with observations of narrow channels of fast plasma flows in the tail (e.g., *Baumjohann et al.*, 1989; *Angelopoulos et al.*, 1994). The diversion itself is due to vorticity from earlier flow channels and the formation of a secondary minimum in B_z 2-5 R_E earthward of the reconnecting regions. The vorticity observed in the simulation results is similar to that presented in previous MHD studies of flow channels (e.g., *El-Alaoui et al.*, 2009; *Birn et al.*, 2011; *El-Alaoui et al.*, 2013). An example of the secondary minimum in B_z can be found in the 1821 UT snapshots in Figure 3.1 at the locations marked

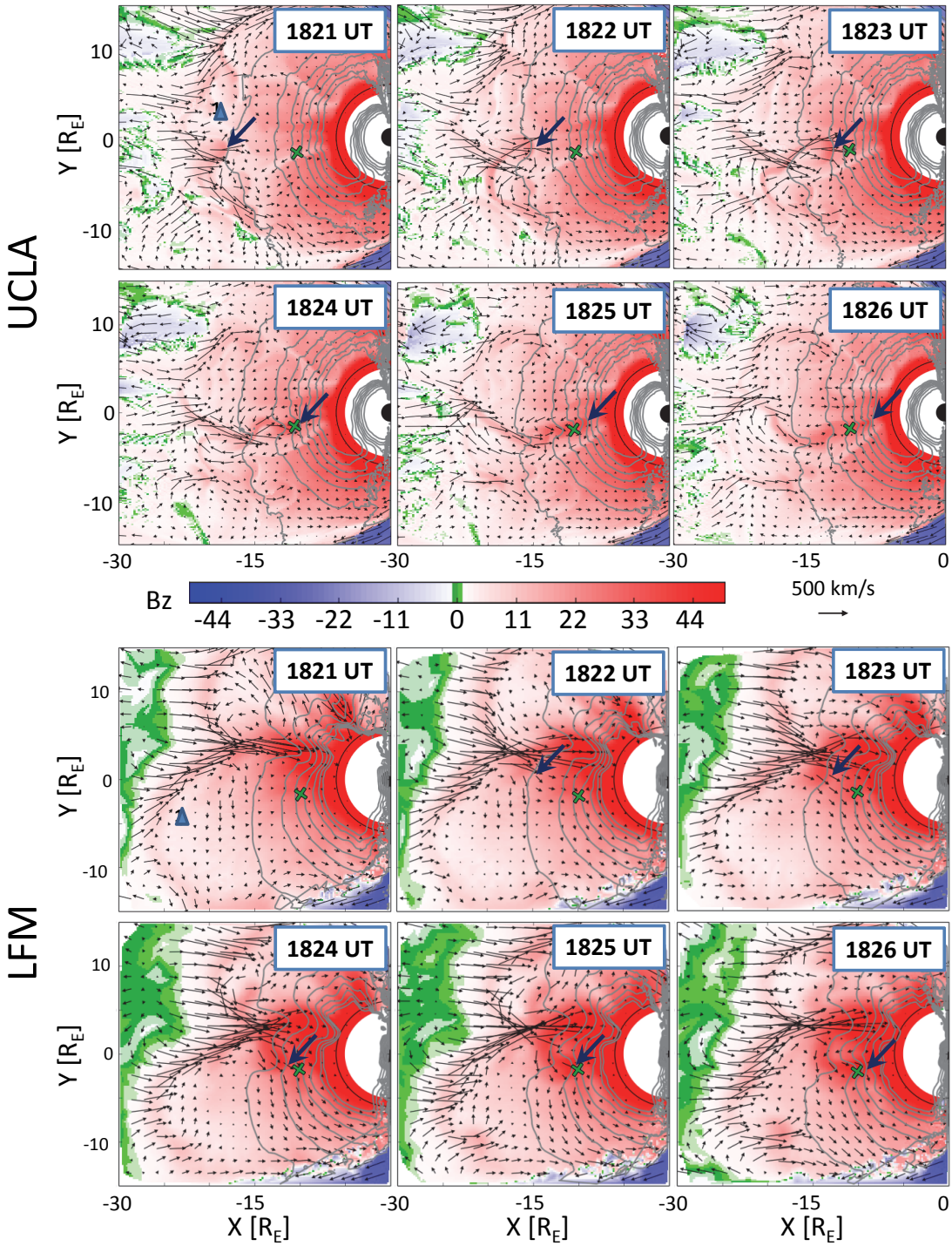
UCLA
LFM
1821 UT
1822 UT
1823 UT
1824 UT
1825 UT
1826 UT
Y [R_E]
X [R_E]
10
0
-10
-30
-15
0
Bz
-44 -33 -22 -11 0 11 22 33 44
500 km/s

by the light blue triangles.

The flow channel in the UCLA results that agrees in timing and location with the appearance of dipolarization at the TC1 spacecraft is fairly isolated and forms near midnight (0045 MLT). There are other DFs that form around the same time as the DF that agrees with the TC1 observations, but they are located at different local times so they would not have been observed by TC1. The flow channel in the LFM results is also located very close to midnight between 0045 and 0100 MLT, but there is also a very strong flow channel that forms earlier, just after 1800 UT, and persists for over 20 minutes just to the dusk side of midnight between 2300 MLT and midnight. Thus, the LFM flow channel that agrees with the TC1 observations is not as isolated, spatially or temporally, as is the corresponding flow channel in the UCLA simulation. The dark green x in each panel of Figure 3.1 marks the location of TC1 and the large dark blue arrows mark the earthward edge of the flow channel that corresponds to the observations. The flow channels that correspond to the Double Star observations in each simulation occur at similar times, reaching -8 R_E at ∼1826 UT, close to the time of substorm onset. Both simulations did a reasonable job of reproducing DFs at the location of the TC1 observations. However, with the sparse observations available it is difficult to determine how localized the DF was for this event, so we cannot determine whether one simulation or the other more accurately recreated the DF.

When comparing the thermal pressure contours in the UCLA and LFM results, shown in the gray lines in Figure 3.1, it becomes evident that the thermal pressure perturbations behave differently in the two simulations. Although the flow channels create an indentation in the pressure contour in both simulations, the indentation is much larger in the LFM results

Figure 3.1 *(preceding page)*: Plasma sheet results from the UCLA (top) and LFM (bottom) simulations for September 14, 2004 for each minute between 1821 and 1826 UT for the area $-30 \leq x \leq 0$ R_E, $-15 \leq y \leq 15$ R_E. Background color shows B_z [nT], the green color marks $|B_z| < 0.15$ nT. Black arrows show the velocity. Gray contours show thermal pressure separated by 500 pPa. The solid black line marks $r = 6$ R_E. The dark green x marks the TC1 location. The large arrow indicates the earthward edge of the observed DF. The blue triangle marks an example of a secondary B_z minimum earthward of reconnection. The Sun is to the right.

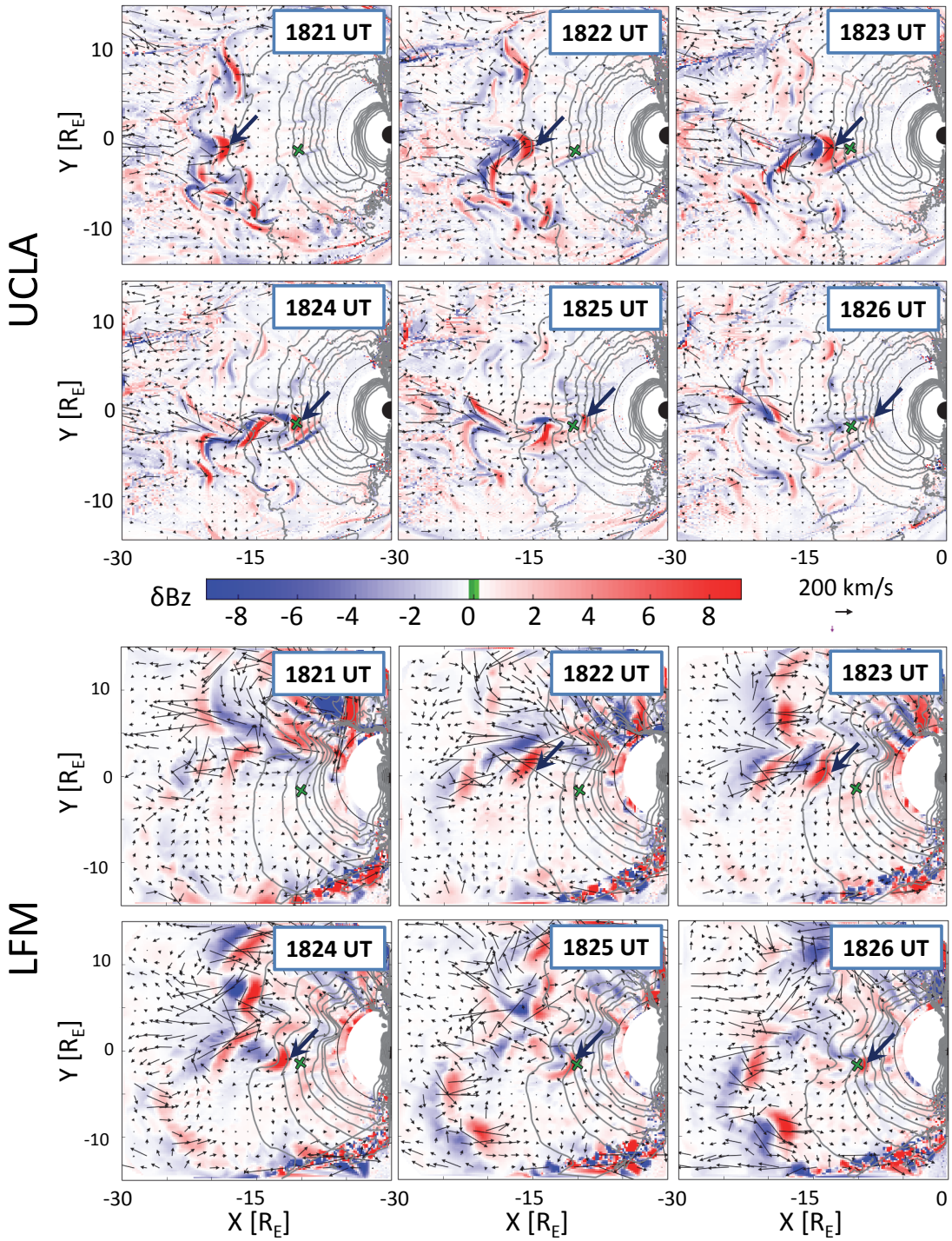
UCLA
LFM
1821 UT
1822 UT
1823 UT
1824 UT
1825 UT
1826 UT
Y [R_E]
X [R_E]
10
0
-10
-30
-15
0
δBz
-8 -6 -4 -2 0 2 4 6 8
200 km/s

than in the UCLA results. The disturbances in the pressure also damp out more slowly in the LFM results than in the UCLA results. As a result, the pressure contours become very distorted in both the radial and azimuthal directions in the LFM results, whereas they remain relatively smooth in the UCLA results.

To study the changes in the plasma sheet leading up to substorm onset in the simulations we have taken snapshots at each time step and subtracted values of the parameters at the previous time step (δt = 30 s). Figure 3.2 shows the results of the differencing for the snapshots shown in Figure 3.1. The background color is δB_z and the arrows show δv in the plane. The gray contours show the total thermal pressure giving us a reference for where the DF has formed in the simulation. The DF appears as an enhancement in δB_z that is both preceded and followed by a depression in δB_z. This structure is accompanied by an enhancement in the earthward flow.

By plotting the perturbations in the plasma sheet in this manner, we can see that the flow channel, and the associated DF, that forms in the UCLA results are very well-defined structures that form near 20 R_E and travel earthward, reaching ∼8 R_E at 1826 UT. We can also see that the flow channel that formed in the LFM simulation around 1800 UT is relatively steady. There is a set of DFs that form in the LFM simulation and travel earthward with the flow early on, but after ∼1815 UT there is relatively little change associated with the flow channel until 1820 UT when the flow channel widens and a new DF forms. As was noted above, this new DF is in the correct location to account for the observations from the Double Star (TC1) satellite in the plasma sheet and the available ground-based magnetometer. The green crosses and large blue arrows are the same as those found in Figure 3.1 and mark the TC1 location and closest approach of the observed DF to Earth at each time step.

The series of events that occur during the course of the simulation interval are similar in the two models. Reconnection begins between 1715 and 1720 UT and several flow channels

Figure 3.2 *(preceding page)*: Time differenced plasma sheet results for September 14, 2004 in the same format as Figure 3.1. The color bar shows $-10 \leq \delta B_z \leq 10nT$ and the reference vector shows $\delta v = 200$ km/s.

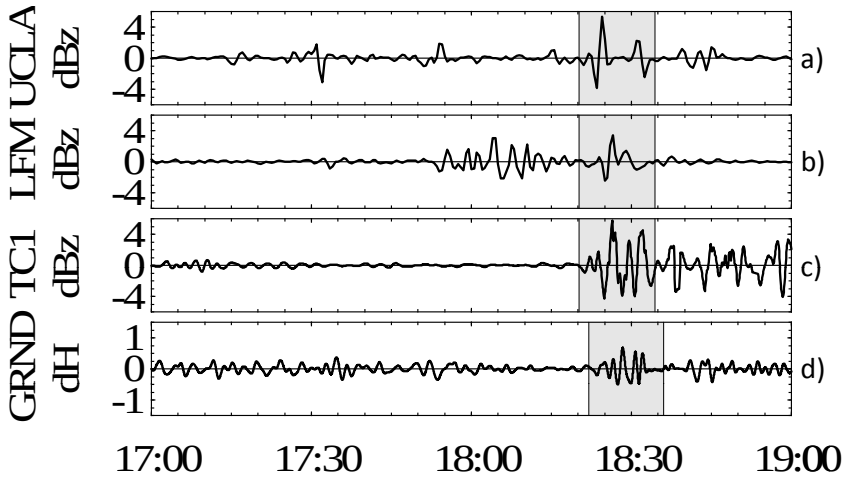

Figure 3.3: δB_Z bandpass filtered to 6-16 mHz for the interval 1700-1900 UT for a) UCLA, b) LFM simulations results near the TC1 location, and c) TC1 observations. The gray areas indicate times when the Pi2 in the simulation correspond to the TC1 measurements. Panel d shows the Pi2 pulsations measured from the ground for comparison.

form and travel earthward during the hour leading up to the substorm. Most of the activity prior to the substorm onset occurs in the dusk sector. At ∼1820 UT, a flow channel with an associated DF forms and crosses the TC1 location. Several additional DFs form and travel earthward until ∼1845 UT when the reconnection regions move tailward and activity in the near-Earth plasma sheet diminishes.

Figure 3.3 shows δB_z, filtered to Pi2 frequencies from a) the UCLA model, and b) the LFM model at the location of the Double Star (TC1) satellite, and c) Double Star observations, along with d) ground Pi2 signatures (δH). In each data set there is a DF accompanied by Pi2 period perturbations. The large peak at 1825 UT in the TC1 δB_z corresponds to the DF in the observations, however, smaller amplitude Pi2 period pulsations begin at ∼1820 UT, 5 minutes before the DF arrives. In the UCLA trace (panel a) perturbations begin at nearly the same time as the perturbations observed by TC1 and correspond to the DF indicated by the thick arrows in the top panels of Figures 3.1 and 3.2. In the LFM trace (panel b) there are perturbations beginning 1753 UT which are related to the earlier, persistent, flow channel in the dusk sector. These perturbations damp out by ∼1815 UT, then a new packet forms at ∼1823 UT. It is the second packet that agrees most closely in time and location with the available observations. There are also perturbations that begin around

1730 UT and just after 1750 UT in the UCLA simulation but the responsible flow channels are a very transient structures and the perturbations damp out quickly, whereas the flow channel in the LFM simulation is a persistent structure, as mentioned above, that continues to drive perturbations for more than 20 minutes.

Although there are some obvious differences in the two simulations, each individual simulation can account for the important features of the observations available during the event. There are flow channels generated by reconnection in the tail producing fast flows and associated DFs that travel earthward and are slowed in the braking region. The location of the flow channels in both simulations agrees well with the location of the flow channel observed by the TC1 spacecraft. The Urumqi magnetometer was located at ∼0300 MLT during the expansion phase of the substorm. In the simulations and observations available for this event the flow channel locations are within 2.5 hours of the Urumqi local time. Using a selection of 48 Pi2 events that occurred when THEMIS was in the inner magnetosphere, *Kwon et al.* (2012) has shown that space and ground observations of Pi2 are coherent if the satellite is within about 3 hours of MLT of the ground station. *Ream et al.* (2013) showed that the pulsations observed in the UCLA simulation are coherent for ∼2.5 hours MLT at a radial distance of 6 R_E, in good agreement with the observational results. The upper limit of the coherence in the LFM results is 2 hours MLT. Therefore, it is reasonable to assume that the flow channel observed by TC1 and the corresponding flow channels in the simulations would contribute to the fluctuations observed by the Urumqi magnetometer beginning at ∼1822 UT. Although there are several flow channels that form in both simulations during the substorm interval, we focus on the flow channel located closest to midnight since that structure can account for the observations available for this event. The timing for the TC1 DF also indicates that it is related to substorm onset.

3.2 Ionospheric Results

The changing properties of the ionosphere in the two simulations are shown in Figure 3.4 for 1818 UT (disturbed interval prior to onset), 1828 UT (substorm onset), and 1838 UT

(recovery phase). In general, the magnitudes of the Hall and Pedersen conductances are much higher in the UCLA simulation than in the LFM simulation. In addition, the potential is much lower in the UCLA simulation than in the LFM simulation. However, the configuration and strength of the field-aligned currents are very similar in the two models throughout the growth and expansion phases of the substorm.

Large differences in the ionospheric conductance and potential can have a dramatic effect on flow patterns in the plasma sheet. If the conductance in the ionosphere becomes too large, the flows in the tail are slowed or stopped because the field-aligned currents are insufficient to support the full solar wind potential drop across the polar cap and the ionosphere is unable to return the magnetic flux to the day side (*Coroniti and Kennel*, 1973; *Walker et al.*, 2006). Therefore, the high conductances in the UCLA model result in very small flow velocities in the near-earth plasma sheet, earthward of $\sim 8\ R_E$. In contrast, the low conductances in the LFM results allow the plasma flows to move more freely into the inner magnetosphere. This effect can be seen in Figure 3.1. Comparison of the flow vectors between UCLA and LFM shows that the flow speeds in LFM are typically higher than those in the UCLA results, particularly in the fast flow channels and in the flow moving around Earth toward the dayside. Figure 3.1 also shows that in the region $7 < r < 10\ R_E$ the velocity in the flow channels in the UCLA results drops to < 50 km/s while in the LFM results the velocity in the flow channels is > 100 km/s and only drops below 50 km/s inside of $\sim 6.5\ R_E$. In the LFM results, the flow braking region is more smeared out in radial distance and the inner edge is located closer to Earth than in the UCLA results.

Figure 3.5 shows field line traces taken from latitudes of $-80°$ to $-60°$ at 0100 MLT for 1) UCLA and 2) LFM. Panels a and b show the Pedersen conductance and the field-aligned currents for the respective simulations at 1828 UT, just after substorm onset. The numbered locations in each plot show where the foot points of the field line traces are located in the ionosphere. The top row in panels c, d, and e show the field lines in $x - z$ with v_x at y=0 plotted in color. Red shows velocity in the positive x direction and blue shows velocity in the negative x direction. The bottom row shows the same field lines in $x - y$ with B_z in color (red - positive, blue - negative). Panels 1c and 2c show a snapshot at 1818 UT during

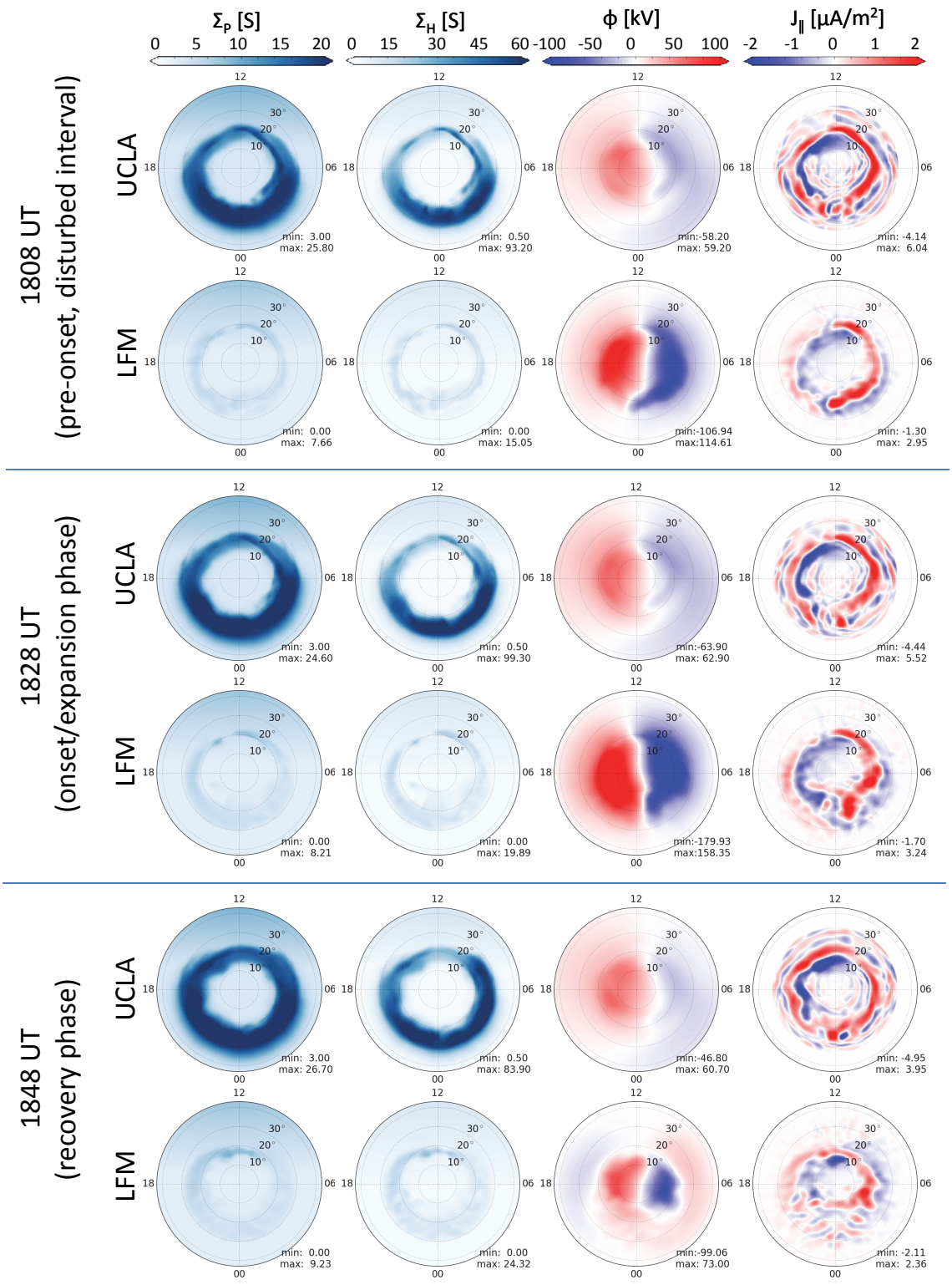
Σ_P [S]
0 5 10 15 20
Σ_H [S]
0 15 30 45 60
ϕ [kV]
-100 -50 0 50 100
$J_\parallel$ [μA/m^2]
-2 -1 0 1 2
1808 UT
(pre-onset, disturbed interval)
UCLA
min: 3.00
max: 25.80
min: 0.50
max: 93.20
min:-58.20
max: 59.20
min: -4.14
max: 6.04
LFM
min: 0.00
max: 7.66
min: 0.00
max: 15.05
min:-106.94
max:114.61
min: -1.30
max: 2.95
1828 UT
(onset/expansion phase)
UCLA
min: 3.00
max: 24.60
min: 0.50
max: 99.30
min:-63.90
max: 62.90
min: -4.44
max: 5.52
LFM
min: 0.00
max: 8.21
min: 0.00
max: 19.89
min:-179.93
max:158.35
min: -1.70
max: 3.24
1848 UT
(recovery phase)
UCLA
min: 3.00
max: 26.70
min: 0.50
max: 83.90
min:-46.80
max: 60.70
min: -4.95
max: 3.95
LFM
min: 0.00
max: 9.23
min: 0.00
max: 24.32
min:-99.06
max: 73.00
min: -2.11
max: 2.36

the disturbed interval prior to substorm onset. Panels 1d and 2d show a snapshot at 1828 UT, about 1 minute after onset during the expansion phase. Finally, Panels 1e and 2e show a snapshot at 1838 UT which is in the recovery phase of the substorm.

Although both simulations show plasma sheet thinning, in general, the plasma sheet is thicker in the LFM model than in the UCLA model, which may be due to the resistivity being purely numerical in LFM while UCLA includes an anomalous resistivity term in Ohm's law. The field lines in the UCLA model are more stretched than those in the LFM results for latitudes $> 65°$. Additionally, the field lines become open between 70° and 75° latitude in the UCLA model. In the LFM model field lines become open between 75° and 80° latitude. Figure 3.5 shows that in both simulations the field lines are dragged duskward at radial distances greater than $\sim$6 R_E. The same is true when we map field lines from the local time of Urumqi into the plasma sheet. We find that they are dragged toward midnight in the plasma sheet with the displacement becoming larger at higher latitudes. Therefore, even though the substorm is occurring near midnight the field lines map from a local time at the equator to an ionospheric location further into the dawn sector, close to the Urumqi location.

3.3 Propagation of Pi2 Pulsations Through the Braking Region

To look at the fluctuations associated with the flow channels observed in the simulations in association with substorm onset, we first identified the path of the flows in each of the simulations by selecting the points in the simulation where the flows exceeded 250 km/s. We then calculated the average y location for each x location in that region to find the average center of the flow channel as it propagated earthward. This effectively traces the path of the flow channel marked by the large blue arrows in Figures 3.1 and 3.2. To identify the fluctuations in magnetic field (radial and azimuthal components), velocity and pressure

Figure 3.4 *(preceding page)*: Ionospheric plots for a) 1808 UT, b) 1828 UT, and c) 1848 UT. The top row in each panel shows UCLA results and the bottom row shows LFM results. Columns from left to right show Pedersen conductance [S], Hall conductance [S], Potential [kV], and parallel current [$\mu A/m^2$].

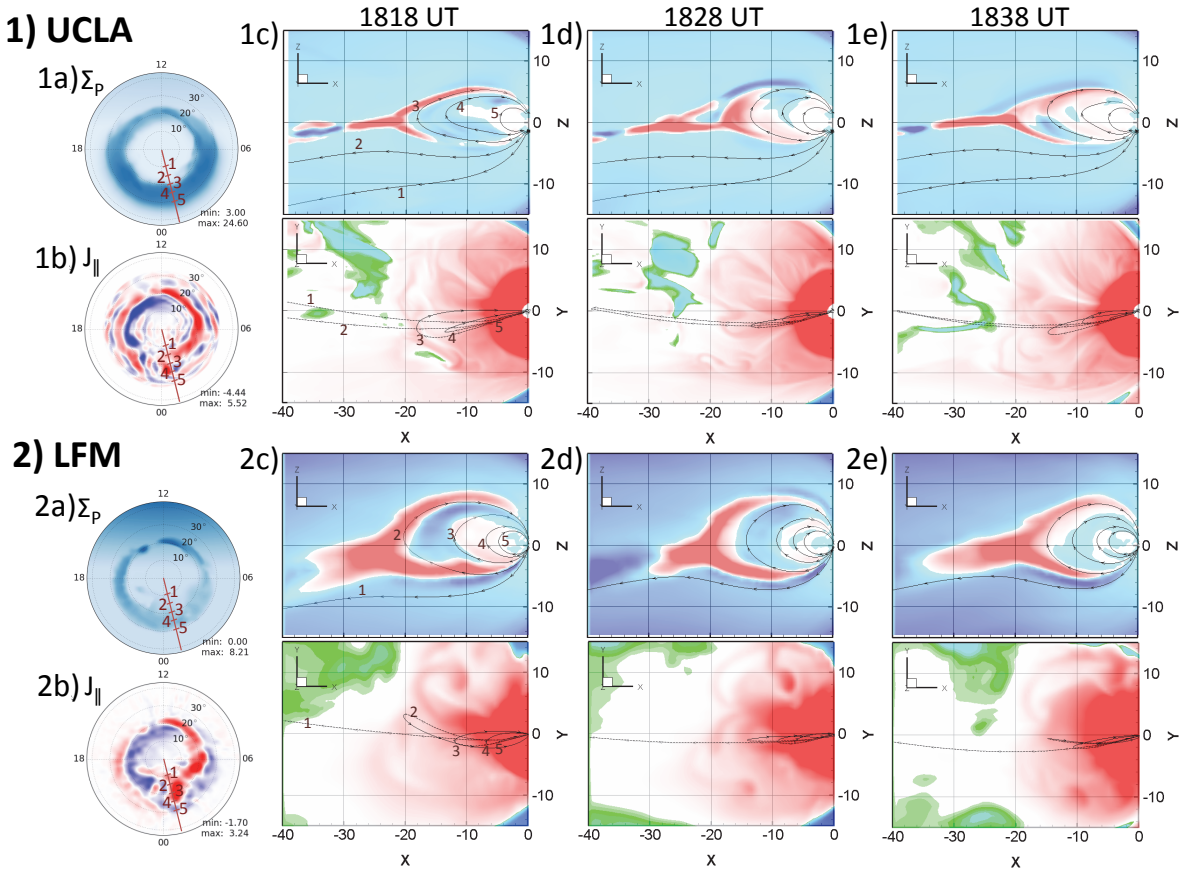

Figure 3.5: Results of field line traces from 1) UCLA and 2) LFM for times before, during, and after substorm onset. Panels show a) Pedersen conductance and b) parallel currents at 1828 UT. Field lines with footpoints at the numbered locations in panels a and b are shown at c) 1818 UT, d) 1828 UT, and e) 1838 UT. The top row in each panel shows an $x - z$ view of the field lines with v_x shown in the color background. The bottom row shows an $x - y$ view of the same field lines with B_z in the background. Field lines south of the geomagnetic equator are dashed. The numbers indicate which footpoint the field line corresponds to in panels a and b.

in the flow channel, we averaged across 15 minutes of MLT on the dawn half of the flow channel at fixed radial distances and plotted the results as a function of radial distance and time. Only the dawn half of the flow channel was selected because the fluctuations in δB_ϕ are ideally anti-symmetric about the center of the flow channel as a result of the oppositely directed vorticity generated on either side of the flow channel as the flow travels earthward. As a result field aligned currents are directed upward (into the ionosphere) on the dawn side and downward (out of the ionosphere) on the dusk side of the flow channel.

The magnetic field and velocity fluctuations for the interval 1700-1800 UT in the region 5-15 R_E are plotted in Figure 3.6. The columns show a) B_z, b) B_ϕ and c) $|v|$ for UCLA (top) and LFM (bottom). B_z and $|v|$ were taken at the center of the plasma sheet. B_ϕ was taken 1.5 R_E above the center of the plasma sheet because at the center of the flow channel, in the plasma sheet B_ϕ is very close to zero so the perturbations are minimal. Color plots show the total value for each of the three components with the path of the DF indicated by the solid black line. The path of the DF was determined by using the beginning of the enhancement in the total B_z in column a). The line plots show radial cuts at 6.0, 6.5, 7.0, 7.5, and 8.0 R_E bandpass filtered to 6-16 mHz (16 mHz is the Nyquist frequency for the simulation output). Red arrows indicate the crossing time of the DF. There are Pi2 period perturbations in B_z, B_ϕ, and $|v|$ in both simulations; however, there is also a significant broadband signal in B_z. The broadband signal is more prominent in the UCLA simulation than in LFM. With the limited observations available in the tail for this event, it is difficult to determine which simulation has more accurately reproduced the event itself. However, in general, both models show Pi2 period perturbations associated with the flow channels that form in the plasma sheet, and reproduce TC1 observations, even though the models use dramatically different grids and numerical methods to solve the set of MHD equations. As a result we believe that the modeled Pi2 period pulsations are inherent in the MHD description of the system and are independent of the initial set-up and the numerical methods used.

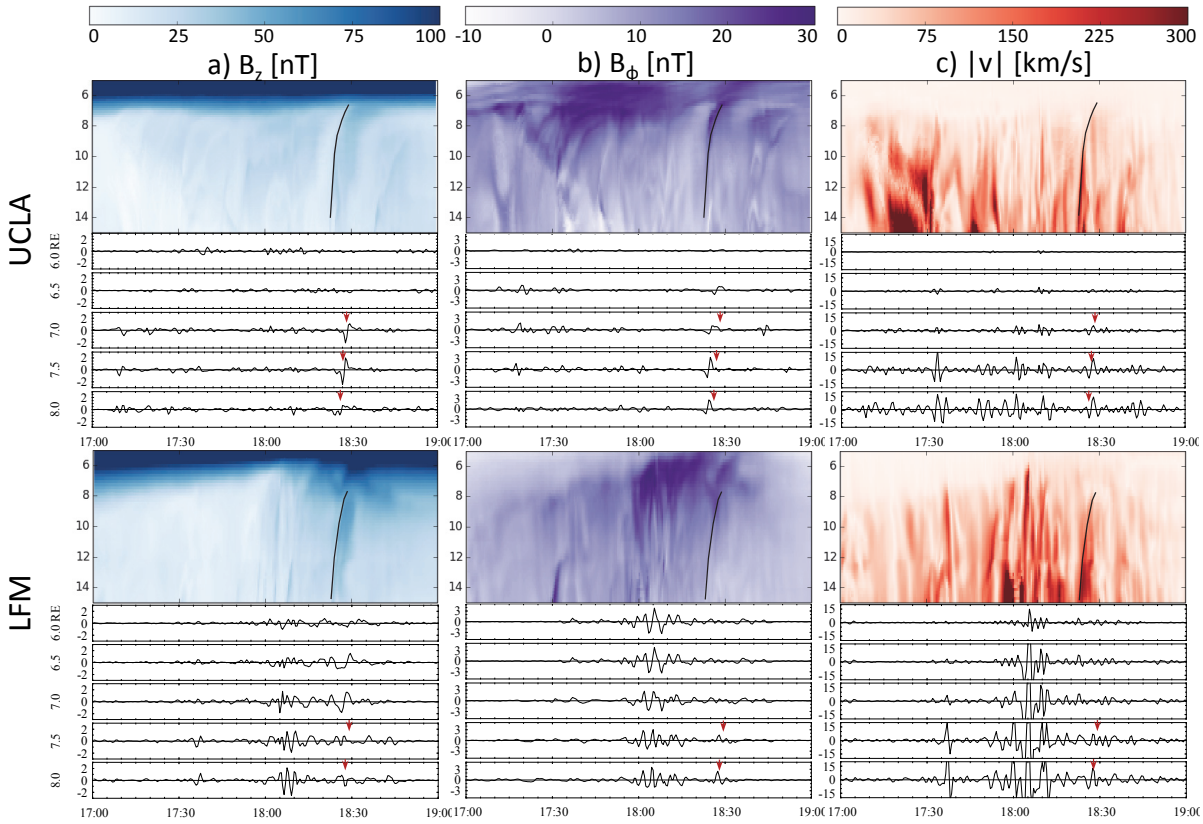

Figure 3.6: Average quantities and perturbations for 15 minutes of MLT on the dusk half of the flow channels that correspond to TC1 measurements as identified in Figures 3.1 and 3.2 for UCLA (above) and LFM (below) between 1700 and 1900 UT. From left to right, color plots show the average quantities B_z, B_ϕ, and $|v|$ plotted versus radial distance from Earth and time. The black line shows the path of the DF through the system determined using B_z and copied onto the other panels. The line plots show cuts between 6 and 8 R_E for each of the components bandpass filtered to 6-16 mHz (the portion of the Pi2 band that can be resolved in the simulations). Red arrows indicate the DF crossing time at each radial distance.

3.4 Ionospheric Conductance, Magnetospheric Convection and Wave Propagation

Throughout the magnetotail, flow velocities in the LFM simulation are typically higher than those in the UCLA simulation (see Figure 3.1). Because the flows do not propagate as far earthward in the UCLA simulation, the perturbations carried by the flow channels are also not able to penetrate as far into the inner magnetosphere. This effect can be seen in the line plots in Figure 3.6. Fluctuations in the flow velocity and magnetic field diminish to noise levels before reaching 6.5 R_E in the UCLA results while in the LFM results the fluctuations are still evident at 6.0 R_E. This is likely a result of the differences in the ionospheric conductance models used in the simulations (see Section 1.5.2). Figure 3.4 shows very clearly that the magnitudes of the conductances in the UCLA model are much higher than those in the LFM model. The high Pedersen conductance in the UCLA simulation effectively stops the earthward flow in the tail inside of ~7.5 R_E (*Coroniti and Kennel*, 1973; *Walker et al.*, 2006). In contrast, the flow in the LFM simulation is able to penetrate much further earthward; in some cases as far as 5 R_E.

In order to confirm our interpretation of the effects of the different Pedersen conductances in the two models, we compare two additional simulations run with the same model, in this case the UCLA model, with different ionospheric conductances. Only the UCLA model was used in order to isolate the effects of the conductance. Both simulations were driven by constant idealized solar wind conditions. Solar wind conditions were $v_x = 450\ km/s$, $n = 10\ cm^{-3}$, and $P = 20\ pPa$. The IMF was set to a constant $-5\ nT$ for the entire 4 hour simulation interval. The only difference in the two simulations is in the Pedersen conductance (Σ_P). For Run 1 $\Sigma_P = 6\ S$. For Run 2 $\Sigma_P = 20\ S$. The results of the simulations can be seen in Figure 3.7. The figure shows that in Run 1 fast flow channels have formed by t=3600 s, one hour into the simulation. Fast flows continue to form and propagate earthward until t=10800 s. In Run 2 we also see that the flow channels form in the simulation by t=3600 s. However, by t=7200 s those flows have died out and no new flow channels are propagating into the near-Earth region. In general, the larger the Pedersen conductance, the fewer the

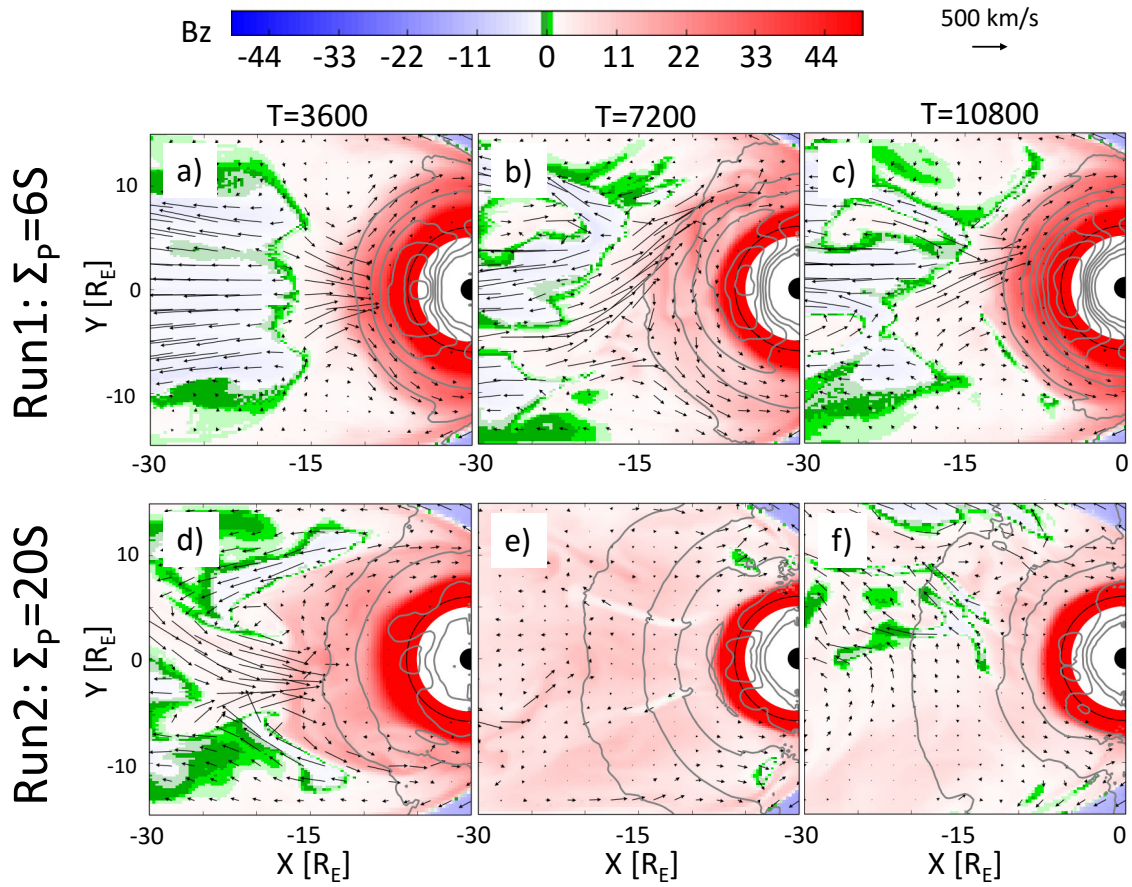

Figure 3.7: Simulation results from Run 1 ($\Sigma_P = 6\ S$) in panels a-c, and Run 2 ($\Sigma_P = 20\ S$) in panels d-f. Simulation times from left to right are t=3600, 7200, and 10800 for each simulation. Background color shows B_z. Arrows show the velocity in the plane.

flow channels. Those that develop for large Σ_P stop further out in the tail. Run 1, with low Σ_P gives results similar to the LFM results where the Pedersen conductance stays low throughout the event and fast flows continue to form and propagate into the near-Earth region well into the recovery phase. Run 2, on the other hand, gives results similar to those found in the UCLA simulation for the current event study. Flow channels form early on in the simulation but as the event progresses, the Pedersen conductance increases and fast flows are stopped further out in the magnetotail. A very large magnetic field gradient also forms in Run 2 which can be seen in Figure 3.7, panels e and f. This is similar to the magnetic field gradient that forms in the UCLA model (see Figure 3.1). The ionospheric results for Run 1 and Run 2 also correspond to the LFM and UCLA results, respectively, for the September 14 event. In Run 1, with low Pedersen conductance, the potential gets very large, with $\Delta\Phi$ exceeding 150 keV, similar to the values seen in the LFM simulation. In Run 2, with high Pedersen conductance, $\Delta\Phi$ stays well below 100 keV throughout the simulation, similar to the UCLA results for September 14. Since the only difference between the two runs is the magnitude of the Pedersen conductance, it is reasonable to conclude that the conductance is responsible for the differences in the magnetotail dynamics. This, along with the similarities between the simulations mentioned above, suggests that the Pedersen conductance is also responsible for differences between the UCLA and LFM results for the current event study.

Figure 3.8 shows the magnitude of $\mathbf{v}\times\mathbf{B}$ at the location of the flow channel for UCLA (top) and LFM (bottom) in the same format as the color panels in Figure 3.6. The flux transport in the UCLA model falls to very low values between 6 and 7 R_E, near the inner edge of the plasma sheet. In the LFM model the flux transport stays relatively high across the inner edge of the plasma sheet. This difference in the flux transport is due primarily to line-tying but the pressure gradients in the two simulations also play a role in how far earthward the flows are able to penetrate (*Coroniti and Kennel*, 1973; *Ashour-Abdalla et al.*, 2002; *Walker et al.*, 2006). Thermal pressure for Run1, Run2, UCLA and LFM at three times are shown in Figure 3.9. In both Run1 and LFM, the largest pressure gradients are closer to Earth than in Run2 or the UCLA simulation. As a result, the flow speeds decrease at larger radial distance in the UCLA model so the flow channels are not able to penetrate as

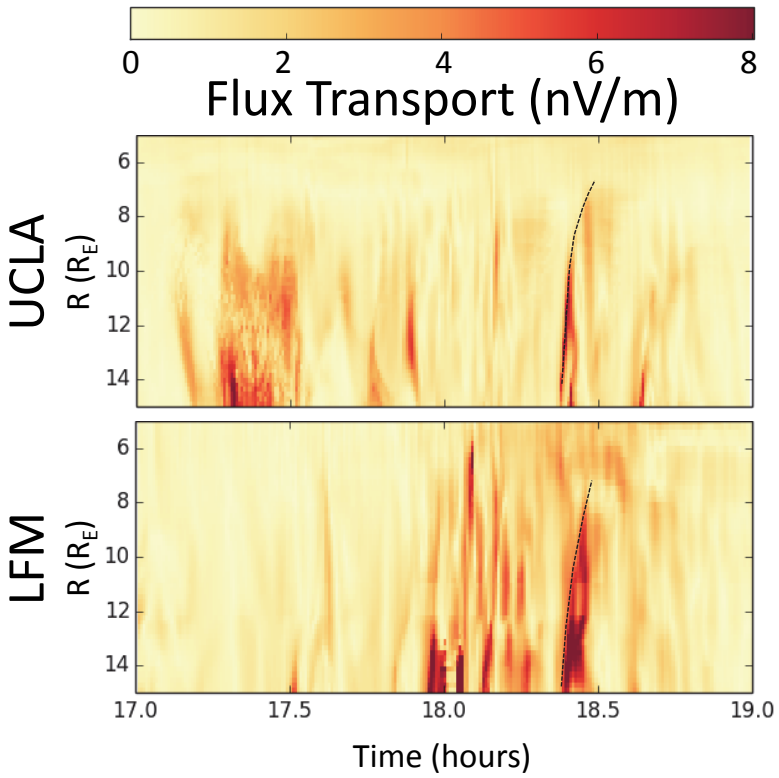

Figure 3.8: The flux transport $|\mathbf{v}\times\mathbf{B}|$ plotted in the same format as the color panels in Figure 3.6 for UCLA (top) and LFM (bottom).

far earthward as those in the LFM simulation. With the exception of the magnitude of the thermal pressure being larger overall in the UCLA results, Run2 and the UCLA results look very similar. Both have strong flows early on followed by an increase in the pressure out to radial distances greater than 10 R_E. As the pressure increases the flows are stopped further back in the tail. Run1 and LFM also look very similar with a larger pressure gradient closer to the planet and flows penetrating to radial distances less than 8 R_E.

The two simulations also differ in the thickness of the plasma sheet (see Figure 3.5) and in the size and duration of the flow channels that form in the plasma sheet (see Figures 3.1 and 3.2). Given these differences, when we look at the perturbations generated in the flow channels observed in the simulations near the time of substorm onset we see that Pi2 period fluctuations are being generated in both simulations in the same way. Perturbations in B_z develop with the flow channel, and the DF that forms at the earthward edge of the flow channel. In Section 2.4 we showed that the frequency of the perturbations associated

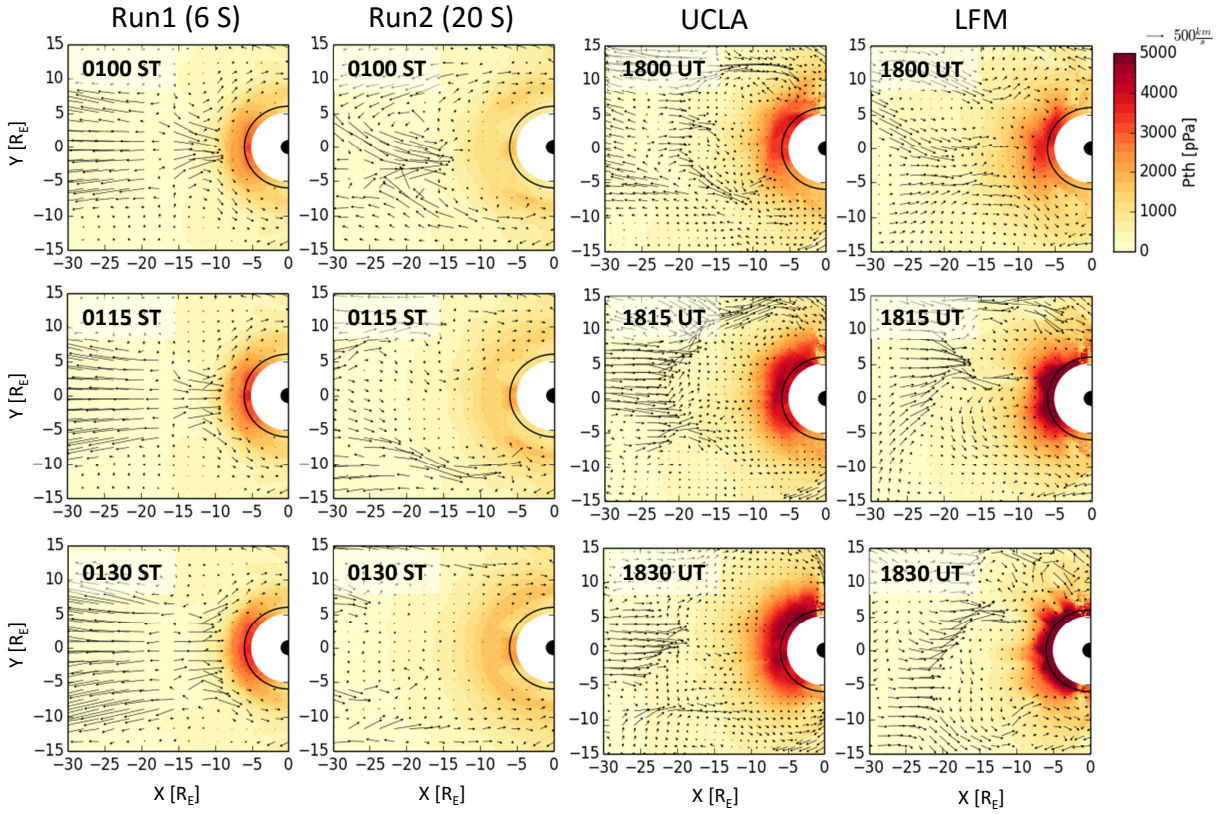

Figure 3.9: Thermal pressure (Pth [pPa]) in the plasma sheet for, from left to right, Run1, Run2, UCLA and LFM. The rows from top to bottom show results at 0100 ST/1800 UT, 0115 ST/1815 UT, and 0130 ST/1830 UT for the generic runs/event study. arrows show the velocity in the plane

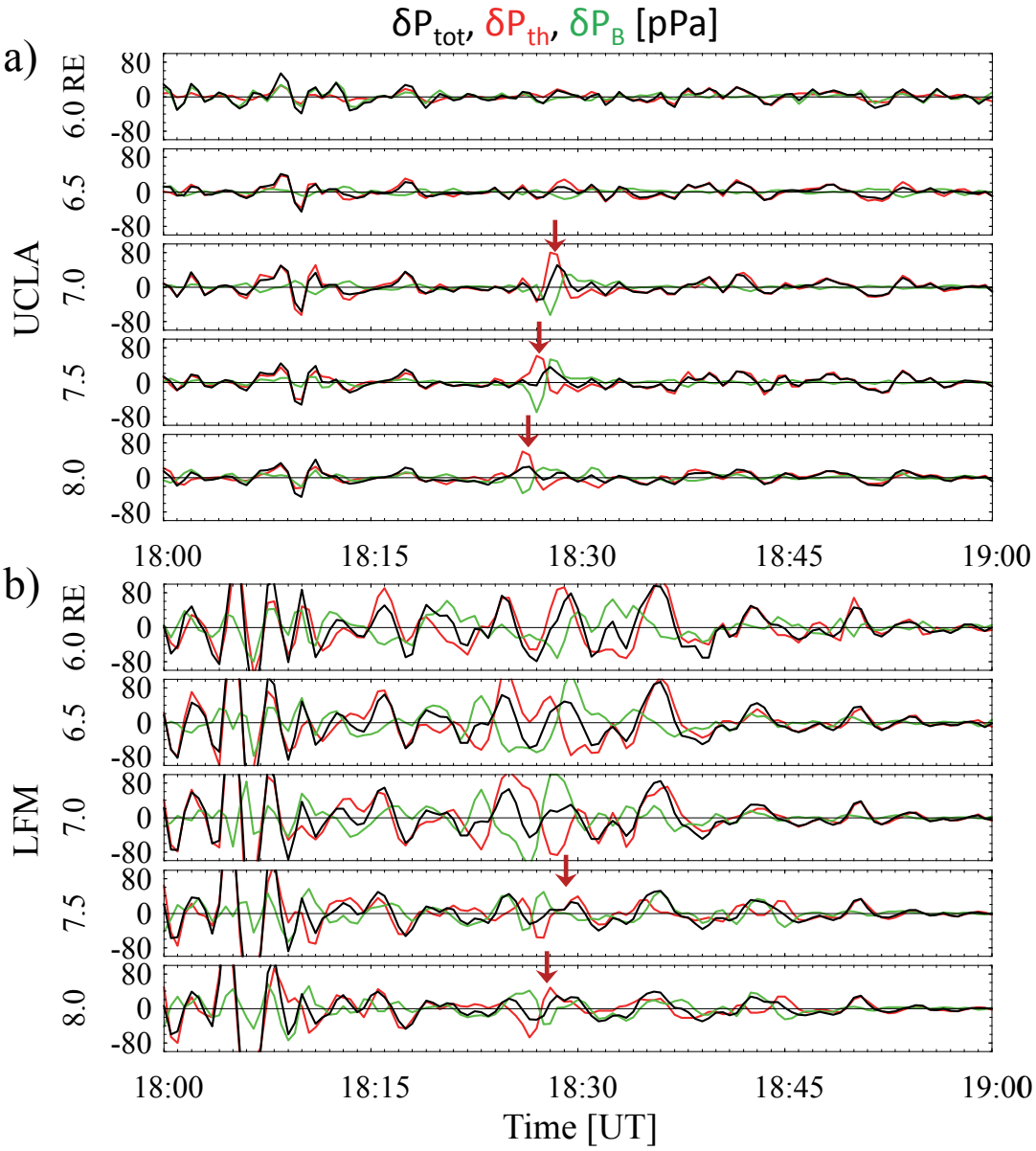

Figure 3.10: Pressure perturbations in the dusk half of the flow channel plotted in the same format as the line plots in Figure 3.6 for the interval 1800-1900 UT. Traces show δP_{total} (black), δP_{th} (red) and δP_{mag} (green) for a) UCLA and b) LFM.

with the flow channel inside of ∼-12 R_E is within the Pi2 spectrum. The fact that the frequency of the perturbations increases as the flow channel propagates earthward supports the Transient Response (TR) model for Pi2 generation. Pi2 period fluctuations also develop in B_ϕ in association with the vortices that form on either side of the flow channel, generating field aligned currents (see Figure 2.15), in support of the Inertial Current (IC) mechanism for Pi2 generation that is included in the bursty flow model (*Kepko et al.*, 2001; *Keiling et al.*, 2009; *Ream et al.*, 2013). Because the period for the TR fluctuations depends on the Alfvén transit time, and both simulations have similar results for the lengths of the field lines, density and magnetic field magnitudes tailward of ∼-7 R_E, both simulations exhibit similar periods related to the flow channels at substorm onset in that region. In the UCLA model, earthward of -7 R_E line tying damps the earthward propagation of the disturbance. However, in the LFM model the perturbations are able to propagate much further earthward, so the simulation results look very different in that region.

In both simulations the braking region lies in the region $-8 > x > -6$ R_E consistent with the source region for Pi2 period compressional waves identified by *Uozumi et al.* (2007). As the flow channel and its associated DF travel through the braking region and approach the inner edge of the plasma sheet, the perturbations begin to travel ahead of the DF. This effect is most evident in B_ϕ (Figure 3.6 column 2) where the separation between the beginning of the perturbations and the red arrow marking the crossing time of the DF gets larger as the disturbance propagates earthward. The separation of the DF and the Pi2 period fluctuations in the braking region supports the idea proposed by *Kepko et al.* (2001), that a compressional wave traveling ahead of the DF into the inner magnetosphere could generate Directly Driven (DD) Pi2 pulsations at mid- to low latitudes on the ground. As the compressional wave travels earthward it couples to an Alfvén wave and is transported into the ionosphere where it can be observed by magnetometers on the ground (*Uozumi et al.*, 2009, 2011).

Figure 3.10 shows the perturbations in the pressure for the interval 1800-1900 UT for a) UCLA and b) LFM. The traces show total pressure (black), thermal pressure (red), and magnetic pressure (green) at 6.0, 6.5, 7.0, 7.5 and 8.0 R_E associated with the flow channel identified in Figure 3.1. The red arrow marks the time of the DF crossing at

each radial distance. In both simulations, the fluctuations associated with the DF show a mixed mode compressional wave with the thermal and magnetic pressure nearly out of phase and significant fluctuations in the total pressure. This agrees well with observations of magnetotail Pi2 by *Nakamizo and Iijima* (2003), which showed that the thermal and magnetic pressure fluctuations associated with the Pi2 fluctuations were out of phase. The pressure fluctuations (magnetic, thermal and total) in LFM and UCLA have the about same amplitude at 7.5 and 8.0 R_E, however, at 7.0 R_E the amplitude of the pressure fluctuations in LFM start to get larger while the pressure fluctuations in the UCLA results do not. Pressure perturbations travel further earthward in the LFM model and the oscillations become very large at radial distances smaller than 7.5 R_E. Meanwhile, pressure perturbations in the UCLA model decay earthward of $\sim$7.0 R_E. As noted above, this is most likely an effect of the differences in the conductances between the two models. The line-tying in the UCLA model is so strong that the flow perturbations are not able to propagate earthward of 7.0 R_E. Based on the pressure perturbations shown in Figure 3.10, the compressional wave propagates more easily into the inner magnetosphere in the LFM model than in the UCLA model. However, as mentioned above, based on the line plots in Figure 3.6, both simulations show a compressional wave traveling ahead of the DF as it slows in the braking region.

3.5 Summary

We have used two different 3D global MHD models, UCLA and LFM, to model the generation and propagation of Pi2 pulsations during a substorm event on September 14, 2004. Although we are unable to rule out plasmaspheric eigenmodes as a source for Pi2 pulsations observed on the ground, the simulations demonstrate that, in some cases, fast flows in the plasma sheet are directly responsible for generating Pi2 pulsations. When we focus on the flow channel that forms around the time of substorm onset in the simulations, we observe Pi2 period perturbations inside $\sim$-12 R_E in the magnetic field, velocity and pressure propagating at the same speed as the DF at the earthward edge of the fast flow until it reaches the braking region in agreement with the Transient Response model for Pi2 *Southwood and Stuart* (1980); *Kepko*

et al. (2001). Pi2 period perturbations are observed in B_y in association with the vortices that form on either side of the flow channel in support of the Inertial Current component of the bursty flow model. As the DF approaches the inner edge of the plasma sheet and is slowed in the braking region, the perturbations begin to travel ahead of it as a mixed mode compressional wave. These propagating compressional waves generated by the fast flows in the braking region can produce Pi2 pulsations observed on the ground as described by the bursty flow model for Pi2 generation (*Kepko and Kivelson*, 1999; *Kepko et al.*, 2001, 2004).

Although the perturbations are generated in the same way in both models, the propagation of the perturbations into the inner magnetosphere is greatly affected by the differences in the ionospheric models in the simulations. The high Pedersen conductance ($\sim$25 S) in the UCLA results causes the flow channels and the perturbations to stop propagating earthward at $\sim$7 R_E, whereas the perturbations in the LFM results, with its maximum Pedersen conductance around 9 S, are able to propagate more easily into the inner magnetosphere.

CHAPTER 4

Isolated Substorm Case Study: August 25, 2013

A non-storm-time isolated substorm event has been carefully selected using multi-point observations in the magnetotail as well as ground-based observations. The criteria for the event selection included good ground coverage on the night side from mid- to high latitudes, including auroral imaging, good satellite coverage on the night side inner magnetosphere, and good coverage in the tail with a focus on plasma sheet measurements. Multiple satellite observations in the tail, including observations of DFs, are important both for timing the events of the substorm and validating the simulation results. Good coverage on the ground is necessary in order for us to compare the observations to simulation results to identify distinct driving mechanisms for Pi2 observed at different latitudes.

4.1 Event Selection

We have selected a substorm that occurred at 0505 UT on August 25, 2013 for this study. The event we have selected has excellent coverage in both the night side plasma sheet and on the ground. There are a total of 11 satellites available in the magnetotail. In addition, there are observations available from more than 50 ground-based magnetometers across North America and Greenland, which show the presence of Pi2 pulsations across much of the continent. This event fits the criteria described above very well with one exception. The substorm begins a steady magnetospheric convection (SMC) interval, so it does not have a typical recovery phase. However, the purpose of this study is to determine the origin of the pulsations that begin with the substorm onset so it is not crucial that the recovery phase be well defined.

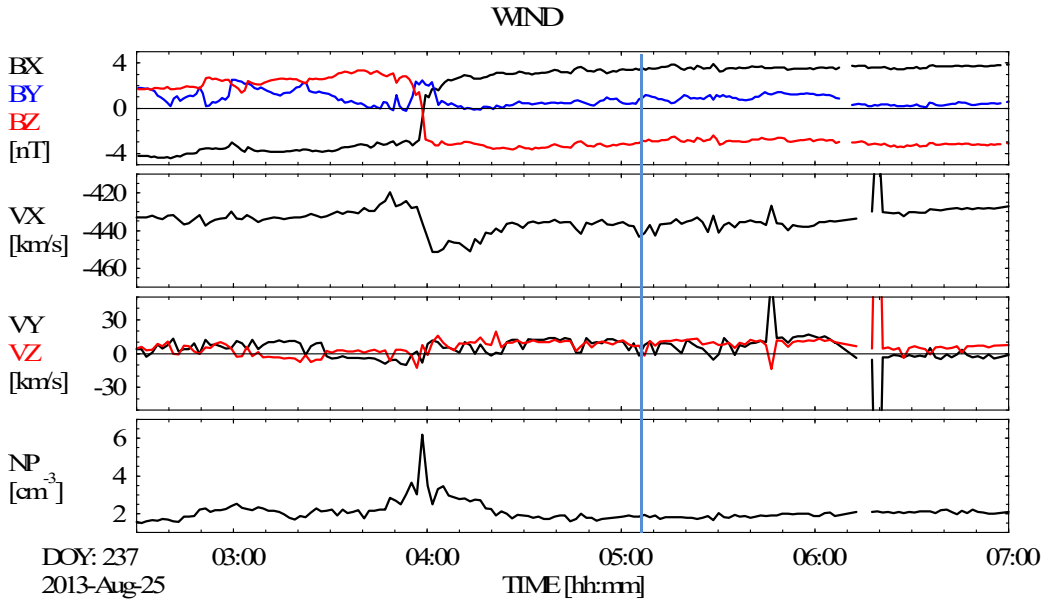

Figure 4.1: Solar wind measurements from the Wind spacecraft for August 25, 2013, propagated to the bow shock. The interval shown is 0200-0700 UT. Panels show a) B_x (black), B_y (blue), B_z (red) $[nT]$, b) v_x $[km/s]$, c) v_y (black), v_z (blue)$[km/s]$, and d) density $[cm^{-3}]$. The blue vertical line marks substorm onset.

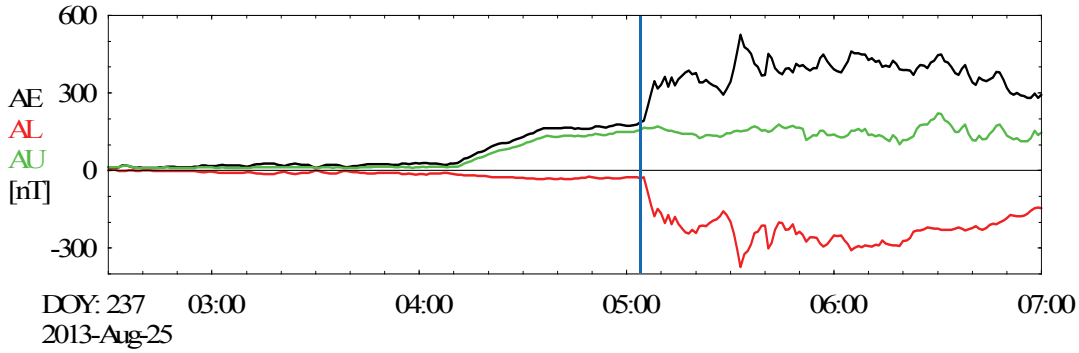

Figure 4.2: Auroral indices, AE (black), AL (red), and AU (green) [nT], for August 25, 2013, 0200-0700 UT. The blue vertical line marks substorm onset.

Wind was used as the solar wind monitor for the event. Solar wind measurements propagated to the bow shock for the interval 0200-0700 UT are shown in Figure 4.1. The panels show a) B_x (black), B_y (red), B_z (green) $[nT]$, b) v_x, c) v_y (black), v_z (red) $[km/s]$, d) density $[cm^{-3}]$. There is a rotation in the interplanetary magnetic field (IMF) at ∼0400 UT when the IMF B_x becomes positive and IMF B_z becomes negative. The IMF stays in this configuration until ∼0900 UT.

4.1.1 Ground-based Observations

We determined that the substorm began at ∼0504 UT by using the AL index (see Figure 4.2). Figure 4.2 shows the Auroral indices (AL – black, AL – red, AE – green) for the event between 0230 and 0700 UT. Based on the AL index the growth phase begins with the southward turning at 0400 UT. There is a steady decrease in AL until ∼0430 UT. After ∼0430 UT AL plateaus until ∼0504 UT when the expansion phase begins. Following the expansion phase AL remains low as the event enters into an interval of steady magnetospheric convection. THEMIS All Sky Imagers (ASI) show auroral break-up beginning at 0503:30 UT over the north-eastern United States. Figure 4.3 shows images taken from SNKQ between 0503 and 0504 UT. There is a pre-existing arc beginning around 0503. The poleward arc brightens and begins to expand between 0503:20 and 0503:40 indicating the beginning of the expansion phase of the substorm.

Magnetometer chains throughout the United States, Canada, and Greenland offer extensive ground observations for this event. The H component (black) and the δH (red) of the magnetic field for one magnetometer chain, located between 270° and 278° longitude, near the longitude of Niagra Falls, that stretches from $\sim$ 79° to $\sim$ 39° magnetic Latitude (mLat) is shown in Figure 4.4. The local time at substorm onset for these stations is 12:04 am. The line plots in Figure 4.4 show that the Pi2 period perturbations begin concurrently with the positive bay in the four lower latitude stations. The high latitude station, which is located in the polar cap, also shows pulsations that begin about a minute earlier than at the mid-latitude stations and before the increase in H.

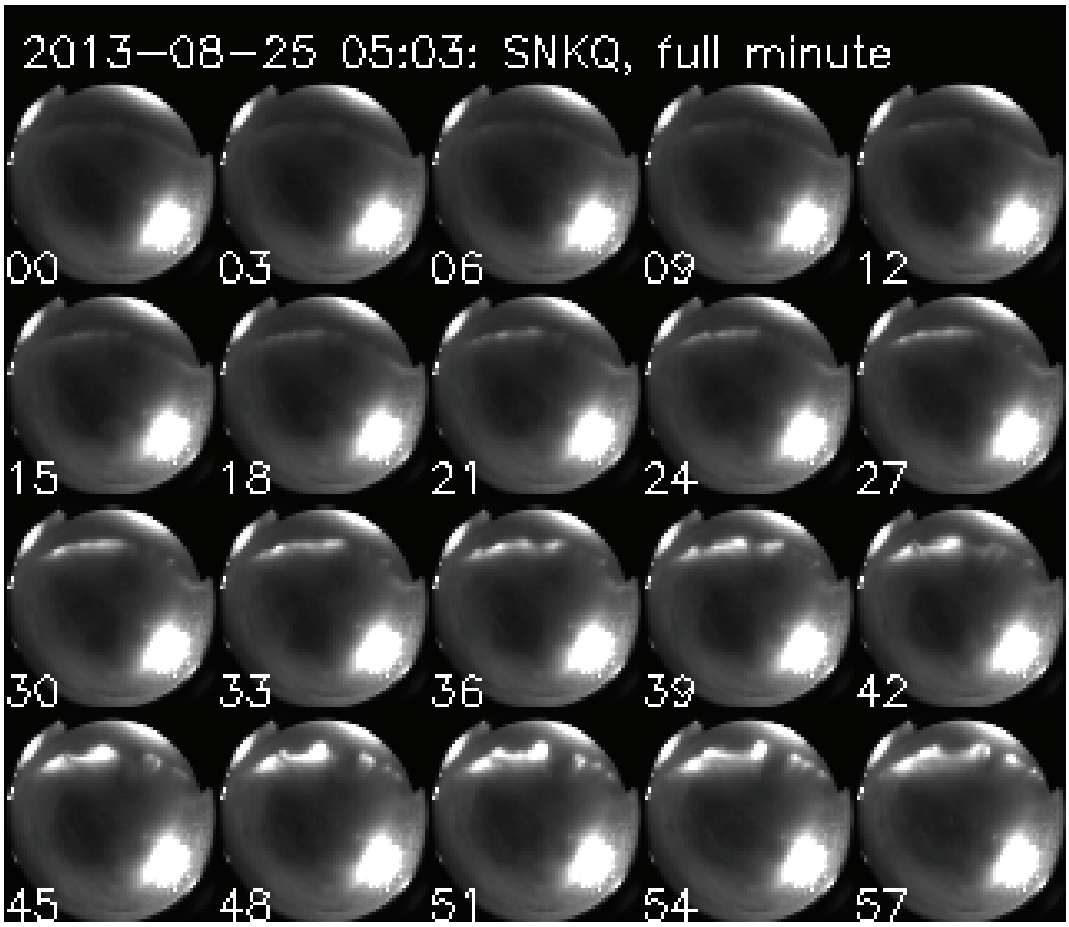

Figure 4.3: THEMIS All Sky Imager (ASI) observations from Sanikiluak (SNKQ) for the interval 0503-0504 UT at 3 second intervals.

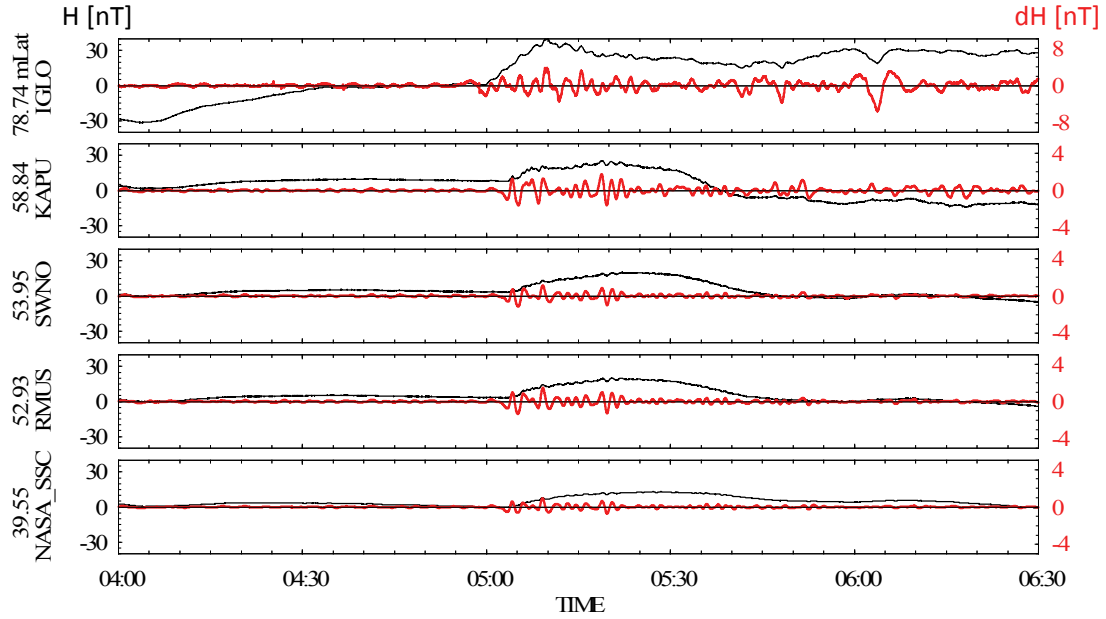

Figure 4.4: Ground measurements from stations between 270° and 278° longitude and ∼ 79° to ∼ 39° magnetic Latitude (mLat). Black traces show the total H component, red traces show observations bandpass filtered to Pi2 frequencies (6-25 mHz). The latitude and station identifier are indicated on the left side of the figure.

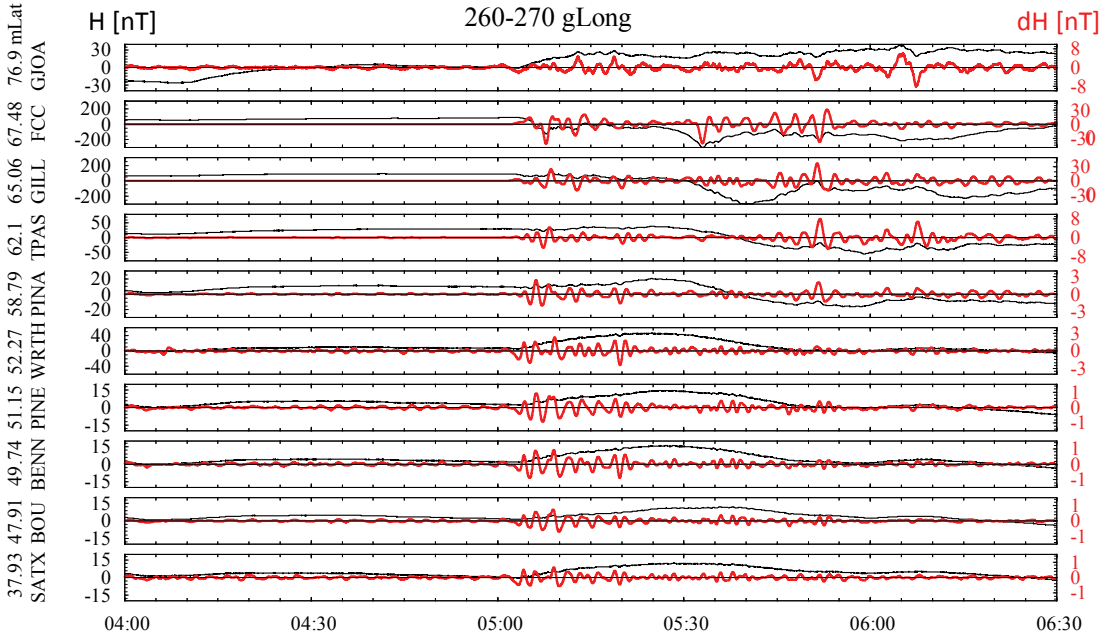

Figure 4.5: Ground station observations between 254° and 266° longitude and ∼ 77° to ∼ 38° magnetic Latitude (mLat) plotted in the same format as Figure 4.4.

Another magnetometer chain, located between 254° and 266° longitude, that stretches from ∼ 77° to ∼ 38° magnetic latitude (mLat) is shown in Figure 4.5. The format is the same as Figure 4.4. Local times for these stations are 10:04 to 11:04 pm at substorm onset The black traces show that there is a drop in the H component of the magnetic field at the Fort Churchill station, located at 67.5° mLat. The higher latitude station (GJOA) is located in the polar cap. At all latitudes below 62° there is a positive bay in the H component. The red traces show that the Pi2 onset at each station coincides with the decrease/increase in H. This figure indicates that the pulsations extend well beyond the location of the substorm onset in both latitude and longitude. This is typical of Pi2 signatures.

4.1.2 Magnetospheric Observations

During the event we have several satellites in the tail. The locations of the available satellites is shown in Figure 4.6. Cluster and THEMIS A and D are available in the plasma sheet giving good coverage across the dusk sector. Observations from the CLUSTER spacecraft, located near (-10.5, 3.0, 0.0) R_E GSM, are shown in Figure 4.7. The panels show B_x (black), B_y (blue), and B_z (red) [nT] for a) C1, b) C2, c) C3 and d) C4, along with d) v_x [km/s] for C4. THEMIS A, located at (-8.80, -2.10, -0.10) R_E GSM, is shown in Figure 4.8. The panels show a) B_x (black), B_y (blue), and B_z (red) and, b) v_x (black) [km/s].

The initial fast flow was observed by the Cluster spacecraft at ∼0504 UT and was accompanied by fluctuations in the magnetic field. A second fast flow accompanied by a dipolarization front (DF) is observed by all four of the Cluster spacecraft at ∼0506 UT. Pi2 period fluctuations are observed concurrently with the dipolarization front. THEMIS A also observes a DF at ∼0506 UT. This however is most likely not the same DF that was observed by Cluster due to the large spatial separation of ∼5 R_E in y of the spacecraft. So several DFs must have been present at different local times in the tail at the time of substorm onset.

GOES 13 and 15 and THEMIS D are available in the inner magnetosphere. Figure 4.9 shows observations from the three spacecraft. The top three panels show GOES 13 magnetic field mesuarements a) B_x, b) B_y, and c) B_z [nT] GSM. The next three panels show GOES 15

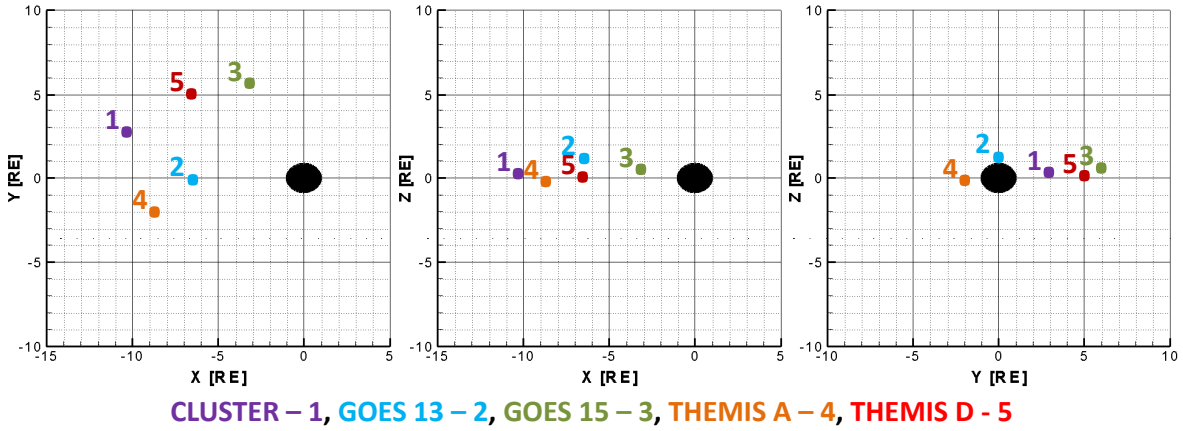

Figure 4.6: The configuration of satellites available for the substorm. Satellites shown are Cluster (A), GOES 13 (B), GOES 15 (C), THEMIS A (D), and THEMIS D (E). Panels show configuration in the a) the xy-plane, b) the xz-plane, and c) the yz-plane.

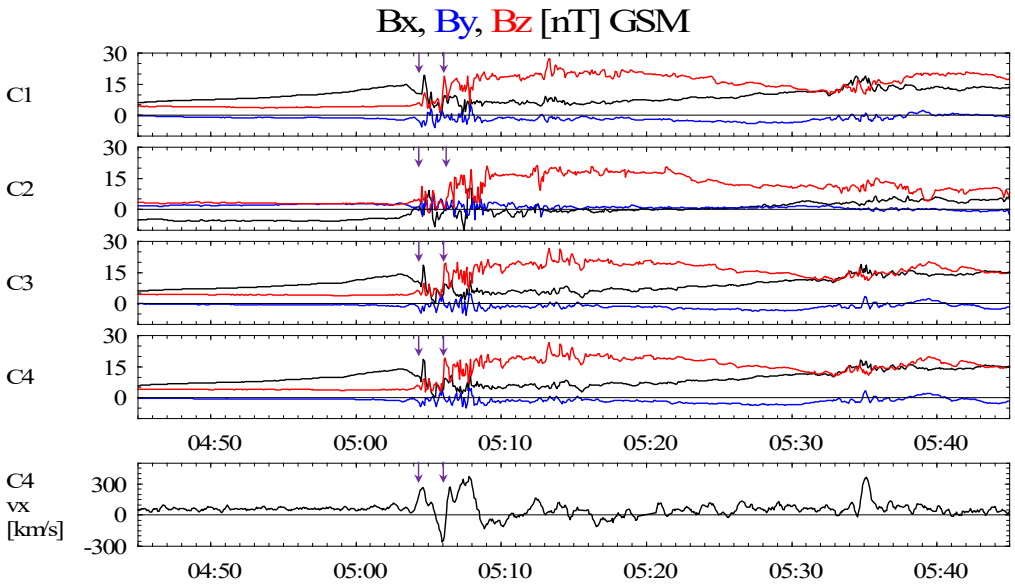

Figure 4.7: Observations from the 4 CLUSTER spacecraft for the interval 0445-0545 UT on August 25, 2013. The panels show B_x (black), B_y (blue), and B_z (red) [nT] for a) Cluster 1, b) Cluster 2, c) Cluster 3, and d) Cluster 4. Panel e) shows v_x [km/s] for Cluster 4. Purple arrows indicate the arrival of fast earthward flows and their accompanying DFs.

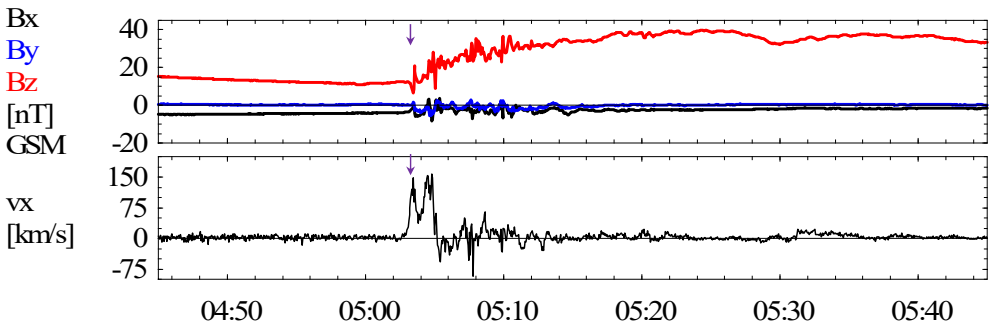

Figure 4.8: Observations from THEMIS A are shown for August 25, 2013, for the interval 0400-0600 UT. Panels show a) B_x (black), B_y (blue), and B_z (red) [nT], and b) v_x [km/s]. Purple arrows indicate the arrival of fast earthward flows and their accompanying DFs.

magnetic field measurements, d) B_x, e) B_y, and f) B_z [nT] GSM. The final four panels show THEMIS D observations g) B_x, h) B_y, i) B_z [nT], and j) v_x [km/s]. GOES 13 is located very close to the location of the substorm onset. Although it does not observe a dipolarization front signature there are Pi2 period pulsations observed in both B_z and B_x at ∼0504 UT. GOES 15 duskward of GOES 13 at the time of substorm onset and does not observe any Pi2 period pulsations at onset. It does, however observe some fluctuations at ∼0532 UT. THEMIS D was located between the two GOES satellites in the inner magnetosphere at (-6.37, 4.72, 0.01) R_E GSM. THEMIS D does not observe Pi2 period pulsations at the time of substorm onset, but it does observe a packet of Pi2 period perturbations about 30 minutes later at ∼0533 UT. This indicates that an additional DF in the dusk sector formed simultaneously with the DF observed by the CLUSTER spacecraft during the expansion phase of the substorm.

Geotail is also available for this event. The spacecraft is located in the northern lobe at (-29.67, 4.24, 8.45) R_E GSM. There is a loading-unloading event in the lobe magnetic field observations, seen as a peak in B_x at 0505 UT, in agreement with the substorm onset time.

Based on the available observations from both the ground and satellites, the substorm begins just prior to midnight in local time. This is based on the DF observed by the CLUSTER satellites, the perturbations observed by the GOES 13 satellite, and the auroral all sky images and magnetometer observations from the ground. At least one additional

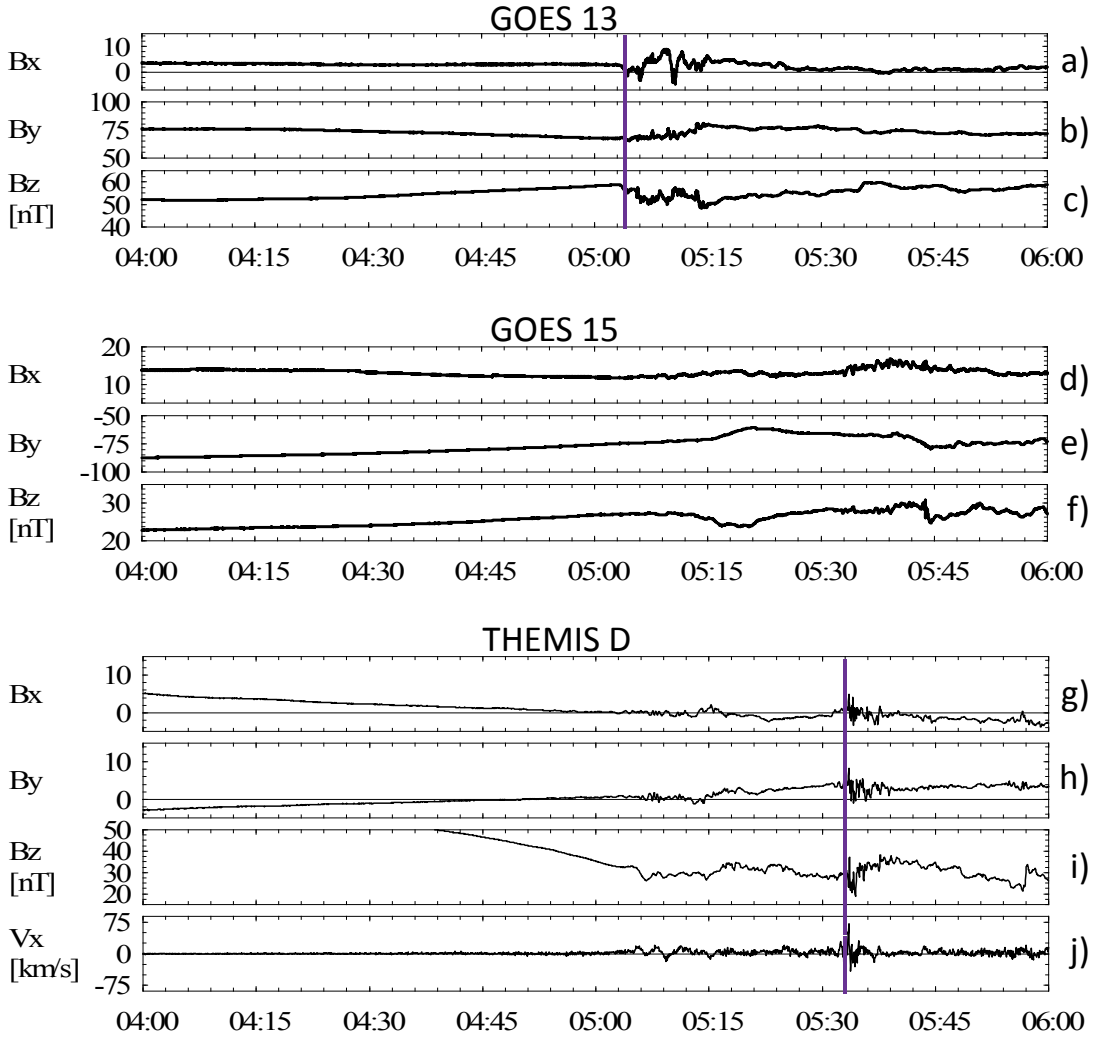

Figure 4.9: The top three panels show GOES 13 magnetic field measurements a) B_x, b) B_y, and c) B_z [nT] GSM. The next three panels show GOES 15 magnetic field measurements, d) B_x, e) B_y, and f) B_z [nT] GSM. The final four panels show THEMIS D observations g) B_x, h) B_y, i) B_z [nT], and j) v_x [km/s]. Purple lines indicate the beginning of the Pi2 period perturbations

flow channel formed in the dawn sector and was observed by THEMIS A which may have contributed to the formation of the substorm current wedge. Additional flow channels also formed in the dusk sector as indicated by THEMIS D observations.

4.2 Simulation Results

Only the LFM model was used for this event because the UCLA model did not handle the event well, possibly due to a combination of the rotation of the minimum variance direction of the solar wind and the dipole tilt. Ionospheric conductances stayed near the minimum allowed in the simulation and and flow channels that developed in the plasma sheet did not penetrate inside of $\sim$8 R_E. In short, a substorm never developed during the simulation interval in the UCLA results. The issue is currently being investigated. The results for this event are available every 10 seconds.

The substorm onset in the LFM simulation results occurred $\sim$13 minutes after the substorm in the observations based on the ionosphere results and the satellite comparisons. Although the timing of onset is off in the simulation, the series of events in the LFM model reproduces the observations reasonably well. Table 4.1 lists the series of events for the substorm in the observations and in the simulation results

In general the plasma sheet results for this event are very similar to the LFM results for the event presented in the previous chapter. Results from the simulated plasma sheet for the interval 0500-0600 UT at 10 minute time steps are shown in Figure 4.10. Figure 4.11 shows the interval 0515-0525 UT at 2 minute time steps in order to show the details of the flow channel most closely related to substorm onset. The simulation shows weak B_z earthward if -20 R_E as early as 0448 UT which generate some small plasma flows in the tail. The early patchy reconnection regions merge to form a cross tail neutral line between -15 and -20 R_E at $\sim$0511 UT. Fast earthward flow channels are generated at several points along this neutral line. The first flow channels to penetrate into the inner edge of the plasma sheet are located in the dawn sector near midnight an 0300 MLT. They are observed at a radial distance of $\sim$-7 R_E at 0515 UT (see Figure 4.11), about 13 minutes later than the onset

Table 4.1: Comparison between observations and simulations results for the interval 0445-0600 UT.

OBSERVATIONS	**LFM**
Flow channel with DF observed by CLUSTER at 0505 UT at ∼2300 MLT	Flow channel with DF forms near 2200 MLT at observation (obs) time +13 min
Flow channel with DF observed by THEMIS A in dawn sector (∼0100 MLT) at 0503 UT	Flow channels with DFs form near 0100 MLT at obs time +11 min
Fluctuations observed by GOES 13 at geosynchronous orbit at 0505 UT	The first flow channels penetrate earthward to -7 R_E in the dawn sector at obs time +10 min
Disturbance observed by THEMIS D in inner magnetosphere at 0533 UT	Several flow channels in both the dusk and dawn sectors travel earthward reaching ∼-7 R_E at obs time -5 minutes
Most perturbations damp out by ∼0600 UT and satellites no longer observe fast flows	Flow channels stop tailward of ∼-13 R_E beginning at ∼0555 UT

of the substorm in the observations. Figure 4.12 shows the same panels as Figure 4.11 but each timestep has the values from the previous timestep subtracted from it so we are looking only at the variations in the plasma sheet magnetic field and velocity. The thermal pressure contours are the same as in the previous plot. DFs in the time differenced plots appear as an enhancement in the perturbation magnetic field followed by a depletion and are indicated by the large blue arrows in each panel. By 0520 UT there are fast flows propagating earthward in both the dawn and dusk sectors. As the pressure and magnetic field builds up in the inner region the flows begin to stop further out in the plasma sheet. By ∼0540 UT the fast flows stop outside of ∼-12 R_E. After 0550 UT no new fast flows penetrate to radial distances less than 15 R_E.

Figure 4.13 shows a) the field aligned currents (FAC), and b) thermal pressure at 5 minute intervals between 0510 and 0525 UT. The FAC for this event are very disordered and no single substorm current wedge can be identified in the top panels of Figure 4.13, rather there are several current wedges across the tail. The FAC associated with the flow channels themselves are the correct sense for the substorm current wedge. To the dusk side of the flow channel there is a downward FAC and to the dawn side of the flow channel there is an

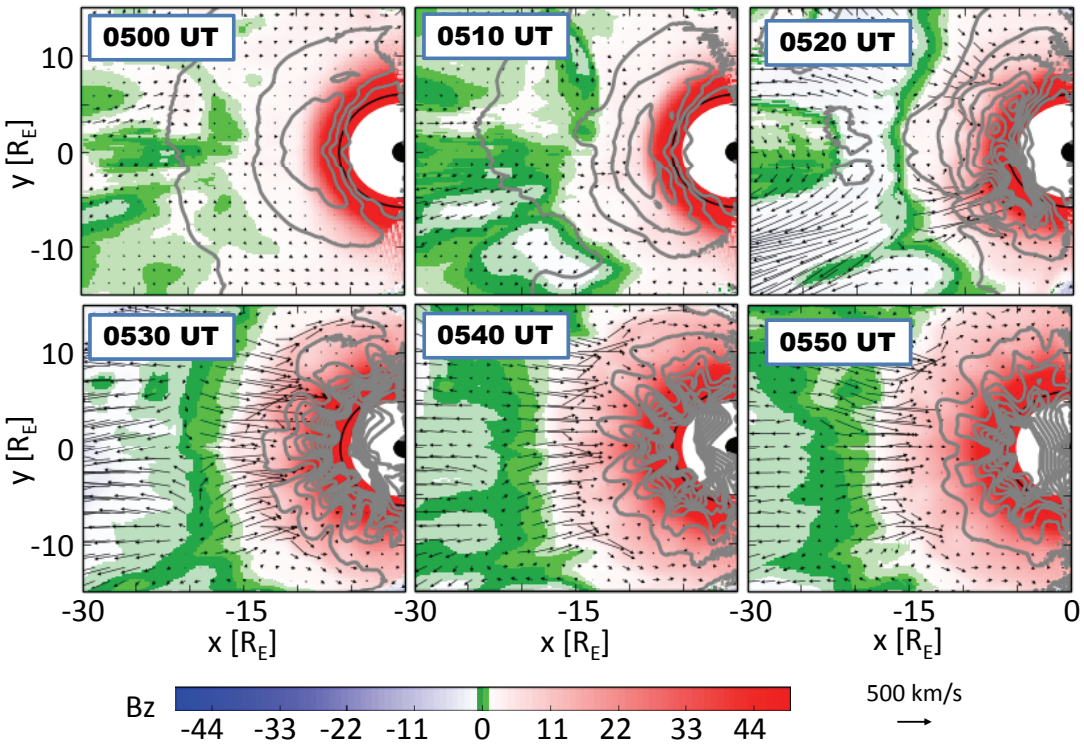

Figure 4.10: Snapshots from the simulated plasmasheet every ten minutes for the interval 0500-0550 UT. The region shown is $-30 < x < 0$ R_E, $-15 < y < 15$ R_E. Background color shows B_z [nT] GSM from -50 nT (blue) to 50 nT (red). The green area indicates where B_z is near 0 nT. Black arrows show the velocity in the plane. A reference vector is shown in the bottom right of the figure. Gray lines show thermal pressure contours between 0 and 1500 pPa, increments are $\delta P = 150$ pPa.

upward FAC. These FACs are enhanced the most at the center of the vortices where the flow velocity is nearly zero. Row c) shows a blow up of the region in the black box in row a) at 0510 and 0515 UT. The regions of upward (into the ionosphere) FAC are indicated by the solid circles with the '+' symbol, while the regions of downward (out of the ionosphere) FAC are indicated by the dashed circles with the '-' symbol. The currents associated with the flow channel relatively well defined at 0510 UT, but, as a result of additional flows entering the region, they become more difficult to identify. In general, the FACs get more and more disordered as the substorm progresses. The regions in the circles in the plot at 0515 UT show the currents from the original flow channel while the additional +/- symbols indicate the upward/downward currents associated with a new flow channel that has entered the region.

As the flow channels travel earthward they increase the thermal pressure in the inner magnetosphere while creating a depression in the thermal pressure in the tail. Both the dawnward and duskward edges of these channels have very steep azimuthal pressure gradients while the earthward edge has a steep radial pressure gradient. Because one of these channels is created by each fast flow that travels earthward, the resulting pressure gradients vary significantly across the night side as can be seen in the lower right panel in Figure 4.13. Although no new flows enter the region between 0550 UT and 0620 UT, these pressure gradients in the LFM results stay very high for extended periods of time, nearly an hour, after the fast flows themselves have dissipated. As the thermal pressure structures dissipate they drift slowly to the flanks. As was shown in Section 3.1 the pressure disturbances in the UCLA model relax much more quickly than those in the LFM results. Although each flow channel creates a disturbance in the thermal pressure, it is unclear how long those perturbations persist. However, there is an overall pressure increase in the inner magnetosphere over the course of the event.

4.2.1 Ionosphere

The results in the ionosphere for this event are shown in Figure 4.14. Columns from left to right show Σ_P, Σ_H and $J_\parallel$. Rows from top to bottom show time steps 0500 UT, 0520

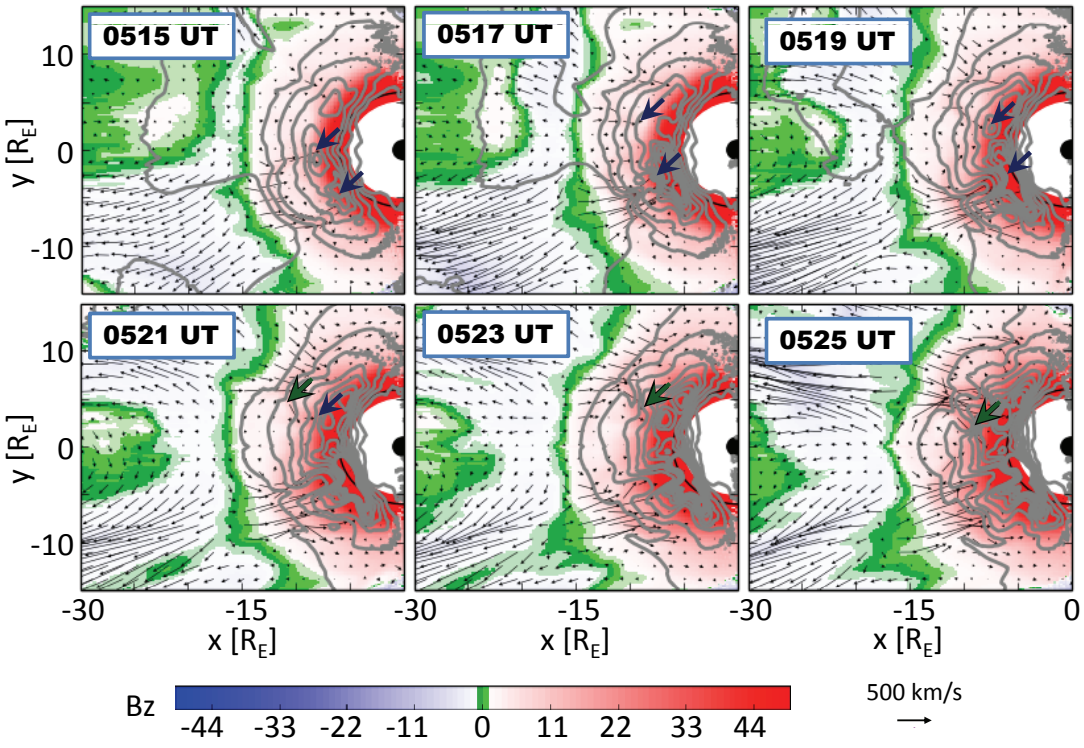

Figure 4.11: Snapshots from the simulated plasmasheet every two minutes for the interval 0515-0525 UT in the same format as Figure 4.10. The thick arrows mark the closest approach of several DFs that propagate earthward during the interval. The first set is indicated by blue arrows and the second set is indicated by green arrows.

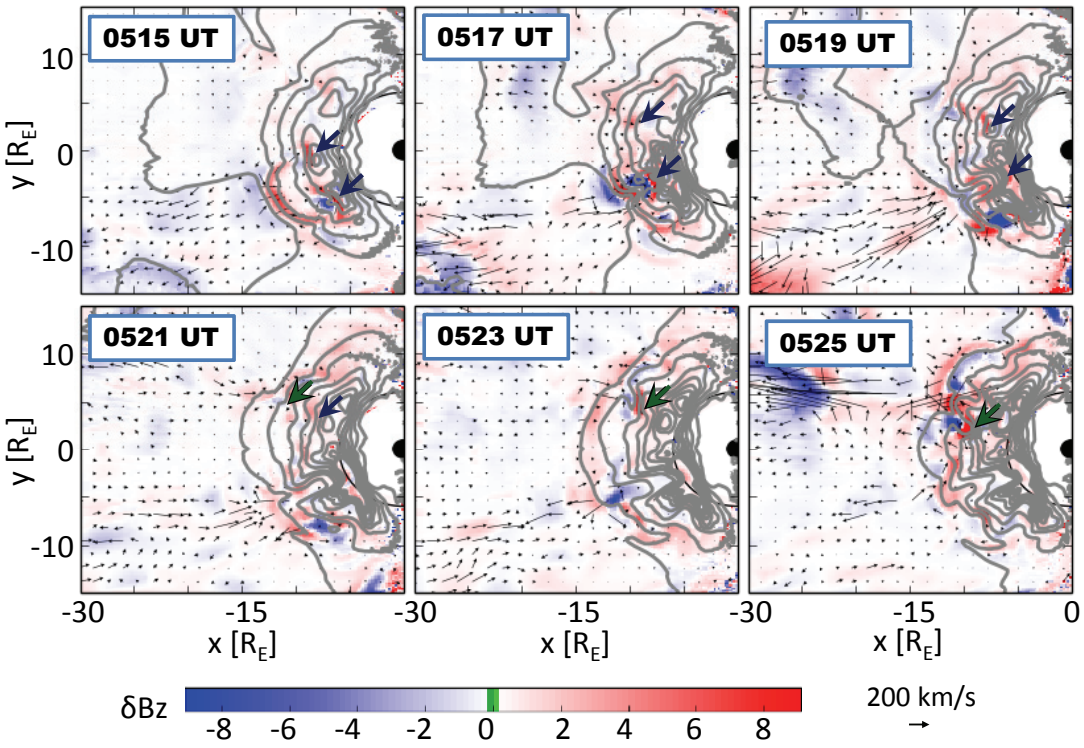

Figure 4.12: Snapshots from the simulated plasmasheet every two minutes for the interval 0515-0525 UT in the same format as Figure 4.11 except the color scale is δB_z -10 to 10 nT.

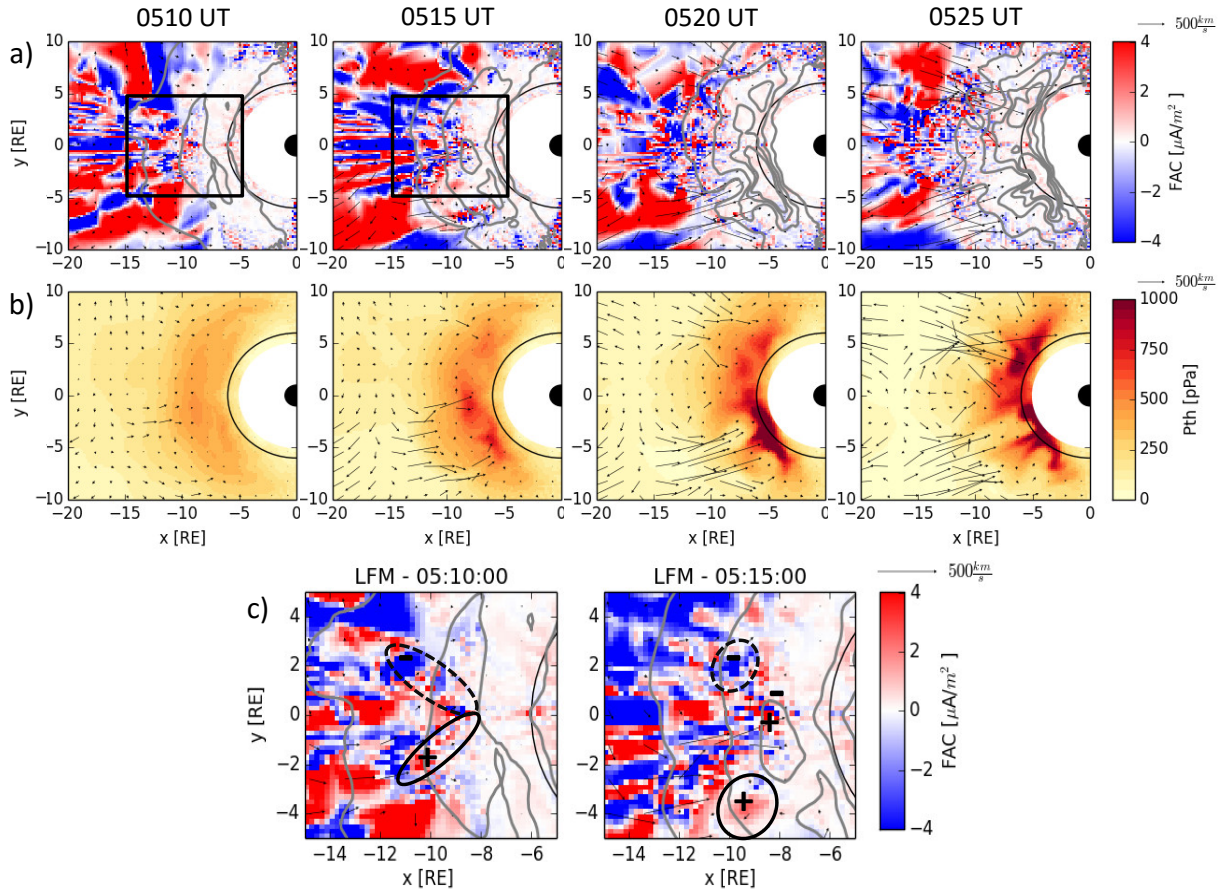

Figure 4.13: Snapshots from the simulated plasmasheet every five minutes for the interval 0510-0525 UT. Row a) shows the field aligned currents [$\mu A/m^2$], row b) shows thermal pressure [pPa] in the region $0 \geq x \geq -20\ R_E$, and row c) shows details from the regions in the black boxes in row a). The solid circles indicate regions of upward (into the ionosphere) FAC while the dashed circles indicate regions of downward (out of the ionosphere) FAC. The additional +/- symbols indicate the currents associated with a new flow channel that has entered the region.

UT, 0540 UT and 0600 UT. Potential contours are plotted over the field aligned currents in Column 3. The results show an increase in the conductances in the auroral region beginning at 0500 UT. This increase corresponds to an increase in the field aligned currents as well as the cross polar cap potential. As was shown in the LFM results in Section 3.2, the conductance results are on the low end of the observed values for active intervals. Enhanced regions of conductance are intermittent across the auroral region because they map to the regions in the tail where flow channels have created a series of depressions in the thermal pressure across the night side near the inner edge of the plasma sheet.

J. Weygand has provided the equivalent ionospheric currents (EICS) and the near field aligned currents for this event, calculated using the available ground observations with the spherical elementary current system (SECS) method *Amm and Viljanen* (1999). The results are show in Figure 4.15. The columns from left to right show the times 0500 UT, 0505 UT (Substorm onset), and 0510 UT. The top row shows the equivalent ionospheric current vectors at each grid point as weather veins with the circle at the base and the line showing the direction and magnitude for the currents. The middle row shows the SECS field aligned currents (FAC) with red as upward currents, and blue as downward currents. The black line in the top and middle rows indicates the location of local midnight. The progression from 0500 to 0510 UT shows the enhancement of the currents at the time of substorm onset as well as the westward progression of the substorm activity. The bottom row shows the field aligned currents from the simulation results. The coloring is the same as in the middle row and the panels have been rotated to line up local midnight. In general, the onset for the substorm is very close to midnight in both the simulation and the SECS results. There is also an increase in the magnitude of the FAC at the time of substorm onset in both. With the exception that the FACs are shifted to higher latitudes in the simulation with the peaks in amplitude near 70° latitude instead of 60° latitude, the simulation has done a reasonable job reproducing the location of the upward and downward field aligned currents obtained using the SECS method.

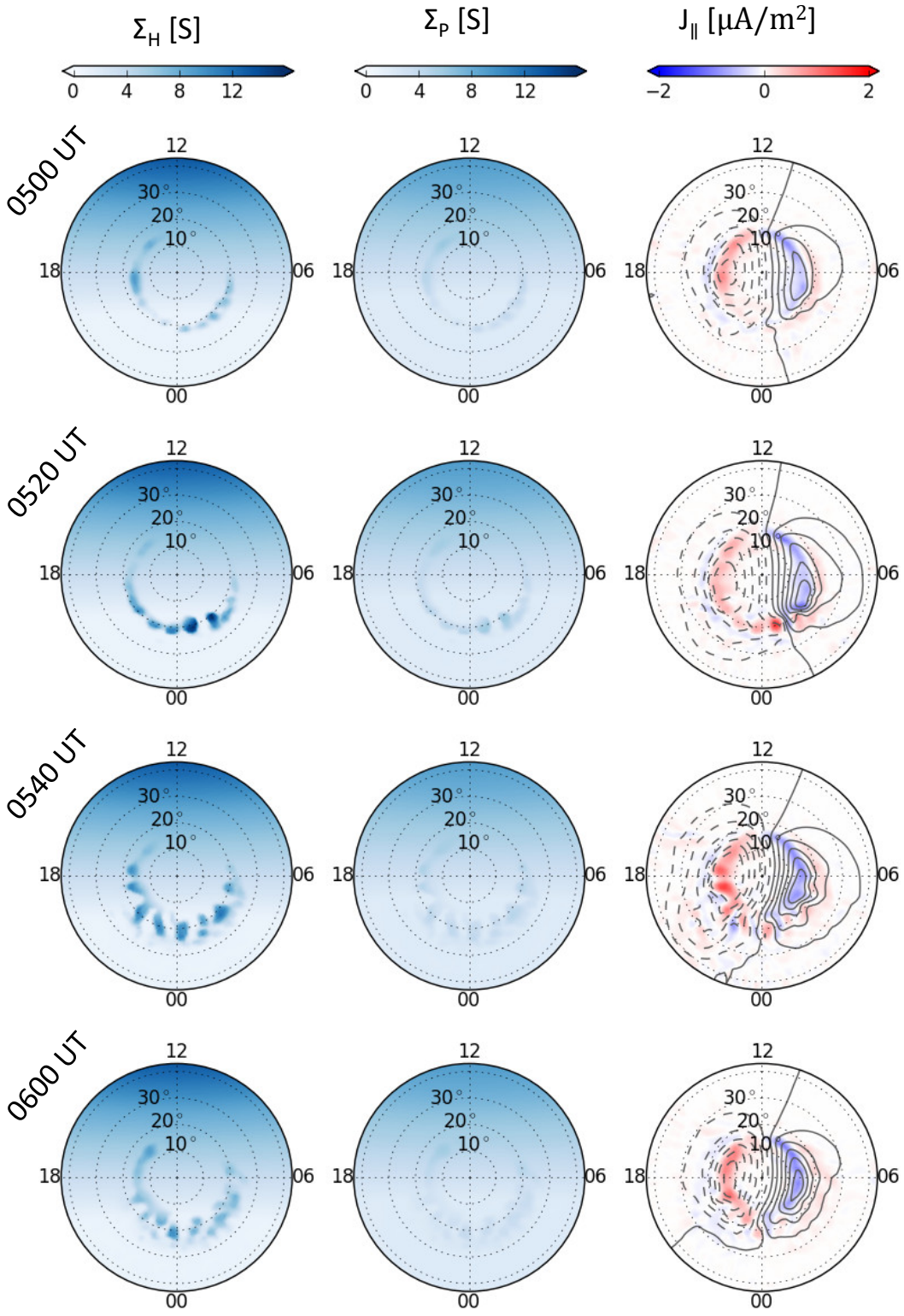
Σ_H [S]
Σ_P [S]
$J_\parallel$ [$\mu A/m^2$]
0 4 8 12
0 4 8 12
−2 0 2
0500 UT
0520 UT
0540 UT
0600 UT
12
30°
20°
10°
18
06
00

4.3 Plasma Sheet Sources for Ionospheric Perturbations

We have looked into the perturbations for this event by investigating the power spectral density (PSD) at each point on the plasma sheet in the region between the reconnection in the tail and the inner edge of the MHD region of the simulation (r=3.7 R_E). The power spectral density is calculated by using the Welch method on 15 minute time series, sampled every 10 seconds, at each point on the plasma sheet. The time series is divided into 10 minute intervals that overlap by 7.5 minutes. A periodogram is computed for each time series using a discrete Fourier transform and taking the squared magnitude of the result. The resulting power spectral density for the time series is the average of the resulting periodograms. PSD plots for B_ϕ (top) and B_θ (bottom) $[nT^2/Hz]$ for the frequency range 10-15 mHz and are shown in Figure 4.16 for the interval 0505-0520 UT, when a flow channel was propagating earthward in the simulated plasma sheet. The region shown is $0 \geq x \geq -20\ R_E$ and $10 \geq y \geq -10\ R_E$. PSD is show in varying shades of green. Units are nT^2/Hz. Because the Pi2 signal is so transient, only a few periods are observed for each Pi2 packet, the PSD analysis was performed by first, subtracting a low order polynomial fit from the time series. The absolute value of the resulting perturbations was taken in order to double the number of periods available for the analysis. As a result the amplitude of the signal was cut in half and the frequency was doubled so the value obtained for the PSD have been corrected in the final step of the analysis. Figure 4.16 shows that there is an enhancement in the PSD at the location of the flow channel for Pi2 frequencies (10-15 mHz). The enhancement forms $\sim$2 R_E from the reconnection site after the DF has developed at the earthward edge of the flow channel. As the flow channel propagates through the braking region and approaches the inner edge of the plasma sheet the enhancement intensifies and spreads in the azimuthal direction. Although the PSD of the shear perturbations is much weaker than that of the compressional perturbations, the azimuthal spreading of the perturbations can be seen in the

Figure 4.14 *(preceding page)*: Columns from left to right show Σ_P, Σ_H and $J_\parallel$. Rows from top to bottom show time steps 0500 UT, 0520 UT, 0540 UT and 0600 UT. Potential contours [kV] ($d\phi$=10 kV) are plotted over the field aligned currents in column 3 with negative contours indicated by dashed lines.

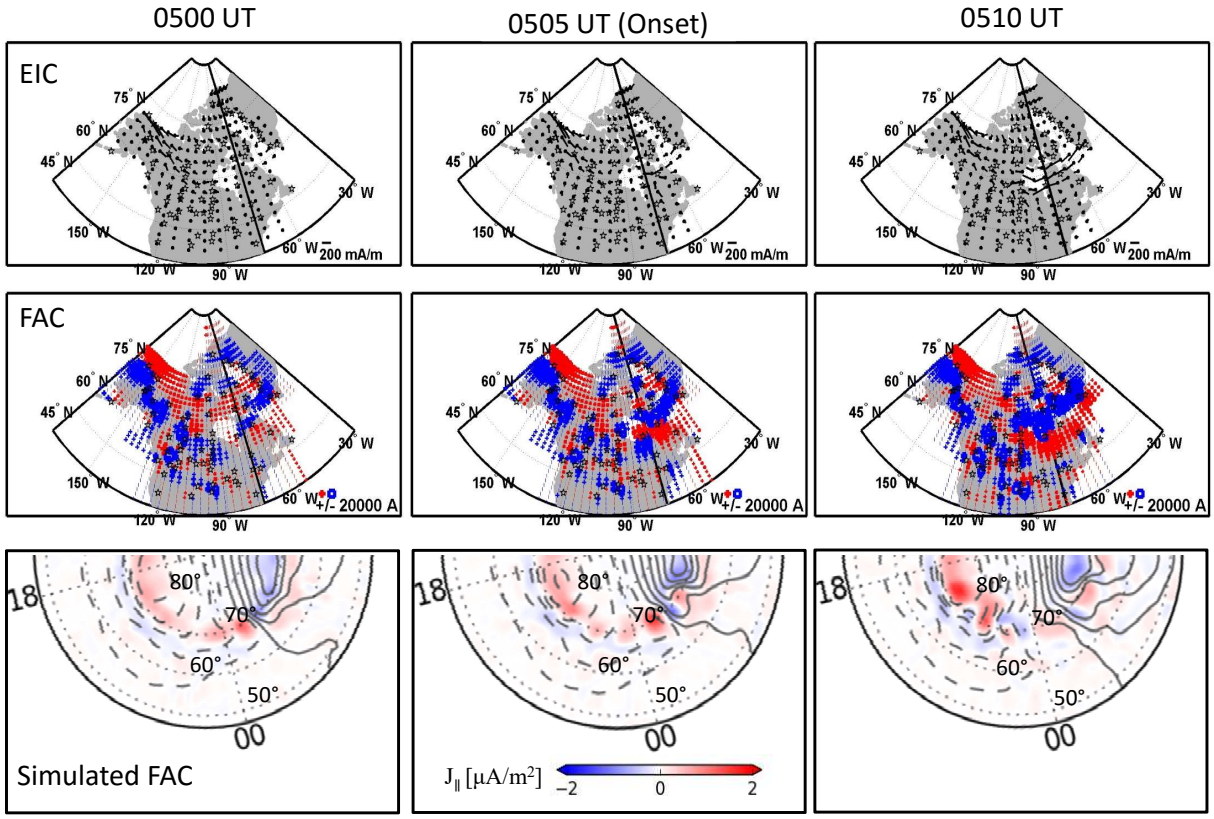

Figure 4.15: Columns from left to right show time steps 0500 UT, 0505 UT (onset time), and 0510 UT. Rows from top to bottom show the equivalent ionospheric currents (EICs), near field aligned currents, and simulated field aligned currents. The EICs are plotted with weather veins, where the dot is at the base and the line indicates the direction and magnitude of the current. Field aligned currents in both the second and third rows show the upward currents as red and the downward currents as blue. Simulated ionosphere results are rotated to match the orientation of rows 1 and 2.

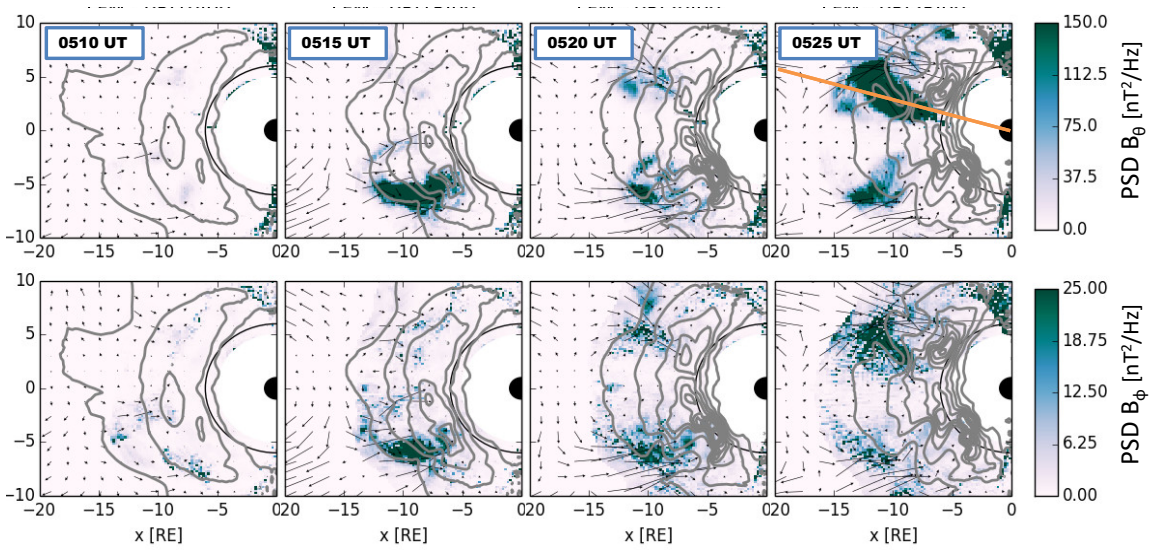

Figure 4.16: PSD plots in the plasma sheet for B_ϕ (top) and B_θ (bottom) $[nT^2/Hz]$ for the frequency range 10-15 mHz for the interval 0505-0520 UT in 5 minute time steps. The region shown is $0 \geq x \geq -20$ R_E and $10 \geq y \geq -10$ R_E. PSD is show in varying shades of green. Thermal pressure contours are shown in gray and the velocity in the plane is indicated by the black arrows. The time stamps indicate the center of the time series used for each plot. Units are nT^2/Hz. The orange line top right panel indicates the location of the meridional cut used in Figure 4.18. Black semi-circle marks the location of $r = 6$ R_E.

PSD for B_ϕ in Figure 4.16 between the third and fourth panels in the bottom row. On the ground, Pi2 signatures are observed at locations distant from substorm onset. The spreading of the Pi2 period pulsations in the braking region can explain how a narrow flow channel is able to create a pulsation over a wide area in the ionosphere and on the ground.

In order to verify that we are looking at Pi2 rather than just a piece of a broadband signature the entire frequency range for a point in the plasma sheet at (-8,4) R_E is shown in Figure 4.17. Panels a-c show the PSD over a range of frequencies from 0.8 to 26 mHz. Panels a and d show B_θ at 0515 UT. Panels b and e show B_θ at 0520 UT and panels c and f show B_ϕ at 0520 UT. The shaded region indicates the Pi2 frequency range. Panels d-f show the PSD in the plasma sheet for the 6-10 mHz bin plotted in the same format as the panels in Figure 4.16. The orange + indicates the point where the power spectra shown in panels a-c was calculated. There is a peak in the PSD at Pi2 frequencies in B_θ at both 0515 and 0520 UT. The double peak in at 0520 UT may be the result of a second flow channel entering the region. There is also a peak in $B\phi$ at 0520 but it is less well defined since B_ϕ

is a minimum on the plasma sheet.

Meridional cuts at the 2245 MLT are shown for the same time steps in Figure 4.18. The location for the meridional cut is indicated by the orange line in Figure 4.16. The figure shows that as the field lines contract the power spectral density enhancement in the shear perturbations, B_ϕ, at Pi2 frequencies increases and spreads along the field lines into the inner region of the magnetosphere at high latitudes ahead of the compressional signal. PSD for B_θ is highest in the plasma sheet but spreads to cover a region of a few R_E in the z direction at times when the flow intensity is the greatest. This B_θ signature shows that the flow channel is generating a compressional wave ahead of it as it propagates earthward through the plasma sheet in agreement with the results presented in Sections 2.4 and 3.3.

This compressional signature propagates as far earthward as $r = 6\ R_E$. In order to investigate the compressional disturbance more accurately we require a simulation that includes physical processes related to the plasmasphere. This is discussed in more detail in Chapter 5.

In order to determine the specific source regions for the pulsations in the ionosphere we have traced field lines from the ionosphere to the plasma sheet. An example of the results from those field line traces is shown in Figure 4.19. The panels show ground-based measurements along with simulated ionospheric quantities at a similar location and mapped quantities in the plasma sheet in the LFM results. Quantities shown are a) the measurements from a ground station, b) simulated ionospheric FAC, c) simulated potential, d) plasma sheet B_z, e) earthward velocity, and f) thermal pressure. In panel a the pulsations in the ionosphere begin the observations at $\sim$0504 UT and continue for approximately 15 minutes. Panels b and c show the FAC and potential, respectively, from the simulated ionosphere at a location near the observations. The perturbations in the FAC are very similar to the Pi2 pulsations observed by the ground station given the 13 minute time shift for substorm onset. The perturbations in the FAC reach their maximum amplitude about 1 minute after the initial disturbance is observed in the plasma sheet. There is also a decrease in the potential just before the pulsations begin in the FAC. In the plasma sheet (Panels d, e, and f) we can see that there is an increase on the earthward velocity and thermal pressure associated with

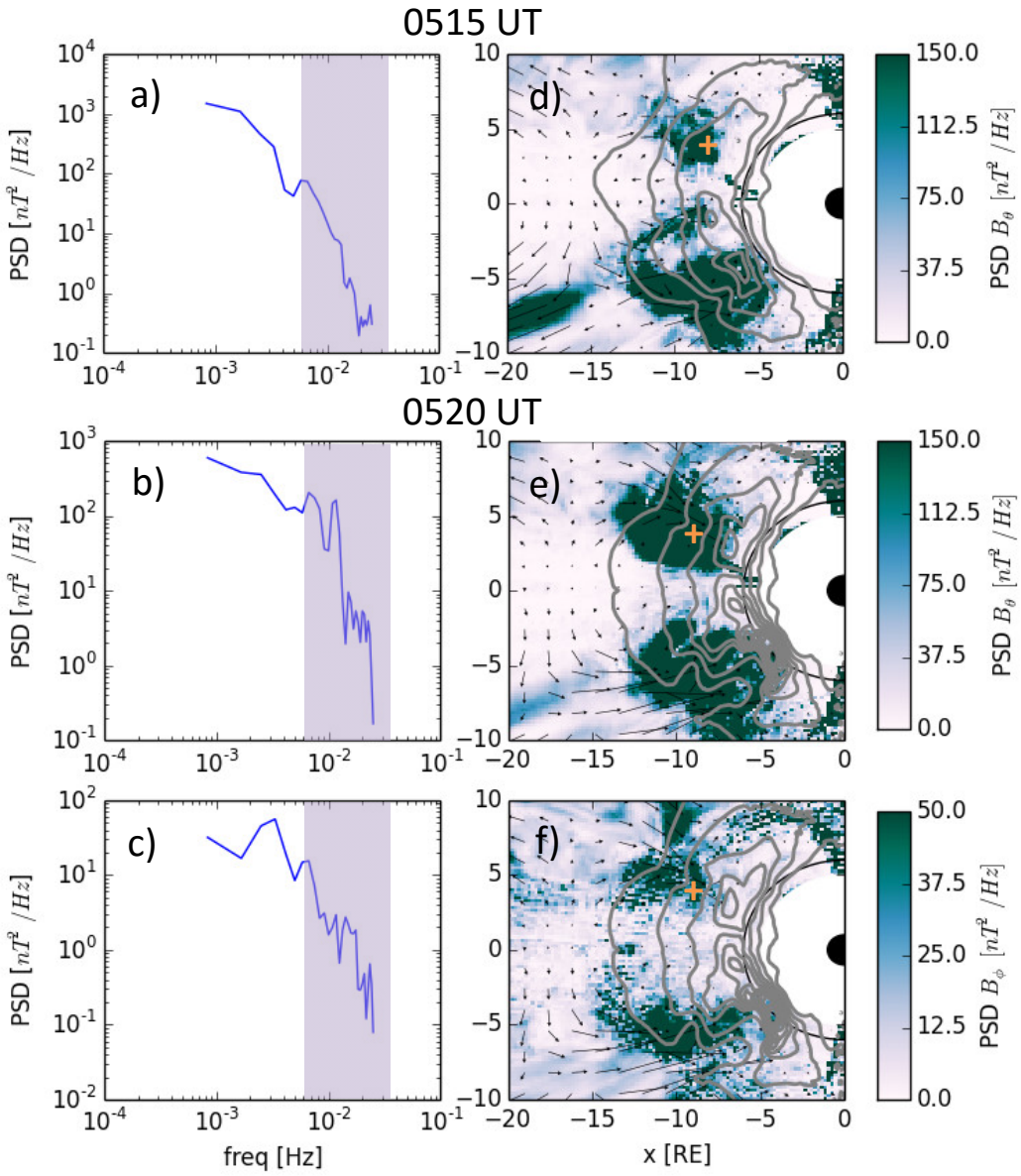

Figure 4.17: PSD at (-8,4) R_E in the plasma sheet. The panels show a) PDS for B_θ at 0515 UT, b) PDS for B_θ at 0520 UT, and c) PDS for B_ϕ at 0520 UT. Panels d, e, and f show the PSD in the plasma sheet in the same format as the panels in Figure 4.16 with the orange + marking the position for the power spectra shown in panels a, b, and c respectively. Shaded regions in panels a-c indicate the Pi2 frequency range.

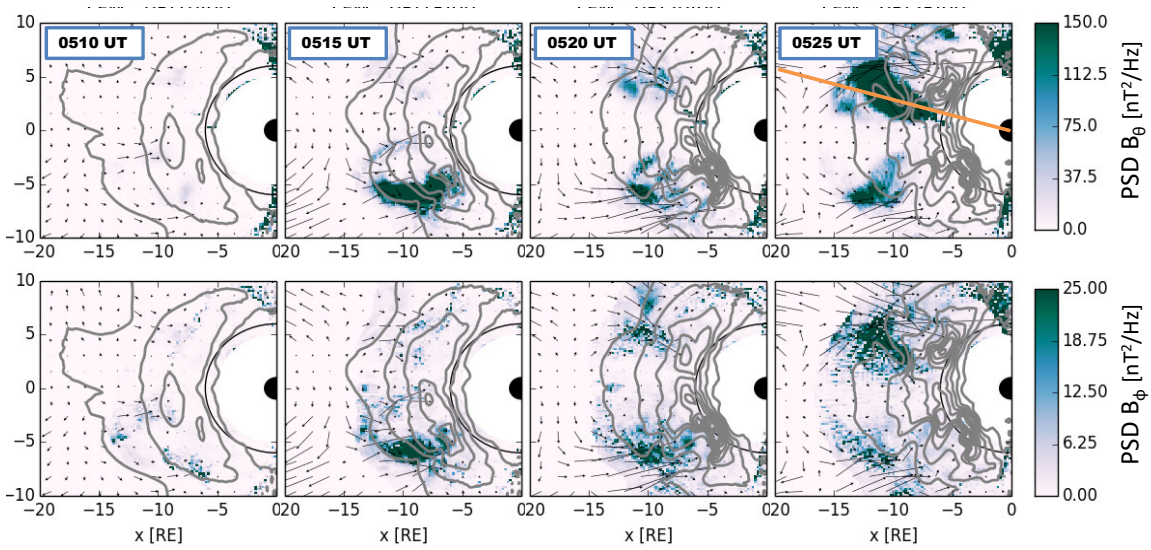

Figure 4.18: PSD plots in the 2245 MLT meridian, indicated by the orange line in Figure 4.16, for B_ϕ (top) and B_θ (bottom) for the frequency range 10-15 mHz for the interval 0505-0520 UT in 5 minute time steps. The region shown is $0 \geq x \geq -20$ R_E and $10 \geq z \geq -10$ R_E. PSD is show in varying shades of green. Thermal pressure lines (gray) are included as a reference. The time stamps indicate the center of the time series used for each plot. Units are nT^2/Hz. Black semi-circle marks the location of $r = 6$ R_E.

most of the pulsations in the ionosphere.

When we look at two traces from the same longitudinal bin we can get an idea of how the perturbation propagates earthward. Figure 4.20 shows time series for two field lines located at 153° at the time of substorm onset. The left plots are for the field line that intersects the ionosphere at 68° latitude. The right panels are for the field line that intersects the ionosphere at 71° latitude. From top to bottom the first three panels show the a) FAC, b) potential, and c) conductances in the simulated ionosphere. The next two panels show the d) magnetic field and e) the thermal pressure at the inner edge of the MHD region in the simulation (∼2.7 R_E). The final three panels show the f) magnetic field, g) velocity and h) thermal pressure at the point where the field line crosses the plasma sheet. For the field line at 71° mLat there is an impulsive increase in the velocity in the plasma sheet at 0525 UT accompanied by an increase in the thermal pressure marked by the cyan dashed line at 0524 UT. There is a nearly simultaneous increase in the thermal pressure and magnetic field at the inner edge of the MHD (panels d and e). Note that just prior to this the field line

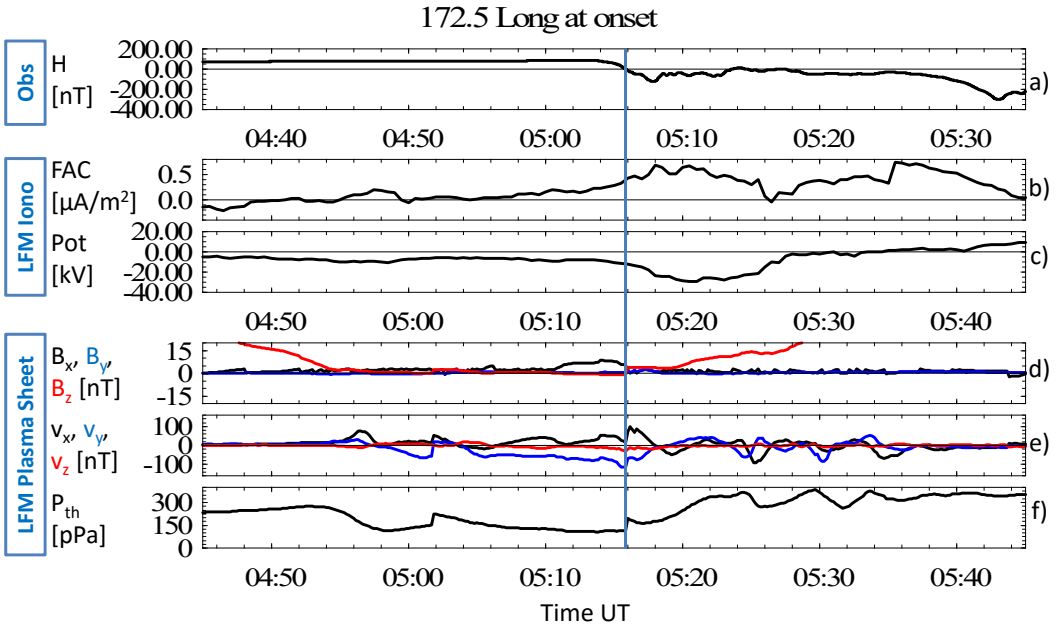

Figure 4.19: A time series of parameters evaluated where a selected field line intersects the ionosphere and crosses the plasma sheet plotted with ground based observations for a station at a similar location. Panels show a) B_H $[nT]$ measurements from a ground station (Fort Churchill - FCC), b) simulated ionospheric FAC $[\mu A/m^2]$, c) simulated potential $[kV]$, d) plasma sheet B_x (black), B_y (red), and B_z (green) $[nT]$, e) plasma sheet velocity v_x (black), v_y (red), and v_z (green) $[km/s]$, and f) thermal pressure $[pPa]$. A 13 minute time shift has been applied to the LFM results. The blue line indicates the time when a flow channel is observed in the simulated plasma sheet.

was open indicated by the shaded region in the figure. Additionally, there are no Pi2 period fluctuations in the ionosphere until 0531 UT. At 0531 UT there is a second enhancement in the plasma sheet pressure with associated fluctuations in the pressure at 3 R_E and Pi2 period fluctuations in the ionospheric FAC. However there is no flow enhancement associated with these fluctuations.

The field line that intersects the ionosphere at 68° mLat also shows enhancements in the plasma sheet thermal pressure associated with fast flows in the plasma sheet. For the disturbance at 0518 UT (black dashed line) there is a steady increase in the thermal pressure at 3 R_E but there are no Pi2 period fluctuations in the ionosphere. However, there are for the second increase in the 68° panel (cyan dashed line) at 0524 UT. This event shows a fast flow in the plasma sheet, a pressure disturbance at 3 R_E, and Pi2 period perturbations in the ionospheric FAC. Similar signatures can be seen at 71° mLat for this event starting at the cyan dashed line in the left panel. In total three disturbances are shown in the figure. The cyan dashed lines in the two panels show the same disturbance. Two of these three disturbances, marked by the black and cyan lines, have fast earthward flows associated directly with them. The other disturbance (magenta dashed line) shows a thermal pressure increase in the plasma sheet but no fast flow is observed in the plasma sheet. Based on the simulation results, the thermal pressure disturbance would have resulted from the passage of a fast flow near the location where the field line intersects the plasma sheet. Although we do not observe the fast flow itself, the pressure disturbance still generated a pulse that propagated along the field lines into the ionosphere.

4.4 Pi2 Model based on Global MHD Simulations

Based on the results presented here and in Chapters 2 and 3 we have determined that Pi2 are being generated as a direct effect of the flow channels that form in the simulations. In Figures 4.16 and 4.18, as well as Section 2.3, perturbations form in the simulations as the flow channels travel earthward. Once the flow channels reach ∼-12 R_E the frequency of the perturbations falls within the Pi2 range. The shear perturbations take ∼30 seconds to

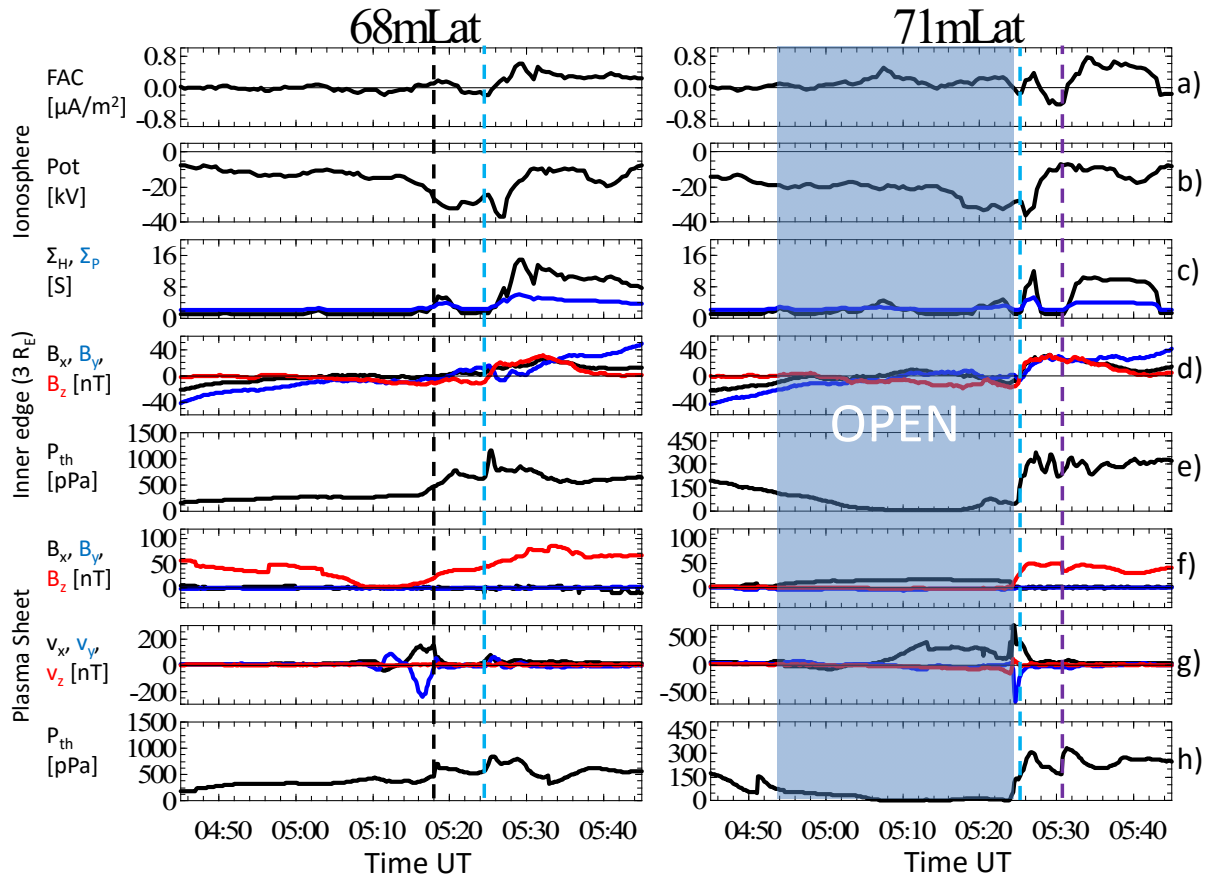

Figure 4.20: Time series in the ionosphere, at the inner edge of the MHD region of the simulation and at the plasma sheet intersection for field line traces from two ionospheric locations, 68° mLat and 71° mLat, located in the 2230 MLT meridian. From top to bottom the panels show a) ionospheric FAC [$\mu A/m^2$], b) ionospheric potential [mV], c) Σ_H (black) and Σ_P (red) [S] d) B_x (black), B_y (red), and B_z (green) [nT] at $r = 3\ R_E$, e) thermal pressure [pPa] at $r = 3\ R_E$, f) plasma sheet B_x (black), B_y (red), and B_z (green) [nT], g) v_x (black), v_y (red), and v_z (green) [km/s], h) plasma sheet thermal pressure [pPa]. Dashed lines mark the beginning of thermal pressure disturbances in the plasma sheet. The shaded region indicates an interval when the field line was open.

travel along the field lines reaching the inner magnetosphere at high latitudes ahead of the compressional perturbations (see Figure 4.18). These results are in good agreement with the transient response model for Pi2 generation (*Southwood and Stuart*, 1980).

In addition Figures 4.16 and 4.18 also show that the Pi2 period perturbations present in the simulations propagate along the field lines into the inner magnetosphere at high latitudes and spread azimuthally as the flow channels are slowed in the braking region. This property of the dynamics of the perturbation in the magnetosphere agrees well with observations of Pi2. In the Figures 4.4 and 4.5 it is evident that the pulsations are observed over a wide area on the ground. This wide spatial range for observations is typical for Pi2 pulsations.

In Figure 4.18 the fluctuations develop in the plasma sheet around 0520 UT with the arrival of the flow channel near $\sim$-12 R_E rather than at the inner edge of the plasmasheet where we see the transition from stretched to dipolar field line configurations. The perturbations intensify and move earthward as the flows continue to propagate and as stronger flows enter the region. If additional Pi2 period perturbations are being generated as a result of the ballooning mode at the inner edge of the plasma sheet as suggested by *Keiling et al.* (2008), they are dwarfed by the perturbations generated by the fast flow channels. However, the pressure contours are so distorted in the region $-10 \leq x \leq -3$ that there is not one clear region through the interval where the magnetic field and pressure gradients both point earthward. With so much variation in the thermal pressure and the magnetic field in near the inner edge of the plasma sheet it is difficult to identify any given region where the ballooning instability could develop and drift in order to generate a Pi2 signature on the ground.

In addition, the results from the field line tracing shows that not every disturbance in the ionosphere maps to a fast flow in the tail. However, all of the ionospheric fluctuations map to thermal pressure disturbances in the tail. When a fast flow passes through an area it creates a pressure disturbance in the surrounding area, the fast flows are indirectly responsible for generating the disturbances observed in the inner magnetosphere and on the ground even if the disturbance does not map to the flow channel itself.

For mid- to low-latitude Pi2 we have shown in Chapter 3 that as the flow channels enter the braking region and begin to slow, a mixed mode compressional wave is generated that begins to travel ahead of the DF signature into the inner magnetosphere. The period of these waves are directly related to the period of the fluctuations contained within the flow channel as it slows in the braking region. These results agree well with the directly driven mechanism for Pi2 (*Kepko and Kivelson*, 1999; *Kepko et al.*, 2001) with the subtle difference that the period is the result of fluctuations contained within one flow channel rather than the result of several consecutive flow channels. In order to investigate how the compressional disturbance travels through the inner magnetosphere we require a model that includes the physics of the plasmasphere. This is discussed more in the next chapter.

4.5 Summary

We have used a case study of a substorm event on August 25, 2013 to investigate the plasma sheet source for Pi2 period perturbations in the LFM global MHD model. Analysis of the Pi2 period pulsations present in the plasma sheet and the ionosphere indicates that the Pi2 pulsations on the ground are driven by fluctuations in the magnetic field and thermal pressure associated with fast earthward flows in the simulated plasma sheet. The PSD analysis shows that, not only does the wave power for Pi2 frequencies increase when a flow channel is present, but that as the flow channel slows in the breaking region it spreads azimuthally so the pulsations generated by a very narrow flow channel would be observed over a wide area on the ground.

The results from a power spectral density analysis confirm that the Pi2 period perturbations are generated by the flow channels as they travel earthward. The perturbations are within the Pi2 range inside of $\sim$-12 R_E. Pi2 period perturbations are generated in both B_θ and B_ϕ as the fast flows travel earthward. The compressional perturbations are mostly confined near the plasma sheet while the shear perturbations spread quickly along the field lines into the inner magnetosphere at high latitudes.

CHAPTER 5

Summary and Future Work

5.1 Summary of Results for Pi2 Generation in MHD Simulations

Understanding how and where Pi2 pulsations are generated and how they propagate through the magnetosphere is an important part of understanding substorms. This is especially true since the onset of Pi2 pulsations observed by ground-based magnetometers is used to determine the timing of substorm onset. There are several models for Pi2 generation that have been developed based on ground-based and satellite observations of Pi2 period fluctuations. We have approached the problem using global MHD simulations in order to get a more global picture of the magnetotail to identify the Pi2 driver.

In Chapter 2 we analyze a UCLA global MHD simulation of a substorm on September 14, 2004 in order to determine whether or not MHD simulations are able to reproduce Pi2 period pulsations observed in the plasma sheet. The results show that the flow channels generate perturbations in the magnetic field as they propagate earthward. Those perturbations are within the Pi2 range once the flow channel is earthward of $\sim$-12 R_E. The DFs in the simulation prior to the time of substorm onset all stop tailward of -7.5 R_E without causing serious disruption to the braking region, and the magnetic field perturbations associated with them are quickly damped. The flow channel at the time of substorm onset is the first to penetrate earthward of -7.5 R_E. The fluctuations inside the braking region appear to be driven by perturbations in total pressure, B_R, v_{pa} and v_x associated with the BBFs even though the B_z signatures dissipate tailward of the braking region.

In order to determine whether the perturbations are generated as a result of the physics included in the models rather than the specific numerical methods used to solve the set of

equations, we simulate the September 14, 2004 event using a second global MHD simulation and compare the results in Chapter 3. When comparing results from the UCLA and Lyon-Fedder-Mobarry (LFM) global simulations we determine that Pi2 period perturbations are generated in the same way in both simulations indicating that they are a result of the physics included in the models rather than the initial set-up or the numerical methods used in the individual simulations. When we focus on the flow channel that forms around the time of substorm onset in the simulations, we observe Pi2 period perturbations inside ∼-12 R_E in the magnetic field, velocity and pressure propagating at the earthward edge of the fast flow in agreement with the Transient Response model for Pi2 *Southwood and Stuart* (1980); *Kepko et al.* (2001). We also observe Pi2 period perturbations in B_y as a result of the vortices that form on either side of the flow channel in support of the Inertial Current component of the bursty flow model. As the DF is slowed in the braking region as it approaches the inner edge of the plasma sheet the perturbations begin to travel ahead of it as a mixed mode compressional wave. These propagating compressional waves generated by the fast flows in the braking region can produce Pi2 pulsations observed on the ground as described by the directly driven model for Pi2 generation (*Kepko and Kivelson*, 1999; *Kepko et al.*, 2001, 2004). A subtle difference between the bursty flow model and the MHD results is that the Pi2 pulsations are generated by the fluctuations within a single flow channel, rather than successive flow channels, arriving at the inner edge of the plasma sheet.

When comparing the results from the two models we determine that the propagation of the perturbations into the inner magnetosphere is greatly affected by the differences in the ionospheric models in the simulations. In the UCLA results, the high Pedersen conductance (∼25 S) causes the flow channels and the perturbations to stop propagating earthward at ∼7 R_E. In the LFM results, on the other hand, the relatively low Pedersen conductance (∼9 S), flows are able to propagate much more easily into the inner magnetosphere.

When investigating power spectral density of the perturbations generated by flow channels in a more isolated substorm on August 25, 2013, we find that, not only does the wave power for Pi2 frequencies increase when a flow channel is present, but that as the flow channel slows in the breaking region it spreads azimuthally so the pulsations generated by a

very narrow flow channel would be observed over a wide area on the ground. By tracing field lines from several locations in the ionosphere to the plasma sheet we are able to show that, although not all ionospheric perturbations map to a fast flow channel, they all map to a disturbance in the thermal pressure. Since the thermal pressure disturbance is a result of the passage of a fast flow the flow channels are at least indirectly responsible for the perturbations observed in the ionosphere.

5.2 Future Work

In order to advance the investigation of Pi2 pulsations using MHD simulations we plan to use the Lyon-Fedder-Mobarry (LFM) 3D global magnetohydrodynamic (MHD) model (*Lyon et al.*, 2004) with the MIX ionosphere model (*Merkin and Lyon*, 2010), coupled to the Rice Convection Model (RCM) (*Harel et al.*, 1981; *Toffoletto et al.*, 2003) to investigate the generation and propagation of Pi2 period fluctuations through the plasma sheet and inner magnetosphere. The coupled models give a much more physical representation of the inner magnetosphere than the version of the model used in this thesis.

In the current work we have focused on the generation of Pi2 pulsations in the magnetotail. By using the LFM-MIX-RCM model we will be able to expand that investigation to test Pi2 models focusing on the role of the inner magnetosphere on Pi2 generation and propagation. Focus will be placed on understanding how the perturbations generated by fast plasma flows in the tail propagate through the boundaries at the inner edge of the plasma sheet and the plasmapause. I will also investigate the drivers for different Pi2 signatures observed at mid- and high latitudes by mapping from virtual ground observatories into the magnetotail and inner magnetosphere.

As described in Chapter 1, in addition to the models for Pi2 generation in the tail, there are also several models describing how the fluctuations propagate once they are in the inner magnetosphere. These models look at plasmasphere cavity modes, plasmapause surface waves, and field line resonances as sources for the pulsations observed on the ground. One model typical of the inner magnetosphere is the Plasmaspheric Virtual Resonance (PVR)

model which states that a broadband compressional wave travels earthward from the inner edge of the plasma sheet and excites a fast mode wave that is trapped in the plasmasphere with the ionosphere and plasmapause acting as nearly perfect reflectors at the inner and outer boundaries (*Lee and Lysak*, 1999). Each of the inner magnetosphere models for Pi2 generation require that a disturbance, presumably from the tail, must impact the inner edge of the plasma sheet to generate the broadband compressional pulse that travels earthward through the inner magnetosphere. We have identified Pi2 period perturbations in the fast flow channels but several questions remain. Specifically, how do the perturbations propagate through the inner magnetosphere and what are the affects of the plasmapause and plasmasphere on the perturbations?

Each of the Pi2 models tries to describe how the Pi2 signatures observed at different latitudes are generated. At high latitudes, the Pi2 signature is disordered and contains several spectral peaks (*Samson*, 1982). The signatures at mid-latitudes are more sinusoidal and have smaller amplitude than the high latitude pulsations. Additionally, the pulsations at high-latitudes appear to be associated directly with the substorm current wedge (SCW) (*McPherron*, 1972; *Singer et al.*, 1983), whereas the mid-latitude pulsations occur over most of the nightside (*Yeoman et al.*, 1994). Most likely, several of the mechanisms described in the existing models are acting together to produce the Pi2 signatures observed by ground-based magnetometers.

In the previous global MHD simulation studies of Pi2 propagation, the models were limited by the fact that they did not include the physics of the inner magnetosphere, namely the plasmasphere and ring currents. As a result the simulations were not able to accurately model the propagation of the pulsations inside $\sim 6R_E$.

Recent success coupling the LFM MHD model to the Rice Convection Model (RCM) has made it possible to more accurately model the magnetosphere to much smaller radial distances by including the plasma species necessary to incorporate the physics of the inner magnetosphere (*Pembroke et al.*, 2012). These advances along with improved resolution in the LFM MHD model have made it possible to study the propagation of ultra-low frequency waves through the inner magnetosphere in a 3D global MHD simulation that includes a

plasmasphere (*Claudepierre et al.*, 2013).

I propose to use the high resolution integrated Lyon-Fedder-Mobarry (LFM), Rice Convection Model (RCM), and MIX ionosphere model (LFM-RCM-MIX) driven with an ideal solar wind to investigate the propagation of the Pi2 pulsations generated in the tail, through the boundaries at the inner edge of the plasma sheet and the plasmapause. Using the coupled model with an included plasmasphere will allow me to address several unanswered questions concerning Pi2 generation and propagation.

By tracing the disturbances generated by individual flow channels through the braking region and into the inner magnetosphere, I will investigate the interaction between the perturbations and the plasmasphere. To do this I will identify the center of individual flow channels that propagate earthward far enough to disturb the inner edge of the plasma sheet. After identifying the location of the inner magnetosphere disturbance in local time, I will be able to take local time cuts from the simulation and look at the power spectral density for Pi2 period fluctuations during the interval directly following the flow channel impact. This will be done in a manner similar to the work presented by *Claudepierre et al.* (2010) investigating perturbations generated in the dayside magnetosphere by fluctuations in the solar wind dynamic pressure. The main focus of this portion of the study will be to identify the wave modes in the plasmasphere that are generated by the compressional wave traveling earthward from the inner edge of the plasma sheet. I will also look at the frequencies associated with the compressional wave and the waves in the plasmasphere to determine where the fluctuations get their characteristic Pi2 period. This will help me to determine which of the mechanisms outlined in the models listed in Table 1.2 is the dominant contributer to the generation of the Pi2 pulsations observed on the ground.

The capability to map from virtual ground stations into the inner magnetosphere and the plasmasheet will allow me to investigate the drivers for Pi2 pulsations observed at mid- to high latitudes. The goal of this portion of the investigation will be to isolate the different mechanisms responsible for generating the disordered Pi2 signatures at high latitudes versus the more sinusoidal Pi2 signatures observed at mid-latitudes. By mapping along field lines from virtual stations at a range of different latitudes, I will be able to determine what region

the pulsations map to in the magnetosphere (plasma sheet, substorm current wedge, inner edge of the plasma sheet, plasmapause, plasmasphere, etc.) and identify the perturbations in that region which couple to the shear mode, and propagate into the ionosphere. I will also investigate the coupling mechanism between the compressional waves generated by the flow channels and the shear waves in the regions identified as source regions for Pi2 generation via field line mapping.

5.3 Future Work Summary

Due to the direct relationship between Pi2 pulsations and substorm onset, understanding how and where the pulsations are generated is very important for understanding the series of events leading up to substorm onset and has the potential to improve our ability to predict when and where a substorm will take place. The question of Pi2 generation has been addressed in several models, outlined in Table 1.2. However, each of the existing Pi2 models have been put together using observations alone. Since the spatial resolution of observations is often very low, especially in the nightside magnetosphere, there are several assumptions that have to be made concerning what is happening in the space between satellites.

In the future we hope to look at the question of Pi2 generation using a coupled 3D global MHD model in order to fill in some of those gaps and get a more thorough picture of what is happening in the tail leading up to Pi2/substorm onset on the ground. *Ream et al.* (2013) have shown that an earthward propagating compressional wave is excited, with a period in the Pi2 range, by fast flows in a global MHD simulation as the flows slow in the braking region. Using the integrated LFM-RCM-MIX model I will be able to extend this analysis into the inner magnetosphere to investigate how the compressional perturbation generated at the inner edge of the plasma sheet travels earthward and interacts with the plasmasphere/plasmapause. This, in addition to the ability to map from virtual stations on the ground into the magnetosphere, will allow me to determine where the Pi2 pulsations observed on the ground at different latitudes are generated in the plasma sheet and inner magnetosphere. It will allow me to determine which of the mechanisms described in the

existing Pi2 models is dominant in producing the different ground Pi2 signatures observed at high latitudes versus mid-latitudes.

Bibliography

Akasofu, S.-I. (1964), The development of the auroral substorm, *Planetary and Space Science*, *12*, 273–282, doi:10.1016/0032-0633(64)90151-5.

Alfvén, H. (1942), Existence of Electromagnetic-Hydrodynamic Waves, *Nature*, *150*, 405–406, doi:10.1038/150405d0.

Amm, O., and A. Viljanen (1999), Ionospheric disturbance magnetic field continuation from the ground to the ionosphere using spherical elementary current systems, *Earth, Planets, and Space*, *51*, 431.

Angelopoulos, V., W. Baumjohann, C. F. Kennel, F. V. Coronti, M. G. Kivelson, R. Pellat, R. J. Walker, H. Luehr, and G. Paschmann (1992), Bursty bulk flows in the inner central plasma sheet, *Journal of Geophysical Research*, *97*, 4027–4039, doi:10.1029/91JA02701.

Angelopoulos, V., C. F. Kennel, F. V. Coroniti, R. Pellat, M. G. Kivelson, R. J. Walker, C. T. Russell, W. Baumjohann, W. C. Feldman, and J. T. Gosling (1994), Statistical characteristics of bursty bulk flow events, *Journal of Geophysical Research*, *992*, 21,257–+, doi:10.1029/94JA01263.

Angelopoulos, V., J. P. McFadden, D. Larson, C. W. Carlson, S. B. Mende, H. Frey, T. Phan, D. G. Sibeck, K.-H. Glassmeier, U. Auster, E. Donovan, I. R. Mann, I. J. Rae, C. T. Russell, A. Runov, X.-Z. Zhou, and L. Kepko (2008), Tail Reconnection Triggering Substorm Onset, *Science*, *321*, 931–, doi:10.1126/science.1160495.

Ashour-Abdalla, M., M. El-Alaoui, F. V. Coroniti, R. J. Walker, and V. Peroomian (2002), A new convection state at substorm onset: Results from an MHD study, *Geophys. Res. Let.*, *29*(20), 1965, doi:10.1029/2002GL015787.

Ashour-Abdalla, M., J.-M. Bosqued, M. El-Alaoui, V. Peroomian, M. Zhou, R. Richard, R. Walker, A. Runov, and V. Angelopoulos (2009), A simulation study of particle energization observed by THEMIS spacecraft during a substorm, *Journal of Geophysical Research (Space Physics)*, *114*(A13), A09204, doi:10.1029/2009JA014126.

Ashour-Abdalla, M., M. El-Alaoui, M. L. Goldstein, M. Zhou, D. Schriver, R. Richard, R. Walker, M. G. Kivelson, and K.-J. Hwang (2011), Observations and simulations of non-local acceleration of electrons in magnetotail magnetic reconnection events, *Nature Physics*, *7*, 360–365, doi:10.1038/nphys1903.

Baker, D. N., T. I. Pulkkinen, V. Angelopoulos, W. Baumjohann, and R. L. McPherron (1996), Neutral line model of substorms: Past results and present view, *Journal of Geophysical Research*, *101*, 12,975–13,010, doi:10.1029/95JA03753.

Baumjohann, W., R. A. Treumann, J. Labelle, and R. R. Anderson (1989), Average electric wave spectra across the plasma sheet and their relation to ion bulk speed, *Journal of Geophysical Research*, *94*, 15,221–15,230, doi:10.1029/JA094iA11p15221.

Birn, J., R. Nakamura, E. V. Panov, and M. Hesse (2011), Bursty bulk flows and dipolarization in MHD simulations of magnetotail reconnection, *Journal of Geophysical Research (Space Physics)*, *116*(A15), A01210, doi:10.1029/2010JA016083.

Cao, X., Z. Y. Pu, H. Zhang, V. M. Mishin, Z. W. Ma, M. W. Dunlop, S. Y. Fu, L. Xie, C. J. Xiao, X. G. Wang, Q. G. Zong, Z. X. Liu, M. V. Kubyshkina, T. I. Pulkkinen, H. U. Frey, A. Korth, M. Fraenz, E. Lucek, C. M. Carr, H. Reme, I. Dandouras, A. N. Fazakerley, G. D. Reeves, R. Friedel, K. H. Glassmeier, and C. P. Escoubet (2008), Multispacecraft and ground-based observations of substorm timing and activations: Two case studies, *Journal of Geophysical Research (Space Physics)*, *113*(A12), A07S25, doi:10.1029/2007JA012761.

Cao, X., Z. Y. Pu, A. M. Du, S. Tian, X. G. Wang, C. J. Xiao, H. U. Frey, M. V. Kubyshkina, V. M. Mishin, S. Y. Fu, L. Xie, and Q. G. Zong (2012), Auroral streamers implication for the substorm progression on September 14, 2004, *Planetary and Space Science*, *71*, 119–124, doi:10.1016/j.pss.2012.07.018.

Carr, C., P. Brown, T. L. Zhang, J. Gloag, T. Horbury, E. Lucek, W. Magnes, H. O'Brien, T. Oddy, U. Auster, P. Austin, O. Aydogar, A. Balogh, W. Baumjohann, T. Beek, H. Eichelberger, K.-H. Fornacon, E. Georgescu, K.-H. Glassmeier, M. Ludlam, R. Nakamura, and I. Richter (2005), The Double Star magnetic field investigation: instrument

design, performance and highlights of the first year's observations, *Annales Geophysicae*, *23*, 2713–2732, doi:10.5194/angeo-23-2713-2005.

Chang, R. P. H., and L. J. Lanzerotti (1975), On the generation of magnetohydrodynamic waves at the onset of a substorm, *Geophys. Res. Let.*, *2*, 489–491, doi:10.1029/GL002i011p00489.

Chen, C. X., and R. A. Wolf (1993), Interpretation of high-speed flows in the plasma sheet, *Journal of Geophysical Research*, *98*, 21,409, doi:10.1029/93JA02080.

Chen, C. X., and R. A. Wolf (1999), Theory of thin-filament motion in Earth's magnetotail and its application to bursty bulk flows, *Journal of Geophysical Research*, *104*, 14,613–14,626, doi:10.1029/1999JA900005.

Chiu, Y. T., and J. M. Cornwall (1980), Electrostatic model of a quiet auroral arc, *Journal of Geophysical Research*, *85*, 543–556, doi:10.1029/JA085iA02p00543.

Chiu, Y. T., A. L. Newman, and J. M. Cornwall (1981), On the structures and mapping of auroral electrostatic potentials, *Journal of Geophysical Research*, *86*, 10,029–10,037, doi:10.1029/JA086iA12p10029.

Chu, X., R. L. McPherron, T.-S. Hsu, and V. Angelopoulos (2015), Solar cycle dependence of substorm occurrence and duration: Implications for onset, *Journal of Geophysical Research (Space Physics)*, *120*, 2808–2818, doi:10.1002/2015JA021104.

Claudepierre, S. G., M. K. Hudson, W. Lotko, J. G. Lyon, and R. E. Denton (2010), Solar wind driving of magnetospheric ULF waves: Field line resonances driven by dynamic pressure fluctuations, *Journal of Geophysical Research (Space Physics)*, *115*(A14), A11202, doi:10.1029/2010JA015399.

Claudepierre, S. G., F. Toffoletto, J. Lyon, M. J. Wiltberger, and R. E. Denton (2013), Global magnetohydrodynamic simulations of resonant ultra-low frequency mode coupling in the inner magnetosphere and plasmasphere, *AGU Fall Meeting Abstracts*, p. C6.

Coroniti, F. V., and C. F. Kennel (1973), Can the ionosphere regulate magnetospheric convection?, *Journal of Geophysical Research*, *78*, 2837, doi:10.1029/JA078i016p02837.

Davis, T. N., and M. Sugiura (1966), Auroral electrojet activity index AE and its universal time variations, *Journal of Geophysical Research*, *71*, 785–801, doi:10.1029/JZ071i003p00785.

Dungey, J. W. (1961), Interplanetary Magnetic Field and the Auroral Zones, *Physical Review Letters*, *6*, 47–48, doi:10.1103/PhysRevLett.6.47.

Dungey, J. W. (1994), Memories, maxims, and motives, *J. Geophys. Res.*, *99*, 19,189, doi:10.1029/94JA00105.

El-Alaoui, M. (2001), Current disruption during November 24, 1996, substorm, *Journal of Geophysical Research*, *106*, 6229–6246, doi:10.1029/1999JA000260.

El-Alaoui, M., M. Ashour-Abdalla, R. J. Walker, V. Peroomian, R. L. Richard, V. Angelopoulos, and A. Runov (2009), Substorm evolution as revealed by THEMIS satellites and a global MHD simulation, *Journal of Geophysical Research (Space Physics)*, *114*(A13), A08221, doi:10.1029/2009JA014133.

El-Alaoui, M., M. Ashour-Abdalla, R. L. Richard, M. L. Goldstein, J. M. Weygand, and R. J. Walker (2010), Global magnetohydrodynamic simulation of reconnection and turbulence in the plasma sheet, *Journal of Geophysical Research (Space Physics)*, *115*(A14), A12236, doi:10.1029/2010JA015653.

El-Alaoui, M., R. L. Richard, M. Ashour-Abdalla, M. L. Goldstein, and R. J. Walker (2013), Dipolarization and turbulence in the plasma sheet during a substorm: THEMIS observations and global MHD simulations, *J. Geophys. Res. -Space*, *118*, 7752–7761, doi:10.1002/2013JA019322.

Evans, C. R., and J. F. Hawley (1988), Simulation of magnetohydrodynamic flows - A constrained transport method, *The Astrophysical Journal*, *332*, 659–677, doi:10.1086/166684.

Fedder, J. A., S. P. Slinker, J. G. Lyon, and R. D. Elphinstone (1995), Global numerical simulation of the growth phase and the expansion onset for a substorm observed by Viking, *Journal of Geophysical Research*, *100*, 19,083–19,094, doi:10.1029/95JA01524.

Frank, L. A., K. L. Ackerson, W. R. Paterson, J. A. Lee, M. R. English, and G. L. Pickett (1994), The Comprehensive Plasma Instrumentation (CPI) for the Geotail Spacecraft, *J. Geomag. and Geoelectr.*, *46*, 23–37.

Fridman, M., and J. Lemaire (1980), Relationship between auroral electrons fluxes and field aligned electric potential difference, *Journal of Geophysical Research*, *85*, 664–670, doi:10.1029/JA085iA02p00664.

Fujita, S., H. Nakata, M. Itonaga, A. Yoshikawa, and T. Mizuta (2002), A numerical simulation of the Pi2 pulsations associated with the substorm current wedge, *Journal of Geophysical Research (Space Physics)*, *107*, 1034, doi:10.1029/2001JA900137.

Gabrielse, C., V. Angelopoulos, A. Runov, H. U. Frey, J. McFadden, D. E. Larson, K.-H. Glassmeier, S. Mende, C. T. Russell, S. Apatenkov, K. R. Murphy, and I. J. Rae (2009), Timing and localization of near-Earth tail and ionospheric signatures during a substorm onset, *Journal of Geophysical Research (Space Physics)*, *114*(A13), A00C13, doi:10.1029/2008JA013583.

Ge, Y. S., J. Raeder, V. Angelopoulos, M. L. Gilson, and A. Runov (2011), Interaction of dipolarization fronts within multiple bursty bulk flows in global MHD simulations of a substorm on 27 February 2009, *Journal of Geophysical Research (Space Physics)*, *116*(A15), A00I23, doi:10.1029/2010JA015758.

Gjerloev, J. W. (2009), A Global Ground-Based Magnetometer Initiative, *EOS Transactions*, *90*, 230–231, doi:10.1029/2009EO270002.

Gjerloev, J. W. (2012), The SuperMAG data processing technique, *Journal of Geophysical Research (Space Physics)*, *117*(A16), A09213, doi:10.1029/2012JA017683.

Harel, M., R. A. Wolf, P. H. Reiff, R. W. Spiro, W. J. Burke, F. J. Rich, and M. Smiddy (1981), Quantitative simulation of a magnetospheric substorm. I - Model logic and overview, *Journal of Geophysical Research*, *86*, 2217–2241, doi:10.1029/JA086iA04p02217.

Hesse, M., and J. Birn (1991), On dipolarization and its relation to the substorm current wedge, *Journal of Geophysical Research*, *961*, 19,417–+, doi:10.1029/91JA01953.

Hones, E. W., Jr., T. Pytte, and H. I. West, Jr. (1984), Associations of geomagnetic activity with plasma sheet thinning and expansion - A statistical study, *Journal of Geophysical Research*, *89*, 5471–5478, doi:10.1029/JA089iA07p05471.

Hsu, T.-S., and R. L. McPherron (2007), A statistical study of the relation of Pi 2 and plasma flows in the tail, *Journal of Geophysical Research (Space Physics)*, *112*(A11), A05209, doi:10.1029/2006JA011782.

Hsu, T.-S., R. L. McPherron, V. Angelopoulos, Y. Ge, H. Zhang, C. Russell, X. Chu, and J. Kissinger (2012), A statistical analysis of the association between fast plasma flows and Pi2 pulsations, *Journal of Geophysical Research (Space Physics)*, *117*(A16), A11221, doi:10.1029/2012JA018173.

Hughes, W. J. (1974), The effect of the atmosphere and ionosphere on long period magnetospheric micropulsations, *Planet. Space Sci.*, *22*, 1157–1172, doi:10.1016/0032-0633(74)90001-4.

Jacobs, J. A., Y. Kato, S. Matsushita, and V. A. Troitskaya (1964), Classification of Geomagnetic Micropulsations, *Journal of Geophysical Research*, *69*, 180–181, doi:10.1029/JZ069i001p00180.

Keiling, A. (2012), Pi2 pulsations driven by ballooning instability, *Journal of Geophysical Research (Space Physics)*, *117*, A03228, doi:10.1029/2011JA017223.

Keiling, A., and K. Takahashi (2011), Review of Pi2 Models, *Space Sci. Rev.*, *161*, 63–148, doi:10.1007/s11214-011-9818-4.

Keiling, A., M. Fujimoto, H. Hasegawa, F. Honary, V. Sergeev, V. S. Semenov, H. U. Frey, O. Amm, H. Rème, I. Dandouras, and E. Lucek (2006), Association of Pi2 pulsations and pulsed reconnection: ground and Cluster observations in the tail lobe at 16 R_E, *Annales Geophysicae*, *24*, 3433–3449, doi:10.5194/angeo-24-3433-2006.

Keiling, A., V. Angelopoulos, D. Larson, R. Lin, J. McFadden, C. Carlson, J. W. Bonnell, F. S. Mozer, K.-H. Glassmeier, H. U. Auster, W. Magnes, S. Mende, H. Frey, A. Roux, O. LeContel, S. Frey, T. Phan, E. Donovan, C. T. Russell, I. Mann, W. Liu, X. Li, M. Fillingim, G. Parks, K. Shiokawa, and J. Raeder (2008), Correlation of substorm injections, auroral modulations, and ground Pi2, *Geophys. Res Let.*, *35*, L17S22, doi: 10.1029/2008GL033969.

Keiling, A., V. Angelopoulos, A. Runov, J. Weygand, S. V. Apatenkov, S. Mende, J. McFadden, D. Larson, O. Amm, K.-H. Glassmeier, and H. U. Auster (2009), Substorm current wedge driven by plasma flow vortices: THEMIS observations, *Journal of Geophysical Research (Space Physics)*, *114*, A00C22, doi:10.1029/2009JA014114.

Kennel, C. F., and H. E. Petschek (1966), Limit on Stably Trapped Particle Fluxes, *Journal of Geophysical Research*, *71*, 1.

Kepko, L., and M. Kivelson (1999), Generation of Pi2 pulsations by bursty bulk flows, *Journal of Geophysical Research*, *1042*, 25,021–25,034, doi:10.1029/1999JA900361.

Kepko, L., M. G. Kivelson, and K. Yumoto (2001), Flow bursts, braking, and Pi2 pulsations, *Journal of Geophysical Research*, *106*, 1903–1916, doi:10.1029/2000JA000158.

Kepko, L., M. G. Kivelson, R. L. McPherron, and H. E. Spence (2004), Relative timing of substorm onset phenomena, *Journal of Geophysical Research (Space Physics)*, *109*(A18), A04203, doi:10.1029/2003JA010285.

Kim, K.-H., K. Takahashi, S. Ohtani, and S.-K. Sung (2007), Statistical analysis of the relationship between earthward flow bursts in the magnetotail and low-latitude Pi2 pulsations, *Journal of Geophysical Research (Space Physics)*, *112*(A11), A10211, doi: 10.1029/2007JA012521.

Kissinger, J., R. L. McPherron, T.-S. Hsu, and V. Angelopoulos (2012), Diversion of plasma due to high pressure in the inner magnetosphere during steady magnetospheric convection, *Journal of Geophysical Research (Space Physics)*, *117*(A16), A05206, doi: 10.1029/2012JA017579.

Kivelson, M. G., and C. T. Russell (1995), *Introduction to Space Physics*, Cambridge University Press.

Knight, S. (1973), Parallel electric fields, *Planetary and Space Science*, *21*(5), 741 – 750, doi:http://dx.doi.org/10.1016/0032-0633(73)90093-7.

Kokubun, S., T. Yamamoto, M. H. Acuna, K. Hayashi, K. Shiokawa, and H. Kawano (1994), The Geotail Magnetic Field Experiment, *J. Geomag. Geoelectr.*, *46*, 7–21.

Kwon, H.-J., K.-H. Kim, D.-H. Lee, K. Takahashi, V. Angelopoulos, E. Lee, H. Jin, Y.-D. Park, J. Lee, P. R. Sutcliffe, and H. U. Auster (2012), Local time-dependent Pi2 frequencies confirmed by simultaneous observations from THEMIS probes in the inner magnetosphere and at low-latitude ground stations, *Journal of Geophysical Research (Space Physics)*, *117*, A01206, doi:10.1029/2011JA016815.

Lee, D.-H., and R. L. Lysak (1999), MHD waves in a three-dimensional dipolar magnetic field: A search for Pi2 pulsations, *Journal of Geophysical Research*, *104*, 28,691–28,700, doi:10.1029/1999JA900377.

Lester, M., W. J. Hughes, and H. J. Singer (1983), Polarization patterns of Pi 2 magnetic pulsations and the substorm current wedge, *Journal of Geophysical Research*, *88*, 7958–7966, doi:10.1029/JA088iA10p07958.

Liou, K. (2010), Polar ultraviolet imager observation of auroral breakup, *Journal of Geophysical Research: Space Physics*, *115*(A12), n/a–n/a, doi:10.1029/2010JA015578, a12219.

Lyon, J. G. (2007), Numerical Methods used in the Lyon-Fedder-Mobarry Global Code to model the magnetosphere, in *Advanced Methods for Space Simulations*, edited by Usui, H. and Omura, Y., pp. 101–109, Terrapub, Tokyo.

Lyon, J. G., J. A. Fedder, and C. M. Mobarry (2004), The Lyon-Fedder-Mobarry (LFM) global MHD magnetospheric simulation code, *Journal of Atmospheric and Solar-Terrestrial Physics*, *66*, 1333–1350, doi:10.1016/j.jastp.2004.03.020.

Lyons, L. R., D. S. Evans, and R. Lundin (1979), An observed relation between magnetic field aligned electric fields and downward electron energy fluxes in the vicinity of auroral forms, *Journal of Geophysical Research*, *84*, 457–461, doi:10.1029/JA084iA02p00457.

McPherron, R. L. (1970), Growth phase of magnetospheric substorms, *Journal of Geophysical Research*, *75*, 5592, doi:10.1029/JA075i028p05592.

McPherron, R. L. (1972), Substorm related changes in the geomagnetic tail: The growth phase, *Planetary and Space Science*, *20*, 1521, doi:10.1016/0032-0633(72)90054-2.

McPherron, R. L., C. T. Russell, and M. P. Aubry (1973), Satellite studies of magnetospheric substorms on August 15, 1968: 9. Phenomenological model for substorms, *Journal of Geophysical Research*, *78*, 3131, doi:10.1029/JA078i016p03131.

Mende, S. B., H. U. Frey, M. Lampton, J.-C. Gerard, B. Hubert, S. Fuselier, J. Spann, R. Gladstone, and J. L. Burch (2001), Global observations of proton and electron auroras in a substorm, *Geophys. Res. Let.*, *28*, 1139–1142, doi:10.1029/2000GL012340.

Merkin, V. G., and J. G. Lyon (2010), Effects of the low-latitude ionospheric boundary condition on the global magnetosphere, *Journal of Geophysical Research*, *115*(A14), A10202, doi:10.1029/2010JA015461.

Miyashita, Y., S. Machida, T. Mukai, Y. Saito, K. Tsuruda, H. Hayakawa, and P. R. Sutcliffe (2000), A statistical study of variations in the near and middistant magnetotail associated with substorm onsets: GEOTAIL observations, *Journal of Geophysical Research*, *105*, 15,913–15,930, doi:10.1029/1999JA000392.

Miyashita, Y., S. Machida, Y. Kamide, D. Nagata, K. Liou, M. Fujimoto, A. Ieda, M. H. Saito, C. T. Russell, S. P. Christon, M. Nosé, H. U. Frey, I. Shinohara, T. Mukai, Y. Saito, and H. Hayakawa (2009), A state-of-the-art picture of substorm-associated evolution of the

near-Earth magnetotail obtained from superposed epoch analysis, *Journal of Geophysical Research (Space Physics)*, *114*(A13), A01,211, doi:10.1029/2008JA013225.

Moen, J., and A. Brekke (1993), The solar flux influence on quiet time conductances in the auroral ionosphere, *Geophys. Res. Let.*, *20*, 971–974, doi:10.1029/92GL02109.

Murphy, K. R., I. J. Rae, I. R. Mann, and D. K. Milling (2011a), On the nature of ULF wave power during nightside auroral activations and substorms: 1. Spatial distribution, *Journal of Geophysical Research (Space Physics)*, *116*, A00I21, doi:10.1029/2010JA015757.

Murphy, K. R., I. J. Rae, I. R. Mann, A. P. Walsh, D. K. Milling, and A. Kale (2011b), The dependence of Pi2 waveforms on periodic velocity enhancements within bursty bulk flows, *Annales Geophysicae*, *29*, 493–509, doi:10.5194/angeo-29-493-2011.

Nagai, T., M. Fujimoto, R. Nakamura, Y. Saito, T. Mukai, T. Yamamoto, A. Nishida, S. Kokubun, G. D. Reeves, and R. P. Lepping (1998), Geotail observations of a fast tailward flow at $X_{GSM} = -15R_E$, *Journal of Geophysical Research*, *103*, 23,543–23,550, doi:10.1029/98JA02246.

Nakamizo, A., and T. Iijima (2003), A new perspective on magnetotail disturbances in terms of inherent diamagnetic processes, *Journal of Geophysical Research (Space Physics)*, *108*, 1286, doi:10.1029/2002JA009400.

Nakamura, R., W. Baumjohann, T. L. Zhang, C. M. Carr, A. Balogh, K.-H. Fornacon, E. Georgescu, H. Rème, I. Dandouras, T. Takada, M. Volwerk, Y. Asano, A. Runov, H. Eichelberger, B. Klecker, C. Mouikis, L. M. Kistler, and O. Amm (2005), Cluster and Double Star observations of dipolarization, *Annales Geophysicae*, *23*, 2915–2920, doi:10.5194/angeo-23-2915-2005.

Nakamura, R., A. Retinò, W. Baumjohann, M. Volwerk, N. Erkaev, B. Klecker, E. A. Lucek, I. Dandouras, M. André, and Y. Khotyaintsev (2009), Evolution of dipolarization in the near-Earth current sheet induced by Earthward rapid flux transport, *Annales Geophysicae*, *27*, 1743–1754, doi:10.5194/angeo-27-1743-2009.

Newell, P. T., and J. W. Gjerloev (2011), Evaluation of SuperMAG auroral electrojet indices as indicators of substorms and auroral power, *Journal of Geophysical Research (Space Physics)*, *116*(A15), A12211, doi:10.1029/2011JA016779.

Øieroset, M., T. D. Phan, M. Fujimoto, R. P. Lin, and R. P. Lepping (2001), In situ detection of collisionless reconnection in the Earth's magnetotail, *Nature*, *412*, 414–417, doi:10.1038/35086520.

Olson, J. V. (1999), Pi2 pulsations and substorm onsets: A review, *Journal of Geophysical Research*, *104*, 17,499–17,520, doi:10.1029/1999JA900086.

Owens, J. H., and J. Fedder (1978), The effects of geomagnetic field aligned potential differences on precipitating magnetospheric particles, *Tech. rep.*, NRL.

Palmroth, M., P. Janhunen, G. Germany, D. Lummerzheim, K. Liou, D. N. Baker, C. Barth, A. T. Weatherwax, and J. Watermann (2006), Precipitation and total power consumption in the ionosphere: Global MHD simulation results compared with Polar and SNOE observations, *Annales Geophysicae*, *24*, 861–872, doi:10.5194/angeo-24-861-2006.

Panov, E. V., R. Nakamura, W. Baumjohann, V. Angelopoulos, A. A. Petrukovich, A. Retinò, M. Volwerk, T. Takada, K.-H. Glassmeier, J. P. McFadden, and D. Larson (2010), Multiple overshoot and rebound of a bursty bulk flow, *Geophys. Res. Let.*, *370*, L08,103, doi:10.1029/2009GL041971.

Parker, E. N. (1957), Sweet's Mechanism for Merging Magnetic Fields in Conducting Fluids, *Journal of Geophysical Research*, *62*, 509–520, doi:10.1029/JZ062i004p00509.

Pembroke, A., F. Toffoletto, S. Sazykin, M. Wiltberger, J. Lyon, V. Merkin, and P. Schmitt (2012), Initial results from a dynamic coupled magnetosphere-ionosphere-ring current model, *Journal of Geophysical Research (Space Physics)*, *117*, A02211, doi:10.1029/2011JA016979.

Pontius, D. H., Jr., and R. A. Wolf (1990), Transient flux tubes in the terrestrial magnetosphere, *Geophys. Res. Let.*, *17*, 49–52, doi:10.1029/GL017i001p00049.

Pytte, T., R. L. McPherron, M. G. Kivelson, H. I. West, Jr., and E. W. Hones, Jr. (1976), Multiple-satellite studies of magnetospheric substorms - Radial dynamics of the plasma sheet, *Journal of Geophysical Research*, *81*, 5921–5933, doi:10.1029/JA081i034p05921.

Rae, I. J., I. R. Mann, K. R. Murphy, D. K. Milling, A. Parent, V. Angelopoulos, H. U. Frey, A. Kale, C. E. J. Watt, S. B. Mende, and C. T. Russell (2009), Timing and localization of ionospheric signatures associated with substorm expansion phase onset, *Journal of Geophysical Research (Space Physics)*, *114*, A00C09, doi:10.1029/2008JA013559.

Raeder, J., J. Berchem, and M. Ashour-Abdalla (1996), The importance of small scale processes in global MHD simulations: Some numerical experiments, in *The Physics of Space Plasmas*, vol. 14, edited by J. R. J. T. Chang, p. 403.

Raeder, J., J. Berchem, and M. Ashour-Abdalla (1998), The Geospace Environment Modeling Grand Challenge: Results from a Global Geospace Circulation Model, *Journal of Geophysical Research*, *1031*, 14,787–14,798, doi:10.1029/98JA00014.

Raeder, J., R. L. McPherron, L. A. Frank, S. Kokubun, G. Lu, T. Mukai, W. R. Paterson, J. B. Sigwarth, H. J. Singer, and J. A. Slavin (2001), Global simulation of the Geospace Environment Modeling substorm challenge event, *Journal of Geophysical Research*, *106*, 381–396, doi:10.1029/2000JA000605.

Ream, J. B., R. J. Walker, M. Ashour-Abdalla, M. El-Alaoui, M. G. Kivelson, and M. L. Goldstein (2013), Generation of Pi2 pulsations by intermittent earthward propagating dipolarization fronts: An MHD case study, *Journal of Geophysical Research*, *118*, 6364–6377, doi:10.1002/2013JA018734.

Ream, J. B., R. J. Walker, M. Ashour-Abdalla, M. El-Alaoui, M. Wiltberger, M. G. Kivelson, and M. L. Goldstein (2015), Propagation of Pi2 Pulsations Through the Braking Region in Global MHD Simulations (Submitted), *Journal of Geophysical Research*, doi:10.1002/2015JA021572.

Richmond, A. D., and Y. Kamide (1988), Mapping electrodynamic features of the high-latitude ionosphere from localized observations - Technique, *Journal of Geophysical Research*, *93*, 5741–5759, doi:10.1029/JA093iA06p05741.

Robinson, R. M., R. R. Vondrak, K. Miller, T. Dabbs, and D. Hardy (1987), On calculating ionospheric conductances from the flux and energy of precipitating electrons, *Journal of Geophysical Research*, *92*, 2565–2569, doi:10.1029/JA092iA03p02565.

Runov, A., V. Angelopoulos, M. I. Sitnov, V. A. Sergeev, J. Bonnell, J. P. McFadden, D. Larson, K.-H. Glassmeier, and U. Auster (2009), THEMIS observations of an earthward-propagating dipolarization front, *Geophys. Res. Let.*, *36*, L14106, doi:10.1029/2009GL038980.

Runov, A., V. Angelopoulos, M. Sitnov, V. A. Sergeev, R. Nakamura, Y. Nishimura, H. U. Frey, J. P. McFadden, D. Larson, J. Bonnell, K.-H. Glassmeier, U. Auster, M. Connors, C. T. Russell, and H. J. Singer (2011), Dipolarization fronts in the magnetotail plasma sheet, *Planet. Space Sci.*, *59*, 517–525, doi:10.1016/j.pss.2010.06.006.

Russell, C. T., and R. L. McPherron (1973), The Magnetotail and Substorms, *Space Science Reviews*, *15*, 205–266, doi:10.1007/BF00169321.

Saito, T., and S. Matsushita (1968), Solar cycle effects on geomagnetic Pi 2 pulsations, *Journal of Geophysical Research*, *73*, 267, doi:10.1029/JA073i001p00267.

Saito, T., K. Yumoto, and Y. Koyama (1976), Magnetic pulsation Pi2 as a sensitive indicator of magnetospheric substorm, *Planet. Space Sci.*, *24*, 1025–1029, doi:10.1016/0032-0633(76)90120-3.

Sakurai, T., and R. L. McPherron (1983), Satellite observations of Pi 2 activity at synchronous orbit, *Journal of Geophysical Research*, *88*, 7015–7027, doi:10.1029/JA088iA09p07015.

Sakurai, T., and T. Saito (1976), Magnetic pulsations Pi2 and substorm onset, *Planet. Space Sci.*, *24*, 573–575, doi:10.1016/0032-0633(76)90135-5.

Samson, J. C. (1982), Pi 2 pulsations - High latitude results, *Planet. Space Sci.*, *30*, 1239–1247, doi:10.1016/0032-0633(82)90097-6.

Schield, M. A. (1969), Pressure balance between solar wind and magnetosphere, *Journal of Geophysical Research*, *74*, 1275, doi:10.1029/JA074i005p01275.

Scholer, M., B. Klecker, D. Hovestadt, G. Gloeckler, F. M. Ipavich, and E. J. Smith (1984), Fast moving plasma structures in the distant magnetotail, *Journal of Geophysical Research*, *89*, 6717–6727, doi:10.1029/JA089iA08p06717.

Sergeev, V. A., V. Angelopoulos, J. T. Gosling, C. A. Cattell, and C. T. Russell (1996), Detection of localized, plasma-depleted flux tubes or bubbles in the midtail plasma sheet, *Journal of Geophysical Research*, *101*, 10,817–10,826, doi:10.1029/96JA00460.

Shiokawa, K., W. Baumjohann, and G. Haerendel (1997), Braking of high-speed flows in the near-Earth tail, *Geophys. Res. Let.*, *24*, 1179–1182, doi:10.1029/97GL01062.

Singer, H. J., W. J. Hughes, P. F. Fougere, and D. J. Knecht (1983), The localization of Pi 2 pulsations - Ground-satellite observations, *Journal of Geophysical Research*, *88*, 7029–7036, doi:10.1029/JA088iA09p07029.

Sitnov, M. I., M. Swisdak, and A. V. Divin (2009), Dipolarization fronts as a signature of transient reconnection in the magnetotail, *Journal of Geophysical Research (Space Physics)*, *114*(A13), A04,202, doi:10.1029/2008JA013980.

Slavin, J. A., D. H. Fairfield, R. P. Lepping, A. Szabo, M. J. Reiner, M. Kaiser, C. J. Owen, T. Phan, R. Lin, S. Kokubun, T. Mukai, T. Yamamoto, H. J. Singer, S. A. Romanov, J. Buechner, T. Iyemori, and G. Rostoker (1997), WIND, GEOTAIL, and GOES 9 observations of magnetic field dipolarization and bursty bulk flows in the near-tail, *Geophysical Research Letters*, *24*, 971–974, doi:10.1029/97GL00542.

Slinker, S. P., J. A. Fedder, B. A. Emery, K. B. Baker, D. Lummerzheim, J. G. Lyon, and F. J. Rich (1999), Comparison of global MHD simulations with AMIE simulations

for the events of May 19-20, 1996, *Journal of Geophysical Research*, *104*, 28,379–28,396, doi:10.1029/1999JA900403.

Solovyev, S. I., D. G. Baishev, E. S. Barkova, N. E. Molochushkin, and K. Yumoto (2000), Pi2 magnetic pulsations as response on spatio-temporal oscillations of auroral arc current system, *Geophysical Research Letters*, *27*, 1839–1842, doi:10.1029/2000GL000037.

Southwood, D. J., and W. F. Stuart (1980), Pulsations at the substorm onset, in *Dynamics of the Magnetosphere*, edited by S.-I. Akasofu, pp. 341–355.

Stuart, W. F., P. M. Brett, and T. J. Harris (1979), Mid-latitude secondary resonance in Pi2's, *Journal of Atmospheric and Terrestrial Physics*, *41*, 65–75.

Sutcliffe, P. R. (1975), The association of harmonics in Pi2 power spectra with the plasmapause, *Planetary and Space Science*, *23*, 1581–1587, doi:10.1016/0032-0633(75)90085-9.

Sutcliffe, P. R., and K. Yumoto (1991), On the cavity mode nature of low-latitude Pi 2 pulsations, *Journal of Geophysical Research*, *96*, 1543–1551, doi:10.1029/90JA02007.

Takahashi, K., S.-I. Ohtani, and K. Yumoto (1992), AMPTE CCE observations of Pi 2 pulsations in the inner magnetosphere, *Geophys. Res. Let.*, *19*, 1447–1450, doi:10.1029/92GL01283.

Toffoletto, F., S. Sazykin, R. Spiro, and R. Wolf (2003), Inner magnetospheric modeling with the Rice Convection Model, *Space Sci. Rev.*, *107*, 175–196, doi:10.1023/A:1025532008047.

Uozumi, T., H. Kawano, A. Yoshikawa, M. Itonaga, and K. Yumoto (2007), Pi 2 source region in the magnetosphere deduced from CPMN data, *Planet. Space Sci.*, *55*, 849–857, doi:10.1016/j.pss.2006.03.016.

Uozumi, T., S. Abe, K. Kitamura, T. Tokunaga, A. Yoshikawa, H. Kawano, R. Marshall, R. J. Morris, B. M. Shevtsov, S. I. Solovyev, D. J. McNamara, K. Liou, S. Ohtani, M. Itonaga, and K. Yumoto (2009), Propagation characteristics of Pi 2 pulsations observed at high- and low-latitude MAGDAS/CPMN stations: A statistical study, *Journal of Geophysical Research (Space Physics)*, *114*(A13), A11207, doi:10.1029/2009JA014163.

Uozumi, T., K. Yumoto, T. Tokunaga, S. I. Solovyev, B. M. Shevtsov, R. Marshall, K. Liou, S. Ohtani, S. Abe, A. Ikeda, K. Kitamura, A. Yoshikawa, H. Kawano, and M. Itonaga (2011), AKR modulation and global Pi2 oscillation, *Journal of Geophysical Research (Space Physics)*, *116*, A06214, doi:10.1029/2010JA016042.

Walker, R. J., M. Ashour-Abdalla, M. El Alaoui, and F. V. Coroniti (2006), Magnetospheric convection during prolonged intervals with southward interplanetary magnetic field, *Journal of Geophysical Research (Space Physics)*, *111*(A10), A10219, doi:10.1029/2005JA011541.

Webster, D. J., J. C. Samson, and G. Rostoker (1989), Eastward propagation of transient field-aligned currents and Pi 2 pulsations at auroral latitudes, *Journal of Geophysical Research*, *94*, 3619–3630, doi:10.1029/JA094iA04p03619.

Wiltberger, M., R. S. Weigel, W. Lotko, and J. A. Fedder (2009), Modeling seasonal variations of auroral particle precipitation in a global-scale magnetosphere-ionosphere simulation, *Journal of Geophysical Research (Space Physics)*, *114*, A01204, doi:10.1029/2008JA013108.

Wolf, R. A., Y. Wan, X. Xing, J.-C. Zhang, and S. Sazykin (2009), Entropy and plasma sheet transport, *Journal of Geophysical Research (Space Physics)*, *114*(A13), A00D05, doi:10.1029/2009JA014044.

Yeoman, T. K., and D. Orr (1989), Phase and spectral power of mid-latitude Pi2 pulsations - Evidence for a plasmaspheric cavity resonance, *Planetary and Space Science*, *37*, 1367–1383, doi:10.1016/0032-0633(89)90107-4.

Yeoman, T. K., M. P. Freeman, G. D. Reeves, M. Lester, and D. Orr (1994), A comparison of midlatitude Pi 2 pulsations and geostationary orbit particle injections as substorm indicators, *Journal of Geophysical Research*, *99*, 4085–4093, doi:10.1029/93JA03233.

Yumoto, K., T. Saito, K. Takahashi, F. W. Menk, and B. J. Fraser (1989), Some aspects of the relation between Pi 1-2 magnetic pulsations observed at L = 1.3-2.1 on

the ground and substorm-associated magnetic field variations in the near-earth magnetotail observed by AMPTE CCE, *Journal of Geophysical Research*, *94*, 3611–3618, doi: 10.1029/JA094iA04p03611.